INFORMATION TO USERS

While the most advanced technology has been used to photograph and reproduce this manuscript, the quality of the reproduction is heavily dependent upon the quality of the material submitted. For example:

- Manuscript pages may have indistinct print. In such cases, the best available copy has been filmed.

- Manuscripts may not always be complete. In such cases, a note will indicate that it is not possible to obtain missing pages.

- Copyrighted material may have been removed from the manuscript. In such cases, a note will indicate the deletion.

Oversize materials (e.g., maps, drawings, and charts) are photographed by sectioning the original, beginning at the upper left-hand corner and continuing from left to right in equal sections with small overlaps. Each oversize page is also filmed as one exposure and is available, for an additional charge, as a standard 35mm slide or as a 17"x 23" black and white photographic print.

Most photographs reproduce acceptably on positive microfilm or microfiche but lack the clarity on xerographic copies made from the microfilm. For an additional charge, 35mm slides of 6"x 9" black and white photographic prints are available for any photographs or illustrations that cannot be reproduced satisfactorily by xerography.

Order Number 8713797

Modulation and Raman spectroscopy study of microstructural geometries in semiconductors

Shen, Hongen, Ph.D.

City University of New York, 1987

U·M·I
300 N. Zeeb Rd.
Ann Arbor, MI 48106

PLEASE NOTE:

In all cases this material has been filmed in the best possible way from the available copy. Problems encountered with this document have been identified here with a check mark ✓.

1. Glossy photographs or pages ____
2. Colored illustrations, paper or print ____
3. Photographs with dark background ____
4. Illustrations are poor copy ____
5. Pages with black marks, not original copy ____
6. Print shows through as there is text on both sides of page ____
7. Indistinct, broken or small print on several pages ✓
8. Print exceeds margin requirements ____
9. Tightly bound copy with print lost in spine ____
10. Computer printout pages with indistinct print ____
11. Page(s) ____ lacking when material received, and not available from school or author.
12. Page(s) ____ seem to be missing in numbering only as text follows.
13. Two pages numbered ____. Text follows.
14. Curling and wrinkled pages ____
15. Dissertation contains pages with print at a slant, filmed as received ✓
16. Other ____

University
Microfilms
International

Modulation and Raman Spectroscopy Study

of Microstructural Geometries in Semiconductors

by

Hongen Shen

A dissertation submitted to the Graduate Faculty in Physics in partial fulfillment of the requirements for the degree of Doctor of Philosophy, The City University of New York

1987

This manuscript has been read and accepted for the Graduate Faculty in Physics in satisfaction of the dissertation requirement for the degree of Doctor of Philosophy.

10/29/86
date

Chairman of Examining Committee

11/6/86
date

Executive Office

F. H. Pollak
J. B. Krieger
G. Skoriko
A. Genack
R. N. Sacks

Supervisory Committee

The City University of New York

ABSTRACT

Modulation and Raman Spectroscopy Study of Microstructural Geometries

by

Hongen Shen

Advisor: Professor Fred H. Pollak

Microstructural geometries i. e., they are structures on the order of several lattice constants (10A) to several hundred lattice constants (1000A), such as $Ga_{1-x}Al_xAs$/GaAs superlattices, GaAs doping superlattices, GaAs and InP space charge region and process induced surface strain layers, were investigated using photoreflectance (PR), electroreflectance (ER) and Raman scattering.

We have demonstrated for the first time that photoreflectance spectra from superlattices can be fit by a third derivative function electromodulation lineshape, thus making it possible to precisely determine energies of the quantum transitions. By employing a detailed lineshape fit, we can detect a barrier height change of several millielectron volts and variations in well width as small as 2A with a spatial resolution

about 100μm. For the first time at room temperature, several forbidden transitions from GaAlAs/GaAs superlattices have been clearly observed, which is a strong support to the valence band mixing theory in superlattices.

The Franz-Keldysh theory for modulation spectroscopy has been generalized to involving both dc and ac fields. We have demonstrated, both theoretically and experimentally that provided that ac field is smaller than dc field, Franz-Keldysh oscillations in modulation spectroscopy are related to the dc electric field and not to the ac modulation field. The effect of ac field is to produces a non-uniform modulation which smears ut high order oscillations.

Photoreflectance study on doping superlattices (nipi) have been performed. For samples with small periodicity, the room temperature spectra showed quantum size effect. For samples with large periodicity, spectra exhibited Franz-Keldysh oscillations. The pump chopping frequency dependence of the PR signal was employed to measure the recombination lifetime of the carriers.

The effect of polish-induced stress on the LO Raman spectra from GaAs and InP have been investigated in detail. The lineshape changes have been quantitatively accounted for by a model based on the convolution of the skin depth of light and the penetration depth of the

polish-induced surface strain. The strain penetration depth as well as the surface strain were determined for various polishing conditions.

We demonstrated that Raman scattering can be used to determine the width of the depletion layer as well as carrier concentration for <100> n-type GaAs (up to $n=10^{19}cm^{-3}$). The results are correlated with a generalized theory of the depletion width for both degenerate and non-degenerate situation at finite temperatures. We have also obtained the coefficient of electric field induced Raman tensor (both amplitude and phase) as well as impurity induced Raman tensor for <100> GaAs at 2.7eV (4579A).

ACKNOWLEDGEMENTS

I wish to express my great appreciation to my adviser, professor Fred H. Pollak. Without his guidance, support, and encouragement, this work would never have been seen the light of day. His enthusiasm and creativity in exploring and understanding physics were an inspiration. His valuable friendship and his constant interest in my progress has given me more than one could hope for in a mentor.

To the other members of the committee, Professor J. B. Krieger and Professor G. Skorinko of Brooklyn College, Professor A. Genack of Queens College and Dr. R. N. Sacks my sincerest thanks for agreeing to serve on my committee and for your careful reading of this manuscript and helpful advice. I particularly want to thank Dr. Sacks for maintaining a constant supply of various samples used in this study. Special thanks also to Professor Krieger for his constant encouragement and his wonderful lectures.

I am deeply indebted to Dr. J. N. Schulman of Hughes Research Laboratory for his valuable helps in calculations of the quantized energy levels and matrix elements for various superlattices and quantum wells. Thanks are also due to Dr. O. J. Glembocki at Naval Research Laboratory for the useful discussion in the possible mechanisms of pho-

toreflectance from superlattices. I have been most fortunate to have had the opportunity to work closely with two special colleagues Dr. X. C. Shen and Dr. Padman Parayanthal. Thanks for their encouragement and helpful suggestions. I also appreciate the help of the other colleagues in ths Solid State Laboratory; Dr. R. N. Bhattacharya and Mr. A. Ksendzov stand out in this regard.

I would like to express my gratitude to Dr. T. J. Drummond of Sandia National Laboratories, Dr. Arthur J. Smirl of Hughes Research Laboratory, Dr Coutts of SERI and Dr. G. Iseler of Lincoln Laboratory MIT for providing the samples used in this study.

I wish to acknowledge ith gratitude the department of Physics of Brooklyn College for providing me this opportunity, the Research Foundation of CUNY for the financial support during the course of this work.

Words can not express my appreciation to and admiration for my wife, Yixin for her support and sacrifice during the years of my graduate career. This work is as much of a reflection of that as of my efforts.

PUBLICATIONS

1. "Raman Study of Polish-induced Surface Strain in <100> GaAs and InP", H. Shen and Fred H. Pollak, Appl. Phys. Lett. 45 692 (1984).

2. "Raman Scattering Determination of Free-Carrier Concentration and Surface Space-Charge Layer in <100> n-GaAS", H. Shen, Fred H. Pollak and R. N. Sacks, Appl. Phys. Lett. 47 891 (1985).

3. "Highly Doped GaAs:Si by Molecular Beam Epitaxy", R. N. Sack and H. Shen, Appl. Phys. Lett. 47 374 (1985).

4. "Photoreflectance Study of GaAS/AlAs Superlattices: Fit to Electromodulation Theory", H. Shen, P. Parayanthal, Fred H. Pollak, Micha Tomkiewicz, T. J. Drummond and J. N. Schulman, Appl. Phys. Lett. 48 653 (1986).

5. "Photoreflectance GaAS/GaAlAs Multiple Quantum: Topographical Variation in Barrier Height and Well Width", P. Parayanthal, H Shen, Fred H. Pollak, O. J. Glembocki, B. V. Shamabrook and W. T. Beard, Appl. Phys. Lett. 48 1261 (1986).

6. "Observation of Symmetry Forbidden Transition in the Room Temperature Photoreflectance Spectra of a GaAs/GaAlAs Quantum

Well", H. Shen, P. Parayanthal, Fred H. Pollak, Arthur L. Smirl, J. N. Schulman, R. A. McFarlane and Irnee D'Haenens, Solid State Comm. 59 557 (1986).

7. "Photoreflectance Characterization of Space Charge Region in Semiconductors: ITO/InP as a Model System", R. N. Bhattacharya. H. Shen, P.Parayanthal, Fred H. Pollak, T. Coutts and H. Aharoni, to be published in Solar Cells.

8. "Raman Study of Polish-induced Surface Strain in <100> and <111> GaAs and InP", H. Shen, Z. Hang and H. Pollak, Proceedings of the Society of Photo-Optical Instrumentation Engineers (SPIE,Bellingham, 1985) 524, 118 (1985)

9. "Raman Scattering Determination of Free-Carrier Concentration and Surface Space-Charge Layer in <100> n-GaAS", H. Shen, Fred H. Pollak and R. N. Sacks, Proceedings of the Society of Photo-Optical Instrumentation Engineers (SPIE. bellingham, 1985) 524, 145 (1985)

10. "Observation of Symmetry Forbidden Transition in the Photoreflectance Spectra of a GaAs/GaAlAs Quantum Well", H. Shen, P. Parayanthal, Fred H. Pollak, Arthur L. Smirl, J. N. Schulman, R. A. McFarlane and Irnee D'Haenens to be published in the Proceedings of the 18th International Conference on the Physics of Semiconductors, Stockholm, 1986.

11. "Photoreflectance of GaAs Doping Superlattices", H. Shen, X. C. Shen, Fred H. Pollak, J. N. Schulman, Arthur L. Smirl, R. M. McFarlane and Irnee D'Haenens, to be published in Proceedings of the Second International Conference on Superlattices, Microstructure and Microdevices, Gothenburg, Sweden, 1986

INTRODUCTION

In his closing address at the 15th Internationa' Conference on the Physics of Semiconductors in 1980 in Kyoto, Professor Y. Uemura remarked that " the birth and rapid growth of new fields during this decade have been so remarkable that trends in research seem to indicate a sign of transformations. Therefore I would like to propose the heading 'sign of transformations'"[1]. Some of the "sign of transformation" that were mentioned by Professor Uemura included bulk to surface and interface, periodic to random or disordered, natural to designed. One of the common factors of these important new areas of investigation are that they consist of microstructural geometries, i. e., they are structures on the order of several lattice constants (10A) to several hundred lattice constants (1000A). Optical techniques are powerful methods for studying such microstructural geometries. Two of the most useful are modulation spectroscopy [2] [3] [4] [5] [6] [7], which probes the electronic states of the system, and Raman Spectroscopy (RS) [8] [9] [10] [11], which is a function of the lattice vibrations of the material.

In this thesis we have investigated the electronic and vibrational properties of various microstructural geometries using modulation spec-

troscopy and Raman scattering. The selected microstructural geometries were compositional and doping quantum wells and superlattices, the space charge region of III-V semiconductors and process-induced surface damage in III-V semiconductors.

Although modulation spectroscopy, particularly electroreflectance has been used extensively to study semiconductors in bulk and thin film form only recently is this approach being applied to study microstructural geometries, i. e. superlattices, quantum wells and heterojuctions. In the past electromodulation has proven to be the most useful method since it yields the sharpest structure, related to the third derivative function (TDF) of the optical constants, also its lineshape is well defined (the Aspnes TDF lineshape) thus enabling investigators to accurately determine the energies, broadening parameters, phases and amplitudes of optical transitions even at room temperature. The sensitivity of electroreflectance to electric fields can be utilized to evaluate the surface and interfacial fields in systems which usually are very important for fundamental and applied studies. In addition, electromodulation signal is inversely proportional to the reduced interband effective mass, thus making it extremely suitable for investigation of the optical properties related to the fundamental gap. Photoreflectance is a special mode of electroreflectance, where the optical constants of the

material are modulated by the photo-injection of electron-hole pairs by a secondary (pump) light source. It is contactless and has certain advantage compared with other modulation techniques. For example, effects of perturbations such as temperature or strain or hydrostatic pressures can be conveniently studied.

Raman scattering is a versatile and effective tool for investigating the lattice vibrations of a semiconductor and interactions of the phonons with other excitations such as plasmons, etc. Since lattice vibrations are very sensitive to local environments, RS can yield information about the semiconductor or structure on the scale of a few lattice constants. Thus it is ideal for investigating the nature of microstructural geometries. Also since RS is a second-order process it contains important symmetry information which is not available from first order optical interactions. In RS, both polarization selection rules as well as peak positions are sensitive to perturbations, both internal and external, such as strain, electric fields, temperature, etc. Furthermore, by using various excitation lines of different wavelengths it is possible to perform depth-profiling measurements.

The $Ga_{1-x}Al_xAs/GaAs$ quantum wells and superlattices are probably among the most important of the various semiconductor systems fabricated in the past decade. The first electroreflectance measurements of

$Ga_{1-x}Al_xAs/GaAs$ multiple quantum wells (MQW) and superlattices (SL) was reported by E. E. Mendez et al [12]and M. Erman [13]. Photoreflectance measurements (PR) of $Ga_{1-x}Al_xAs/GaAs$ quantum wells were recently reported by Glembocki et al [14] [15]. The spectra of well characterized multiple quantum well (MQW) sample exhibit the complete ladder of interband transitions between the heavy hole and conduction subband states. Weaker structure was detected at the photon energies corresponding to excitations for light hole to conduction subband states. As $Ga_{1-x}Al_xAs/GaAs$ quantum wells and superlattices are of great interest from both fundamental as well as technological considerations, it is essentially important to experimentally determine (a) composition x of $Ga_{1-x}Al_xAs$ epilayer ,(b) width of the quantum well and (c) conduction band offset. The search for allowed and forbidden quantum transitions helps to examine our theoretical knowledge of the band mixture effect in quantum wells[16].

Doping superlattices (n-i-p-i) are another interesting class of superlattices. As the requirements for growing high quality n-i-p-i are less demanding and they have wide applications, it has been attracting considerable attention recently. Very little modulation studies have been studied on this system. To our knowledge there is only one photoreflectance measurement on InP nipi has been reported very

recently [17]. The mechanism of PR in nipi are quite different from compositional superlattices. A detail study for different potential profiles are important to explore this new area.

The Space Charge Region (SCR) of a semiconductor plays an important rule in semiconductor devices. The direct sensitivity of the features in the modulation spectroscopy, particularly ER and PR, to the nature of surface field has been noted by a number of investigators [6] [7] [18] [19] [20]. Most of the works were done in the low field region, where the built in dc field was small and so was the ac modulation field [6]. If the low field condition is not met, Franz-Keldysh oscillations (FKO) begin to appear, which can also yield information about the SCR. In previous studies [6], the built-in dc field was small and so was the ac field. The FKO were related to the modulation electric field. These prior investigation did not consider the effect of a dc electric field in SCR. In order to understand the performance of SCR devices, it is important to know how dc and ac fields play different rule in modulation spectroscopy.

Heavily doped III-V semiconductors are of interest from both a fundamental and technological point of view. For examples, the effect of electron-phonon coupling as well as high surface electric field can be studied in such system. Only recently with the improvement of MBE

Raman spectra lineshapes are accounted for by a model based on the convolution of the penetration depth of the light and the skin depth of the polish induced surface strain. Also discussed in this section is the result from heavily doped n-GaAs. Both carrier concentration and depletion width are examined and compared to a generalized theory for both degenerate and non-degenerate materials at finite temperatures. The coefficients of electric field induced Raman tensor (both amplitude and phase) and impurity induced raman tensor are also evaluated for <100> GaAs at 2.7eV (4579A).

In the last chapter we summarize the results and conclusions of our investigations.

in Section 1 and the experimental procedures in Section 2. In the experimental section we highlight a newly developed servo mechanism for normalizing the spectrum, which has a considerable advantages over the previous one. Section 3 contains the results obtained by modulation spectroscopy for $Ga_{1-x}Al_xAs/GaAs$ quantum wells, superlattices and GaAs doping superlattices (nipi). The main focus is on the accurate determination of the various transition energies using third derivative lineshape. Topographic variation and depth profiling of superlattices are carried out. Violation of the selection rules and observation of forbidden transitions are reported as a support to the band mixing theory. Also presented in this section are the generalized FKO theory and the experiment evidence on InP/ITO SCR.

Raman spectroscopy is discussed in Chapter III. The basic principles of Raman scattering are covered in Section 1 and experimental techniques in Section 2. In Section 3 we describe the results of the investigation regarding polish-induced surface strain. The resulting LO Raman spectra lineshapes are accounted for by a model based on the convolution of the penetration depth of the light and the skin depth of the polish induced surface strain. Also discussed in this section is the result from heavily doped n-GaAs. Both carrier concentration and depletion width are examined and compared to a generalized theory for

both degenerate and non-degenerate materials at finite temperatures. The coefficients of electric field induced Raman tensor (both amplitude and phase) and impurity induced raman tensor are also evaluated for <100> GaAs at 2.7eV (4579A).

In the last chapter we summarize the results and conclusions of our investigations.

Contents

ABSTRACT iii

ACKNOWLEDGEMENTS vi

PUBLICATIONS viii

INTRODUCTION xi

Chapter I: DISCUSSION OF MICROSTRUCTURAL GEOMETRIES . . 1

- Compositional Superlattices and Quantum Wells 2
  - Modified Kronig-Penney Model 5
  - Bastard Model 9
  - Schulman Model 10
- Doping Superlattices 11
- Space Charge Region 15

Chapter II: MODULATION SPECTROSCOPY 18

- Theory of Modulation Spectroscopy 18
  - Dielectric Function and Modulation Spectra 21
  - Low Field Limit (Third Derivative Spectra) 25
  - Franz-Keldysh Oscillations 30
  - Generalized Franze-Keldysh Oscillations 35
  - Mechanism of Photoreflectance 43
- Experimental Details 45
  - Electroreflectance 46
  - Photoreflectance 49
    - Elimination of False Signal 51
    - A New Servo Mechanism 54
    - Data Acquisition. 62
- Experimental Results 63
  - Photoreflectance: GaAs/AlAs Superlattices 63
    - Fit to Electromodulation Theory 63
    - Pump Wavelength Dependence (Depth Profiling) 70
  - Photoreflectance: GaAlAs/GaAs Multiple Quantum Wells 74
    - Topographical Variations 74
    - Forbidden Transitions 84

Electroreflectance: InP/ITO Space Charge Region 90
Photoreflectance: InP/ITO Space Charge Region 94
Photoreflectance: GaAs Doping Superlattices 101
Small Period Sample -- Quantum size effect 102
Large Period Sample -- FKO 107
Pumping Power Dependence 110
Chopping Frequency Dependence 112

Chapter III: RAMAN SPECTROSCOPY 118

General Background of Raman Scattering 116
Polarizability Theory of Raman Scattering 117
Microscopic Description 120
Selection Rules 124
Coupled LO Phonon Plasmon Modes. 127
Experimental Details 129
Experimental Results 132
Surface Charge Layer in <100> GaAs 132
Determination of Free Carrier Concentration 135
Measurements of Depletion Widths 138
Depletion Width at Finite Temperature 142
Electric Field and Impurity Induced Forbidden LO Scattering 150
Polish-Induced Surface Strain 157

Chapter IV: SUMMARY AND CONCLUSIONS 178

Bibliography 184

Figures

1. Schematic illustration of compositional superlattice and doping superlattices (nipi) 2

2. Schematic representation of the potential profile of a compositional superlattice 4

3. Schematic representation of the conduction, heavy hole and light hole states in a superlattice 7

4. Schematic representation of electron and hole in the nipi structure 12

5. Uncompensated doping superlattices 14

6. Schematic representation of the surface states and band bending in an N-type semiconductor. 17

7. Two categories of modulation mechanism 20

8. The Franz-Keldysh lineshapes 33

9. Space charge region modulation by a small ac field 38

10. Generalized Franz-Keldysh oscillation (real part) 41

11. Generalized Franz-Keldysh oscillation (imaginary part) 42

12. Effect of laser induced modulation in space charge region . . . 45

13. Schematic function block diagram of electroreflectance set up 47

14. Schematic function block diagram of photoreflectance set up 50

15. Photoreflectance spectrum from GaAs/GaAlAs quantum well normalized by conventional servo 57

16. Photoreflectance spectrum from GaAs/GaAlAs quantum well unnormalized 58

17. Photoreflectance spectrum from GaAs/GaAlAs quantum well normalized by variable desity filter 59

18. Photoreflectance spectrum from GaAs/GaAlAS quantum well normalized by numerical division 60

19. Comparison of third derivative and first derivative lineshapes 64

20. Photoreflectance spectra of GaAs/AlAs superlattices 66

21. Wavelength dependence of the photoreflectance signal from GaAs/AlAs superlattices 72

22. Photoreflectance spectra from GaAs/$Ga_{0.76}Al_{0.24}As$ multiple quantum well 77

23. Expand version of photoreflectance spectra from GaAs/$Ga_{0.76}Al_{0.24}As$ multiple quantum well 79

24. Photoreflectance spectra from $Ga_{0.76}Al_{0.24}As$/GaAs multiple quantum well 83

25. Forbidden transitions in room temperature Photoreflectance spectrum from $Ga_{83}Al_{0.17}As$/GaAs superlattices 86

26. Electroreflectance of InP/ITO at various dc bias 91

27. Electroreflectance of InP/ITO at various ac modulation voltage 93

28. Photoreflectance spectra of InP/ITO at various dc bias. 96

29. Surface filed as a function of bias voltage 98

30. Photoreflectance GaAs doping superlattices nipi497 103

31. Photoreflectance GaAs Doping superlattices nipi498 108

32. Photoreflectance PR spectra of GaAs nipi 498 for different dc pump power density. 111

33. Photoreflectance intensity as a function of ac pump

chopping frequency. 113

34. Schematic representation of modulation voltage in nipi 114

35. Kinematics of Stokes inelastic light scattering. 119

36. Two and three band Raman scattering 121

37. Coupled LO phonon-plasmon mode 129

38. Schematic function block diagram of Raman scattering 131

39. Room temperature Raman spectra of <100> GaAs 136

40. Schematic representation of the depletion width 144

41. Depletion width as a function of free carrier concentration 148

42. Electric field and impurity induced LO Raman scattering . . 152

43. Raman scattering from polished <100> GaAs and InP 161

44. Raman scattering from polished <111> GaAs and InP 163

45. Linewidth and peak shift as a function of optical skin depth for <111> GaAs and InP 164

46. Fit of LO lineshape for damaged <100> GaAs and InP 170

Tables

1. Energies, broadening parameters from the buffer and the substrate of a GaAs/AlAs superlattice 67

2. Comparison of experiment results and theoretical calculation of GaAs/AlAs superlattices 68

3. Comparison of fit with different order of derivatives 70

4. Energy and broadening parameters for various quantum transition at four position alone the body diagnal 80

5. Comparison of experiment results and theoretical calculation of $GaAs/Ga_{0.83}Al_{0.17}As$ supe~lattices including forbidden transitions 88

6. Comparison of experimental result and theoretical calculation of GaAs doping superlattices 105

7. Recombination life time of extra carriers in nipi498 115

8. The allowed Raman tensor 125

9. The linear q induced Raman tensor 126

10. Electric field induced Raman tensor 126

11. Strain induced Raman tensor 127

12. Free carrier concentration measurements 137

13. Depletion width measurement using 5 lines of an Ar^+ lasor . 140

14. Depletion width of various <100> GaAs samples experimentally 142

15. experimental results for various polishing conditions on <100> suurface 171

16. Experimental results for various polishing conditions on <111> suurface 172

Chapter I

DISCUSSION OF MICROSTRUCTURAL GEOMETRIES

Microstructural geometries are structures on the order of several lattice constant (10A) to several hundred lattice constants (about 1000A) including semiconductor superlattices (SL), quantum wells (QW), heterostructure interface, space charge region (SCR), microcrystalline effects, etc.

Superlattices and quantum wells [22] [23] [24] [25] are composed of a periodic sequence of ultrathin (about 100A) crystalline layers of alternating composition (e. g. AlAs/GaAs InAs/GaSb, Ge/Si, etc.) or alternating doping (e. g. n-GaAs/p-GaAS, n-Si/p-Si, etc. so called nipi structure) (Figure 1). Space charge region [6] [7] [26] [27] near the surface or interface of semiconductors is usually due to the Fermi level pinning. It can also occur with no pinning if there is an applied field. The band bending near the surface or interface results in a depletion layer as thin as 50A-1000A. In this thesis we only discuss QW, SL and SCR.

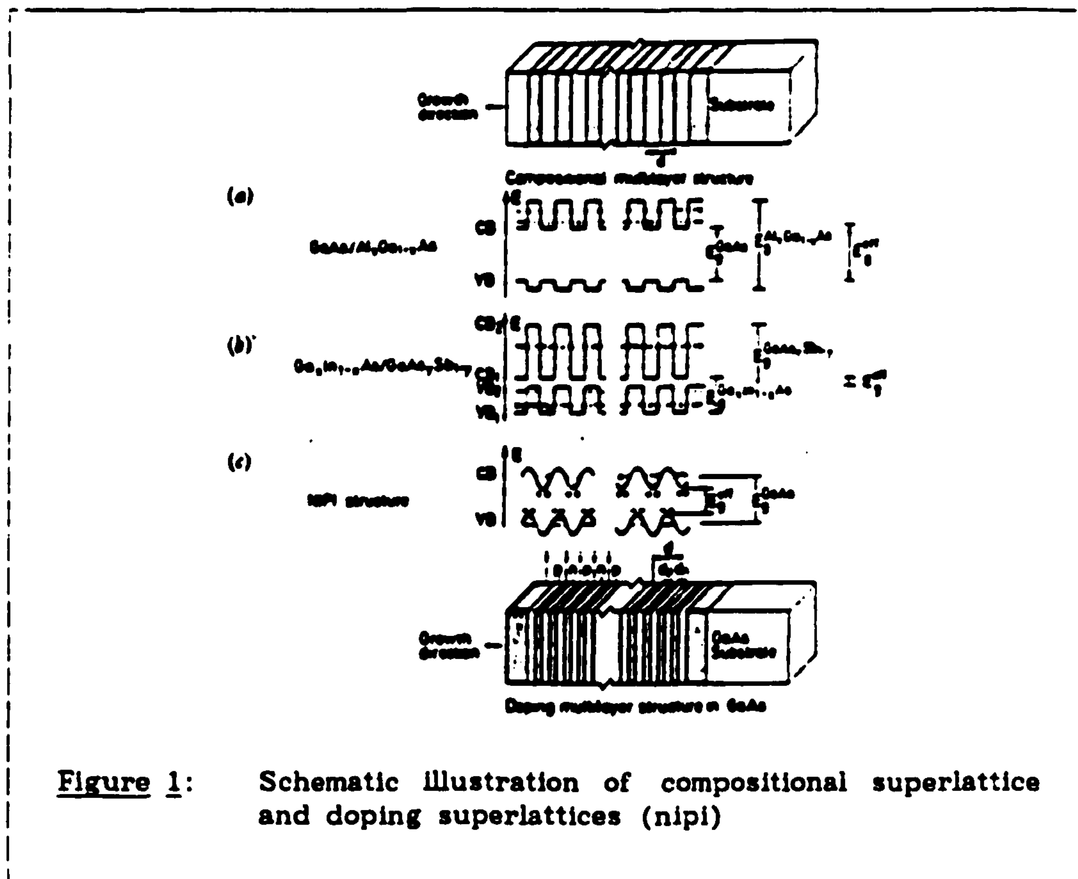

Figure 1: Schematic illustration of compositional superlattice and doping superlattices (nipi)

1.1 Compositional Superlattices and Quantum Wells

In a compositional SL the semiconductors are chosen so that their energy band gaps are different. The most straight forward way to determine the electronic properties in SL is to treat the SL as simply a series of semiconductor layers, with each layer contributing its characterizatic properties. More sophisticated calculations show that this

approach gives satisfactory results, even in the case of extremely thin layers. Thus, the periodic variation of the layers gives rise to a periodic alteration in the electrical potential. Inside each potential well only certain energy states are available to conduction (valence) band electrons (holes).

The components of the superlattice have energy band gaps E_g^{I} and E_g^{II} and layer thickness d^I and d^{II} (for example I=GaAs and II=GaAlAs). The energy gap difference

$$V_o = E_g^{II} - E_g^{I} \tag{1}$$

is divided into one part $V_{o,c}$ which appears as a discontinuity in the conduction band edge $E_c(z)$ and another part $V_{o,v}$, which modulates the the valence band edge $E_v(z)$, where z is the direction of the superlattices growth. This is illustrated in Figure 2.

Consider the square well potential in Figure 2. The states of the electrons (holes) in the z direction is quantized, yielding a number of discrete energies for the electron ($E_{c,n}$) and holes($E_{v,n}$). An estimate of the electron and hole energies based on an infinite well height gives

$$E_{c,n_c} = \pi^2\hbar^2 n_c^{\,2}/2m^*_c(d^I)^2 \tag{2}$$

$$E_{v,n_v} = \pi^2\hbar^2 n_v^{\,2}/2m^*_v(d^I)^2 \tag{3}$$

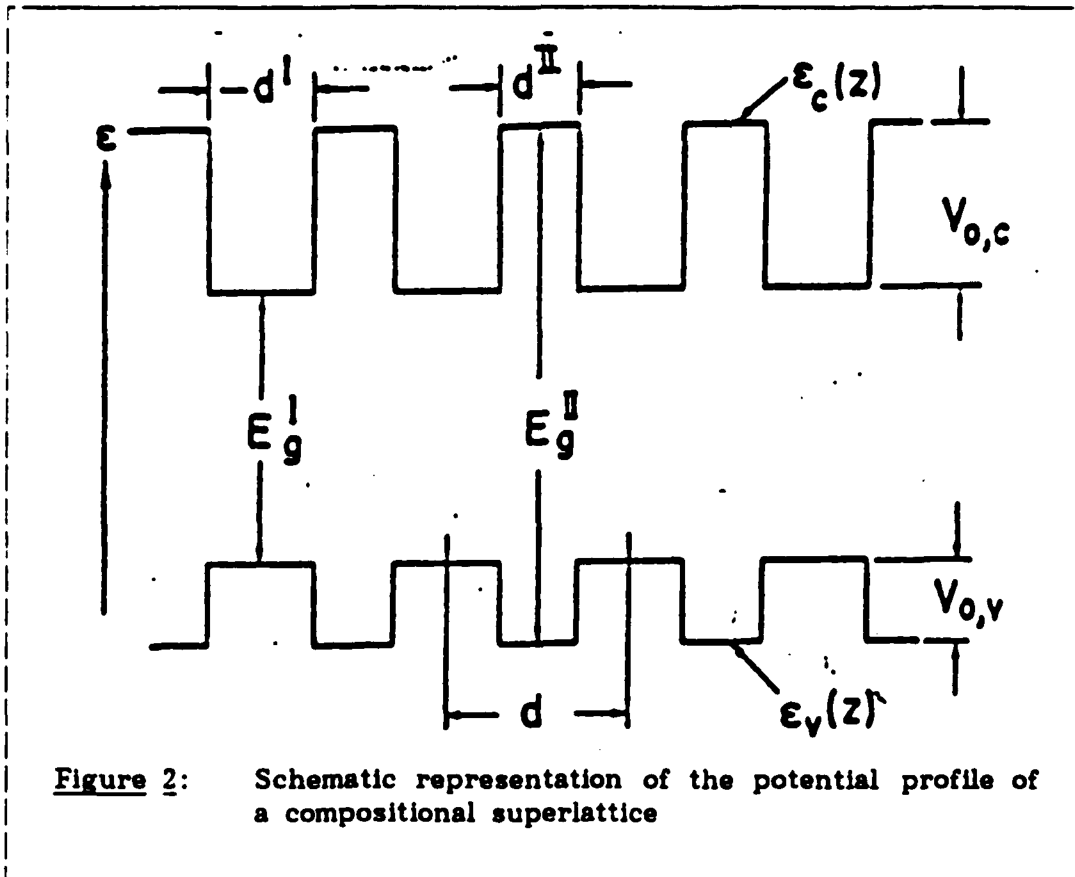

Figure 2: Schematic representation of the potential profile of a compositional superlattice

where m^*_c and m^*_v are the electron and hole effective masses (along z), respectively.

The above equations give a reasonable description for the lowest level of an isolated quantum well multiple quantum wells. A more detailed approach is required for the general case of a SL. There are several theoretical models presently available, i. e., the modified Kronig-Pennney model[28], two-band envelope function model (Bastard

model)[29] and multi-band tight-binding and envelope function model (Schulman model)[16] [30].

1.1.1 Modified Kronig-Penney Model

The Kronig-Penney model is described in quantum mechanics textbook [28]. The only difference with the textbook treatment is in the use of two masses for the two materials and the modified boundary conditions, i. e. $[1/m^*(z)][d\phi_{c,v}(z)/dz]$ continuous at the interface, where $\phi_{c,v}(z)$ is the envelope function for electrons and holes respectively, $m^*(z)$ is the effective mass along the growing direction z. This boundary condition insures the continuity of the probability current. The modified Kronig-Penney equation reads

$$\cos(qd)=\cos(k_I d_I)\cos(k_{II} d_{II})-1/2(x+1/x)\sin(k_I d_I)\sin(k_{II} d_{II}) \quad (4)$$

where

$$d=d_I+d_{II} \quad (5)$$

$$x=k_I m_{II}/k_{II} m_I \quad (6)$$

$$k^2_I = (2m^*_I E/\hbar^2)-k_\perp^2 \quad (7)$$

$$k^2_{II} = [2m^*_{II}(V_{o,c,v}-E)/\hbar^2]-k_\perp^2 \quad (8)$$

$k_\perp^2 = k_x^2 + k_y^2$, i. e., he momentum perpendicular to the superlattices direction and q is the wave vector in the subband.

Let us look more detail in the effectr of superiattices (or quantum well) potential on the band structure of the diamond and zincblende type material. The top of the valence band consists of a heavy hole (m_{HH}) and light hoie (m_{LH}) contribution. The degeneracy is a consequence of the cubic symmetry of these materials. The superlattice (quantum well) potential V(z) removes the degeneracy, i. e. it makes z inequivalent to x, y. Thus in SL (or QW) the conduction and valence states are shown in Figure 3. The splitting of the valence band into heavy and light hole subbands can also been seen from Eqs (2) and (3).

The selection rules for the optical transition can easily understood in term of the Kronig-Penney model. In fact the superlattice wave function $\Phi_{SL}(r)$ in the effective mass framework is written as a product of the Brillion zone center bulk Bloch function $\psi^0_{c,v}$ with a slowly varying envelope function $\phi_{c,v,n}(z)$ modifying along the superlattice axis

$$\Phi_{SL}(r) = \psi^0_{c,v} {}^* \phi_{c,v,n}(z) \tag{9}$$

the momentum matrix element P_{SL} related to optical transition can be written as

$$P_{SL} = \langle \psi^0_c {}^* \phi_{c,n_1}(z) | i\hbar\nabla | \psi^0_v {}^* \phi_{v,n_2}(z) \rangle$$

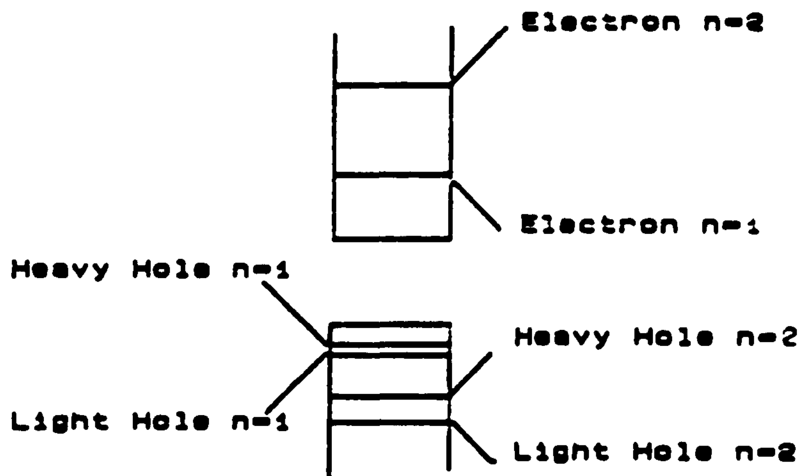

Figure 3: Schematic representation of the conduction, heavy hole and light hole states in a superlattices

$$=P_{cv} \langle \phi_{c,n_1}(z) | \phi_{v,n_2}(z) \rangle \qquad (10)$$

where $$P_{cv} = \langle \psi^0_c | i\hbar\nabla | \psi^0_v \rangle \qquad (11)$$

Thus only when $n_1=n_2$ or $\Delta n=0$, then interband dipole matrix are large. Although the overlap between other envelope functions is not exactly zero due to the difference between the conduction and valence band offset, it is small enough to give the quasiselection rule.

Up to now, the modified Kronig-Penney model is still the one most commonly used in the design of a SL. However, it frequently introduces error for the higher subbands. The reasons are : t'ₙ non-parabolicity of the bulk band structure, the mixing of the superlattices bands when they are close in energy and the mixing of light and heavy hole character for k not equal to zero.

1.1.2 Bastard Model

Calculation of the Bastard model begins with the 6x6 Kane matrix describing the k.p interaction within the Γ_6 and Γ_8 subspace [31]. By decoupling the heavy particle ($M_j=\pm 3/2$) from the light particles (electron and light hole $M_j=\pm 1/2$) , the Kane matrix can be transformed into two identical 2x1 differential systems (for describing coupling between light hole and electron) and two 1x1 systems (for describing heavy hole). The 1x1 equation leads to the same solution as the modified Kronig-Penney model, however the 2x2 equation introduces a small modification to the modified Kronig-Penney model, i. e. replace x by

$$x = k_I(E+Eg^{II}-V_o)/k_{II}(E+Eg^I) \tag{12}$$

The advantage of this method is that at almost no cost in terms of computational effect, it gives quite satisfactory results. The mixing of

the conduction band and the light hole is considered and the non-parabolicity of the bands is included in a natural way. We have compared Bastard model to the more sophisticated methods (Schulman's model). Results are very close for all the confined levels (within 1-2 meV). The discrepancies among published results for similar cases is due simply to the variations in bulk parameters assumed as input to the calculations, especially effective masses.

The disadvantage of the envelope function method is that it allows no mixing of two or more bulk states with widely separated wave vector and no mixing of bulk heavy hole and light hole states in the superlattice wave function. Thus although it gives the almost right energy positions of the subbands, it can not explain any forbidden transitions which frequently appear in experiments [12] [32] [33].

The limitation of the two band envelop function model is that the ratio of the bulk band gap to the effective mass in material I and II must be the same. Thus if the band gap and effective mass in the well are used, the choice must be make whether the band gap or the effective mass of the barrier , but not both , is also used. Y. C. Chang , etc. suggested that [34] it is preferable to use the effective mass to the energy gap. However, from an experimental point of view, the energy gap is a quantity which can be easily measured.

1.1.3 Schulman Model

J. N. Schulman, etc. have recently presented a multi-band tight-binding and envelope function method [16] [30]. They used five orbitals per atom (s,x,y,z,s*) and nearest-neighbor overlap to produce 20 Bloch states per material. By diagonaling the Hamiltonian formed by using the 40 Bloch functions, the superlattice function can be expanded as a linear combination of them. Their results showed that, the lowest superlattice conduction band states are primarily derived from the expected bulk states with wave vector near the center of BZ. The valence band states are more complicate in that the superlattice potential mixed the heavy-hole and light-hole state together. This type of mixture is especially strong when heavy-hole like and light-hole like states are close in energy for certain superlattice thickness. The mixing breaks down the optical selection rule $\Delta n = 0$ and has substantial effect on the optical properties of the superlattices. We will return to this point in the later section.

1.2 Doping Superlattices

In contrast to the compositional superlattices, doping superlattices [24] [35] [36] [37] consist of homogeneous bulk material modulated only by periodic n and p doping, possibly separated by undoped (intrinsic,

i) regions(nipi crystal). The periodic potential in doping superlattices is exclusively space-charge induced. As we are dealing with a homogeneous semiconductor, the effective mass approximation provides a very satisfactory description.

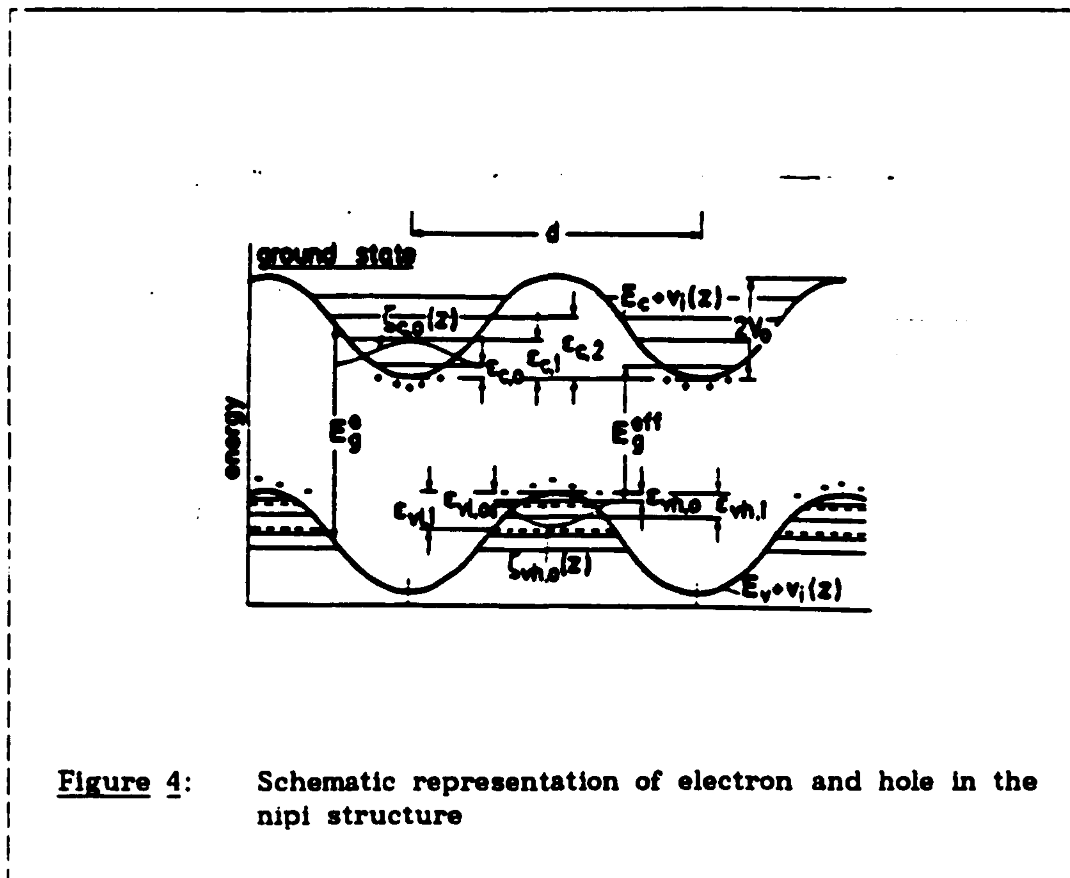

Figure 4: Schematic representation of electron and hole in the nipi structure

Consider the simplest nipi structure formed by a compensated doping with equal thickness $d_n=d_p$ for n and p doping layers, and equal doping concentration $n_d=n_a$. The period space charge potential in this case is parabolic and has an amplitude of

$$2V_o = 4\pi e^2 n_d d^2/4\varepsilon \tag{13}$$

where ε is the dielectric constant of the material and $d=d_n+d_p$. The subband energy and envelope function are exactly solutions of the harmonic oscillator equation. [24]

$$E_{c,v,n} = (n+\tfrac{1}{2})\hbar\omega_{c,v} \tag{14}$$

where

$$\hbar\omega_{c,v} = \hbar(4\pi e^2 n_d/\varepsilon m^*_{c,v})^{\frac{1}{2}} \tag{15}$$

$m_{c,v}$ is the effective mass for electron and hole respectively (see Figure 4). Since the electron and holes are separated in real space, their is no selection rule for optical transitions. The transition energies are

$$E_{n,m}=E_g-2V_o+(n+\tfrac{1}{2})\hbar\omega_c+(m+\tfrac{1}{2})\hbar\omega_v \tag{16}$$

where E_g is the energy gap of the host material.

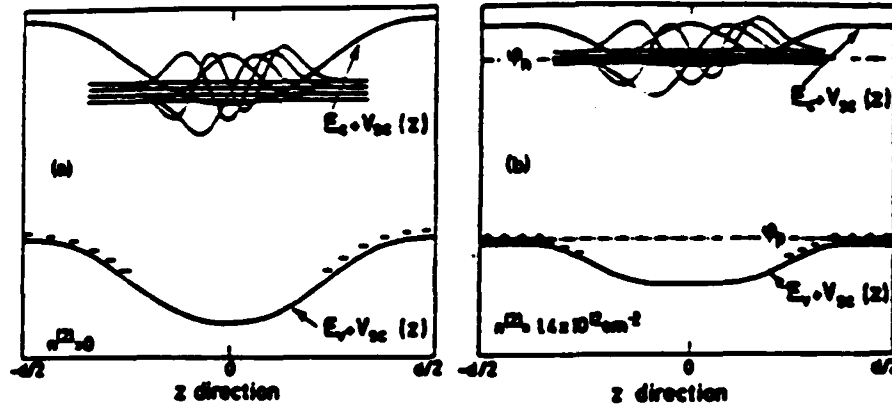

Figure 5: Uncompensated doping superlattices. a) small free carrier concentration. b) an intermediate value of free carrier concentration

In the case of an uncompensated doping superlattice, there is a finite (two dimensional) electron or hole concentration $n^{(2)}$ or $p^{(2)}$ in the n or p layer. Its value follows the neutrality condition

$$n^{(2)} = n_d d_n - n_a d_p \tag{17}$$

The spatial distribution of electrons, n(z) or holes, p(z) depends on the wavefunctions of the populated subbands and the number of carriers in these subbands. They have to be calculated self-consistently.

Ruden and Dohler etc. [38] reported a detailed study of the self-consistent calculation and showed that the free carriers have a significant probability to remaining at the center region of the respective layers (see Figure 5). Hence one can assume that the space charge is exactly neutralized in the central region of width $d_d = n^{(2)}/n_D$ and simply solve the effective mass equation with a flat bottom at the center of each layer (see Figure 5). This simply method was used in this thesis.

1.3 Space Charge Region

Extensive studies on Fermi level pinning and space charge region have been reported in the literatures [6] [7] [26] [27]. One model theory of Fermi level pinning in zincblende type semiconductor is the Defect Model [26]. In this model, a large density of surface states is assumed to been due to the defects (such as lack of As atom near the GaAs surface) or are associated with oxide layers and foreign absorbed materials. Most of the surface states are laying in the middle of the energy gap (see Figure 6). Fermi level at the surface is to be pinned in the position of the states (i. e. middle of the energy gap). Recent-

ly, J. M. Woodall, etc [27] have suggested a new model so called Effective Work Function Model (EWF). The EWF model assumes that the Fermi level location is de^^rmined by the work function of anions released from the bulk material (for example, As from GaAs or P from InP). For most of the III-V semiconductors (except InAs), the work function ϕ_P or ϕ_{As} is near the middle of the energy gap (see Fig. 1 in ref [27]). Because of the Fermi level pinning, free carriers near the III-V semiconductor surface are removed and only the bare ionized impurities are left. Under this fully depletion approximation, the Poisson's equation can been written as

$$d^2\phi/dx^2=4\pi e^2 n_d/\varepsilon \tag{18}$$

where n_d is the doping concentration. ε is the dielectric constant. The depletion width is

$$d_s=(\varepsilon V_s/2\pi e n_D)^{\frac{1}{2}} \tag{19}$$

and the surface electric field $\mathcal{E}_s$ is

$$\mathcal{E}_s^{\ 2} = 8\pi e n_D V_s/\varepsilon \tag{20}$$

where V_s is the surface band bending. Using the above equation, we can estimate the surface depletion width of GaAs (n_D=10^{18}-10^{19}cm^{-3}) being about 50A to 200A and the surface electric field as high as 10^6V/cm.

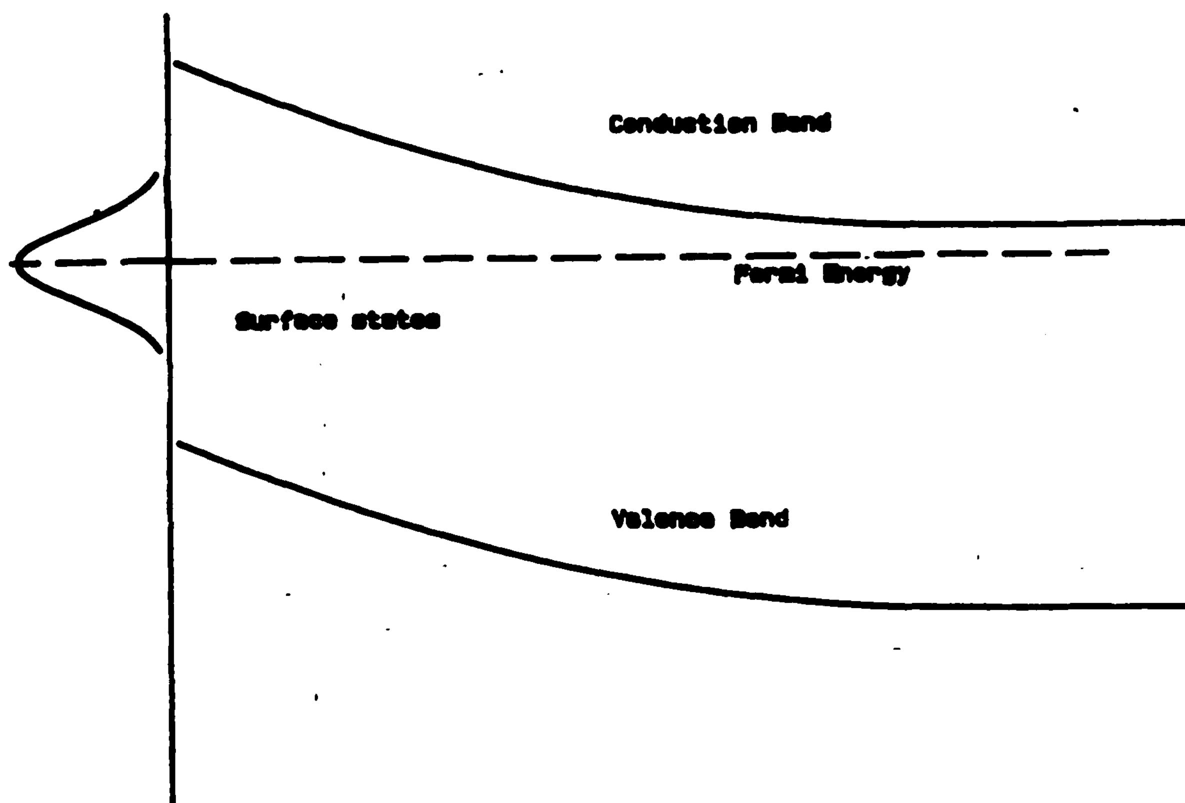

Figure 6: Schematic representation of the surface states and band bending in an N-type semiconductor.

Chapter II

MODULATION SPECTROSCOPY

2.1 Theory of Modulation Spectroscopy

The idea of modulation spectroscopy [2] [6] [7] [39] is a very general principle of experimental physics. Instead of directly measuring an optical spectrum, the derivative of the spectrum with respect to some parameter is measured. This can be easily accomplished by applying the parameters as a small perturbation in a periodic fashion and measuring the corresponding change in the optical properties with phase sensitive detector (i. e. with a lock-in amplifier). Structure in the conventional optical spectra is considerably enhanced in the derivative spectra and flat, structureless backgrounds are eliminated.

The modulation techniques can be classified into two categories: internal and external. In the internal modulation method, parameter of the monochromatic optical beam, such as the wavelength or the degree of polarization, is modulated. In the external method, an independent modulation parameter (e.g. a stress, an electric field, etc.) is applied to the sample. The internal method is simpler from the theoretical point

of view since it involves only the optical properties of an unperturbed solid. On the other hand, external method is simpler from the experimental point of view. In an internal modulation experiment the spectral distribution of the intensity and polarization properties of the incident beam produces spurious signal which can only be corrected by using a double beam system. In an external modulation experiment, however, the spurious signal can been removed easily, especially with a new servo mechanism developed in this thesis. We shall return to this point in the latter section.

The external modulation method can be subdivided into two categories according to the nature of the perturbation. Some perturbations (e.g. stress [40], temperature [41]) preserve the translational symmetry of the solid. In this case momentum conservation must be satisfied, i. e. $\Delta k = 0$ and either the energy gap or the broadening parameter or both have been modulated which usually gives rise to the first derivative-like spectra (see Figure 7a). Other perturbations partially destroy the translational invariance (e. g. electric field [6] and magnetic field [2]). In this case, forbidden transitions of $\Delta k \neq 0$ become allowed (see Figure 7b) which gives rise to complicated lineshapes usually corresponding to higher order derivative-like spectra. Interpretation of these kinds of spectra involves the rather formidable problem of

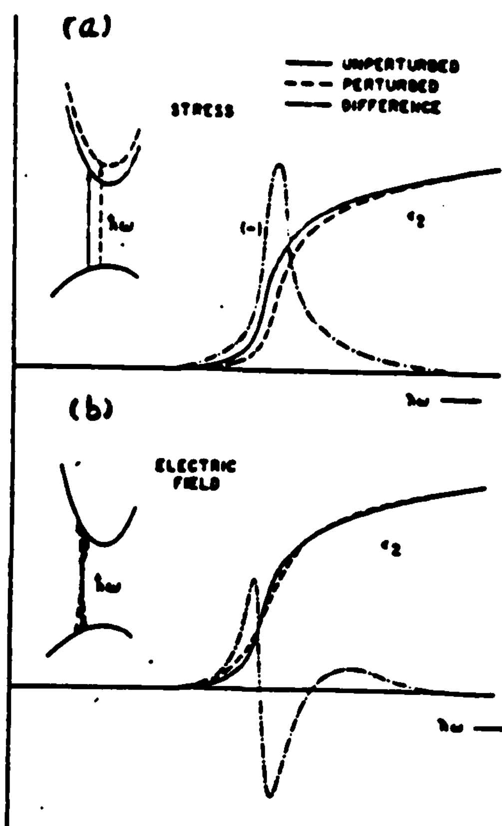

Figure 7: Two categories of modulation mechanism. a) First derivative modulation process where lattice periodicity is preserved. b) electric field modulation where lattice periodicity is not preserved.

the theory of the optical properties of the material in the presence of a perturbation. Since the $\Delta k \neq 0$ transitions are now add to the spectra, it can not and should not simplified to first derivative spectra.

Among all kind of modulations, electro modulation (including electroreflectance, electrolyte electroreflectance and photoreflectance) is the most powerful technique because of the sharpness of the spectra. In ER (electroreflectance) the field is modulated by applying the perturbating voltage across a MOS configuration, Schottky barrier or immersing the sample in an electrolyte (electrolyte electroreflectance EER). In PR (photoreflectance), the modulation is accomplished by photo-injected electron-hole pairs created by mechanically chopping a laser or other second light source of photo energy greater than the fundamental gap of the material. In this thesis we will only discuss the electromodulation techniques.

2.1.1 Dielectric Function and Modulation Spectra

The fundamental quantity which describes the optical response of the material is the complex dielectric function

$$\varepsilon(\omega) = \varepsilon_1(\omega) + i\varepsilon_2(\omega) = N^2 \qquad (21)$$

where $N=n+ik$ is the complex refractive index of the material. The real part (ε_1) and imaginary part (ε_2) of $\varepsilon(\omega)$ are related to those of N by:

$$\varepsilon_1 = n^2 - k^2 \tag{22}$$

$$\varepsilon_2 = 2nk \tag{23}$$

For near normal incidence, the reflectivity at the discontinuous interface between two different, but homogeneous media (substrate/ambient) can be written using Fresnel's equations as

$$R = |(N-N_a)|^2/|(N+N_a)|^2 \tag{24}$$

where N and N_a are the refractive indices of the material and the ambient, respectively.

The dielectric function exhibits features which are due to singularities in the combined density of states at certain points in the BZ called Van Hove singularities [42] or ' critical points '. To calculate modulation spectra(but not the dielectric function as a whole) we can write the dielectric function as a superposition of the local functions [6]

$$\varepsilon(E,\Gamma)=(Q/E^2)\Sigma(E_{cv}(k)-E-i\Gamma)^{-1} \tag{25}$$

where

$$Q=e^2\hbar^2|e.P_{cv}|^2/\pi m^2 \tag{26}$$

c,v denotes conduction (empty) and valence (filled) bands, respectively. The quantity **e** is the unit polarization vector of photon electric field, E is photon energy, m is the free electron mass and:

$$P_{cv} = \langle ck|\mathbf{p}|vk\rangle \tag{27}$$

is the momentum matrix.

$$E_{cv}(\mathbf{k}) = E_c(\mathbf{k}) - E_v(\mathbf{k}) \tag{28}$$

is the interband energy, and Γ is the phenomenological broadening parameter.

Because the region is local we may assume $P_{cv}(\mathbf{k})$ to be independent of **k**. Performing the integral in eq.(25) explicitly for one two, or three dimensions (for which two, one or none of the reduced interband effective masses m* are infinite), we have explicitly

$$\varepsilon(E,\Gamma) = \begin{cases} (Q/E^2) D_x D_y K_z i^{(l+1)} (E_g - E + i\Gamma)^{-\frac{1}{2}} & \text{1D} \\ (Q/E^2) D_x D_y K_z i^{(l+2)} \ln(E_g - E + i\Gamma) & \text{2D} \\ (2\pi Q/E^2) D_x D_y D_z i^{(l+1)} (E_g - E + i\Gamma)^{\frac{1}{2}} & \text{3D} \end{cases} \tag{29}$$

where

$$D_i = |2m^* \hbar^2|^{\frac{1}{2}}, \quad i = x,y,z \tag{30}$$

$K_l = K_y$ or K_z are the cutoff lengths in the brillouin zone for one and two dimensional critical points, and l is the critical point type which equal to the number of negative masses. We emphasize that the above equations are to be used to calculate difference or derivative spectra, and consequently, constant background terms do not appear.

In modulation experiments the perturbation changes the dielectric function ε. Let us assume that the real and imaginary parts of the dielectric function are changed by the amounts $\Delta\varepsilon_1$ and $\Delta\varepsilon_2$, respectively. Then it can be shown that

$$\Delta R/R = \mathrm{Re}\ \{2N_a \Delta\varepsilon / N(\varepsilon - \varepsilon_a)\} \tag{31}$$

$$= \mathrm{Re}\{(\alpha - i\beta)\Delta\varepsilon\} \tag{32}$$

$$= \alpha(\varepsilon_1, \varepsilon_2, \varepsilon_a)\Delta\varepsilon_1 + \beta(\varepsilon_1, \varepsilon_2, \varepsilon_a)\Delta\varepsilon_2 \tag{33}$$

where α and β are the Seraphin coefficients, which have a characteristic energy dependence for most semiconductors, ε_a is the dielectric constant of the ambient. In the next section we shall show how $\Delta\varepsilon_1$ and $\Delta\varepsilon_2$ are varied by an applied electric field.

2.1.2 Low Field Limit (Third Derivative Spectra)

Several method can be found in the literature [43] [44] [45] [46] [47] for the calculation of the dielectric function in the presence of low electric field. Most of derivations are algebraically complicated . We

here present a very simple semiclassical approach [48]. Although it is not rigorous the physical insight is quite transparent.

The physical mechanism responsible for electric field modulation is the coupling of the field to the electron (or hole), causing them to accelerate through the lattice and to occupy a range of k states before they undergo a collision process (see Figure 7b). There is another way of saying that an electron (or hole) occupies a range of energy in the band structure prior to a collision. This energy assists electron in tunneling though the gap and effectively reduces the energy gap.

The energy gain of electron and hole can be calculated using classical mechanics

$$E_{gain} = e^2 \mathcal{E}^2 t^2 / 2m^* \quad (34)$$

where m* is the interband reduced effective mass, t is time between two collision and is electric field.

The average energy (or the average energy uncertainty) during -t/2 to t/2 is

$$E_{gain} = e^2 \mathcal{E}^2 t^2 / 24m^* \quad (35)$$

The change in dielectric constant due to $\mathcal{E}$ is

$$\Delta\varepsilon = \varepsilon(E-E_{gain},\Gamma) - \varepsilon(E,\Gamma) \tag{36}$$

if the field is low enough so that:

$$E_{gain} < \Gamma \tag{37}$$

then we can make a Taylor's series expansion yielding

$$\Delta\varepsilon = -E_{gain}(d/dE)\varepsilon(E,\Gamma) \tag{38}$$

$$= -(e^2\mathcal{E}^2t^2/24m^*)(d/dE)\varepsilon(E,\Gamma) \tag{39}$$

In quantum mechanics

$$t = i\hbar(d/dE) \tag{40}$$

and thus:

$$\Delta\varepsilon = (1/3)(\hbar\Omega)^3(d^3/dE^3)\varepsilon(E,\Gamma) \tag{41}$$

where

$$\hbar\Omega = (e^2\mathcal{E}^2h^2/8m^*)^{1/3} \tag{42}$$

is the characteristic electro-optic energy of the system.

It can been easily seen that the electric field-induced change is related the third derivative with respect to energy of the unperturbed

dielectric function. This is in contrast to the first derivative nature of modulation techniques which preserve translation symmetry. Thus electro-modulation will give sharper structure. From the above equation we can also see that the lineshape of $\Delta\varepsilon$ is independent of field in the low field limit and its amplitude simply increases as the square of the field and inversely as the interband mass.

It is interesting to point out that this simple derivation, unlike any other sophisticated method, is independent of the unperturbed dielectric constant. It does not matter if the zero field dielectric function is Lorentzian-like or Gassian-like, the low field electric modulation is always the third derivative of the corresponding function as long as electron and hole can accelerate and gain energy from the electric field. We will return to this point when we discuss the mechanism of photoreflectance.

The inequality $E_{gain} < \Gamma$ gives the limit for the low field region. If we approximately take $t=\tau=\hbar/\Gamma$ the average collision time, then the energy gain prior to a collision will be

$$E_{gain}=e^2\mathcal{E}^2t^2/24m^*=(\hbar\Omega)^3/3\Gamma^2 \qquad (43)$$

Low field limit condition $E_{gain}<\Gamma$ reads

$$(\hbar\Omega)^3/\Gamma^3 < 1/3 \qquad (44)$$

Hence, the above low field limit is applicable to the intraband mechanism when the average energy gained per particle by acceleration in the field is small compared to the natural lifetime induced uncertainty. In practice the above low field limit is valid if the characteristic energy $\hbar\Omega < \Gamma$. In this limit the field enters only as a scaling prefactor $\mathcal{E}^2$. Experimentally this low field limit can be recognized whenever the spectral amplitude scales as $\mathcal{E}^2$, and no change is observed in the lineshape. Usually as a rule of thumb, this low field limit is applicable whenever $\Delta R/R \leq 10^{-4}$. Since the lineshape is field invariant, it is not necessary to use square wave modulation nor even to modulate from flatband provided that both dc and ac field satisfy $\hbar\Omega<\Gamma$.

Since the low-field electroreflectance (ER) structure of a single critical point is well localized within an energy range not exceeding several broadening parameters, the unperturbated dielectric function can be replaced with the local dielectric function discussed in last section, thus we can write:

$$(\Delta R/R) = \mathrm{Re}\{[Ce^{i\theta}(E-E_g+i\Gamma)]^{-n}\} \qquad (45)$$

where C and θ are the amplitude and phase factor which vary slowly with E, and hence can essentially be considered energy independent for small changes in E. The parameters C and θ determine the amplitude

and asymmetry of the lineshape, respectively, and E_g and Γ determine the location and width of the structure. For three dimensional critical points (i.e., all the effective masses are finite) n=2.5, and for two dimensional critical points (i.e., one of the masses is infinite) n=3 whereas n=3.5 for a one dimensional critical point. In the case of exciton, electric field modulates exciton binding energy as well as accelerates electrons and holes. The first one gives a contribution corresponding to n=2 ,while the second one corresponding to n=4.0

2.1.3 Franz-Keldysh Oscillations

If the low field limit is not valid, then a full quantum mechanical description must be used. Several different but equivalent methods have been reported in the literatures to calculate the dielectric constant in the presence of such an electric field [49] [50] [51] [52] [53] [54] [55]. We outline only the simplest, i. e., the stationary state approach in the effective mass approximation[50].

The calculation begins with the center of mass problem of the electron and hole

$$[(\hbar^2/2m^*)\nabla^2+e\mathcal{E}z+W_i]\phi_i(z) = 0 \qquad (46)$$

The solution of Eq(46) is given by :

$$\phi_i(z) = (e\mathcal{E}/\hbar\theta)\ Ai[(e\mathcal{E}z-W_i)/\hbar\theta] \qquad (47)$$

where

$$(\hbar\theta)^3 = e^2 \mathcal{E}^2 \hbar^2 / 2m^* \tag{48}$$

and Ai is the Airy function.

The imaginary part of the dielectric function is proportional to the probability of finding electron and hole at the same position, i. e.

$$\varepsilon_2(E) = (Q'/E^2)\ \Sigma\ |\phi(0)|^2 \delta(W_i - E) \tag{49}$$

substituting $\phi(0)$ from Eq(47) into the above equation yields the result:

$$\varepsilon_2(E, \mathcal{E}) = (Q'/E^2)(\hbar\theta)^{\frac{1}{2}} \pi [Ai'^2(\eta) - \eta Ai^2(\eta)] \tag{50}$$

$$\varepsilon_2(E, 0) = (Q'/E^2)(\hbar\theta)^{\frac{1}{2}} (E - E_g)^{\frac{1}{2}} H(E - E_g) \tag{51}$$

where H(x) is the step function and

$$Q' = (2e^2\hbar^2/m^2)|e.P_{cv}|^2(2m^*/\hbar)^{3/2} \tag{52}$$

$$\eta = (E_g - E)/\hbar\theta$$

This result and its Kramers-Kronig transform (i. e., $\Delta\varepsilon_1$) can be expressed as:

$$\Delta\varepsilon(E, \mathcal{E}) = (Q'/E^2)(\hbar\theta)^{\frac{1}{2}}[G(\eta)+iF(\eta)] \tag{53}$$

where

$$F(\eta) = \pi[Ai'^2(\eta)-\eta Ai^2(\eta)]-(-\eta)^{\frac{1}{2}}H(-\eta) \tag{54}$$

$$G(\eta) = \pi[Ai'(\eta)Bi'(\eta)-\eta Ai(\eta)Bi(\eta)]+(\eta)^{\frac{1}{2}}H(\eta) \tag{55}$$

The lineshape factor G and F, plotted as field induced changes in real and imaginary part of dielectric function are shown in Figure 8.

The physical picture of Franz-Keldysh oscillations is photo-assisted indirect interband transitions in the real space. Franz-Keldysh oscillation is also sometimes called photo-assisted tunneling. Transitions between valence band and conduction band are now possible for energy smaller then E_g through the quantum effect, which corresponding to the exponential tail in Figure 8 for $\eta>0$. Transitions above the energy gap ($\eta<0$) show resonance effects, wherever the distance the electron travels equals an integer number of de Broglie wavelength, which corresponding to the periodic peaks in Figure 8.

Using the asymptotic expression of the Airy function [56]

$$Ai(\eta) = \pi^{\frac{1}{2}}(-\eta)^{-1/4}\sin[(2/3)(-\eta)^{3/2}+\pi/4] \tag{56}$$

Notice that:

$$(\hbar\theta)^3 = (\hbar\Omega)^3/4 \tag{57}$$

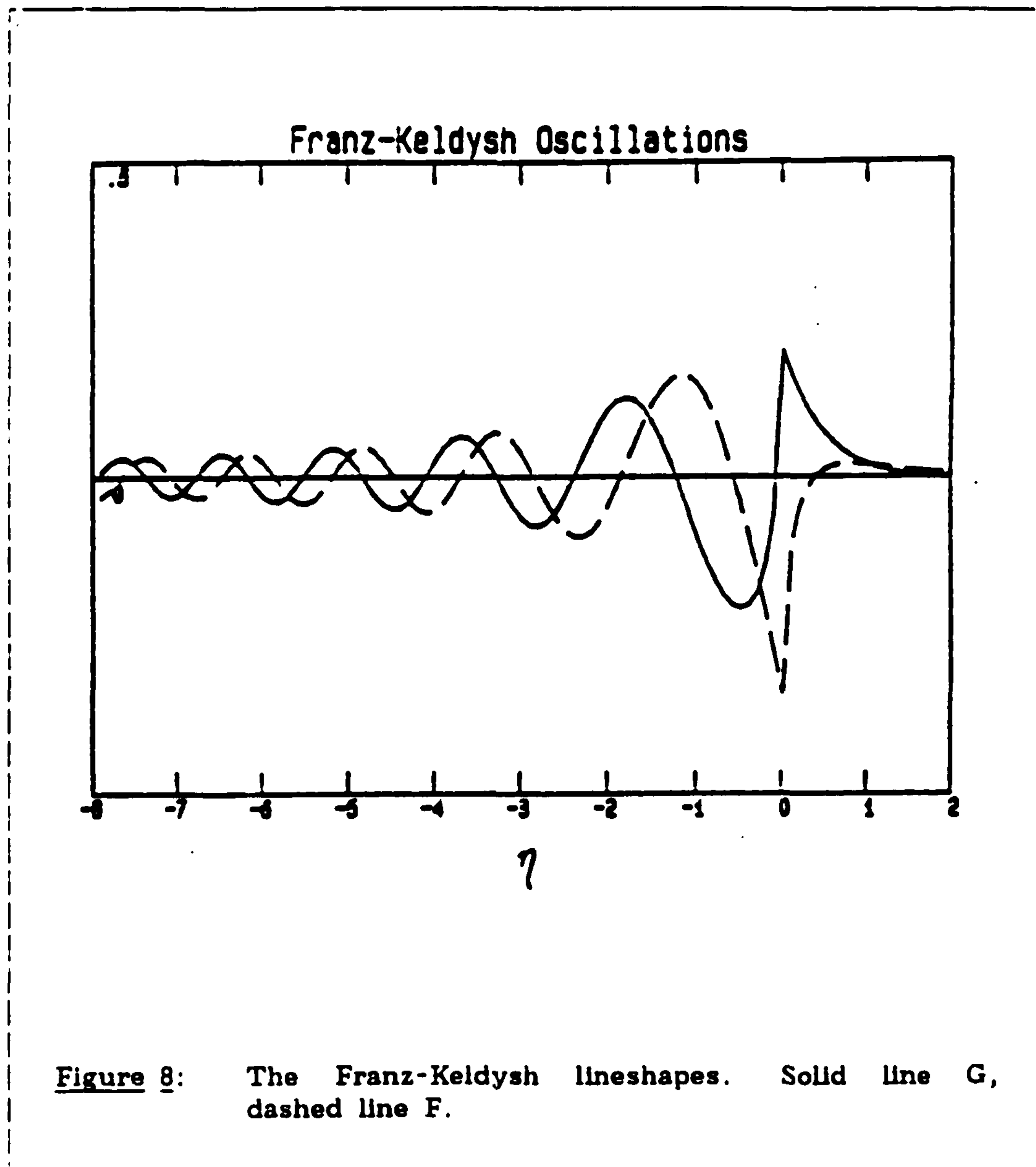

Figure 8: The Franz-Keldysh lineshapes. Solid line G, dashed line F.

The energy at the peak of the νth half oscillation is determined by the relation:

$$\nu\pi = \theta + (2/3)[(E_\nu - E_g)/\hbar\Omega]^{3/2} \tag{53}$$

Thus a plot of extremum number ν versus $2/3(E_\nu - E_g)^{3/2}$ yields a slope of $(\hbar\Omega)^{-3/2}$. Since $\hbar\Omega$ contains information about effective mass and the electric field, it is important to observe as many oscillations as possible. In order to do so , a uniform modulation from the flat band was suggested by several authors [57] [58]. That usually required a nearly intrinsic sample. In heavily doped semiconductors, the electric field is always inhomogeneous since the penetration depth of field is so small. We will demonstrated in next section that an homogeneous modulation can also be obtained by applying a small ac modulation field.

2.1.4 Generalized Franze-Keldysh Oscillations

The above FKO theory is based on modulation from flat band and do not take into account the presence of large build in dc field (e.g. in the space charge region of heavily doped material or nipi structures). We will show below that if the dc field is considerable larger than the modulation field, the period of the KFO are a measure of the former field, not the latter.

Including a dc electric field($\mathcal{E}_{dc}$), the change of dielectric function due to the ac modulation($\mathcal{E}_{ac}$) can be written as

$$\delta\varepsilon(E, \mathcal{E}_{dc}, \mathcal{E}_{ac}) = \varepsilon(E, \mathcal{E}_{dc}+\mathcal{E}_{ac}) - \varepsilon(E, \mathcal{E}_{dc}-\mathcal{E}_{ac}) \quad (59)$$

$$= \Delta\varepsilon(E, \mathcal{E}_{dc}+\mathcal{E}_{ac}) - \Delta\varepsilon(E, \mathcal{E}_{dc}-\mathcal{E}_{ac}) \quad (60)$$

if $\mathcal{E}_{ac} << \mathcal{E}_{dc}$ then

$$\delta\varepsilon(E, \mathcal{E}_{dc}, \mathcal{E}_{ac}) = 2\mathcal{E}_{ac}(d/d\mathcal{E}_{dc})\Delta\varepsilon(E, \mathcal{E}_{dc}) \quad (61)$$

Using relations between Airy functions and their derivatives, we have explicity

$$\delta\varepsilon(E, \mathcal{E}_{dc}, \mathcal{E}_{ac}) = (4/3)(\mathcal{E}_{ac}/\mathcal{E}_{dc})(Q'/E^2)(\hbar\theta)^{\frac{1}{2}}[\tilde{G}(\eta)+i\tilde{F}(\eta)] \quad (62)$$

where

$$\tilde{F}(\eta) = (\pi/2)[Ai'^2(\eta)+\eta Ai^2(\eta)] \quad (63)$$

$$\tilde{G}(\eta) = (\pi/2)[Ai'(\eta)Bi'(\eta)+\eta Ai(\eta)Bi(\eta)] \quad (64)$$

Since η is related to the dc field, the FKO now is determined by $\mathcal{E}_{dc}$ not the modulation field $\mathcal{E}_{ac}$. Thus FKO provides a direct optical measure of the surface (or interface) field.

In order to compare this result to the experiment, one must take into account the inhomogenities of the field. Aspnes and Frova [57] pointed out that, in the presence of non-uniform field, an approximate

solution of Maxwell equation in the simple local uniform perturbation approximation leads to an expression for the effective change in dielectric constant is

$$<\Delta\varepsilon> = 2ik \int_0^{d_s} \Delta\varepsilon(z)e^{-ikz}dz \tag{65}$$

In the fully depleted space charge region the electric field changes linearly in the SCR

$$\mathcal{E}(z) = \mathcal{E}_s(d_s-z)/d_s \qquad (0<z<d_s) \tag{66}$$

where $\mathcal{E}_s$ is the electric field at the surface. d_s is the depletion width. For a very short field penetration depth (i. e. heavily doped material) the effective change of dielectric function is

$$<\Delta\varepsilon> = iC \int_0^{\mathcal{E}_s} \Delta\varepsilon(\mathcal{E})d\mathcal{E} \tag{67}$$

where C is a real constant. When applying an ac modulation, the surface field $\mathcal{E}_s$ will change from $\mathcal{E}_{dc}-\mathcal{E}_{ac}$ to $\mathcal{E}_{dc}+\mathcal{E}_{ac}$, however the slope of electric field keeps constant (see Figure 9) provided that net free carriers in SCR is negligible compare to the impurity concentration. The net charge of dielectric constant due to the ac modulation is

$$\langle \delta\varepsilon \rangle = iC \int_{\mathcal{E}_{dc}-\mathcal{E}_{ac}}^{\mathcal{E}_{dc}+\mathcal{E}_{ac}} \Delta\varepsilon(\mathcal{E})\, d\mathcal{E} \qquad (68)$$

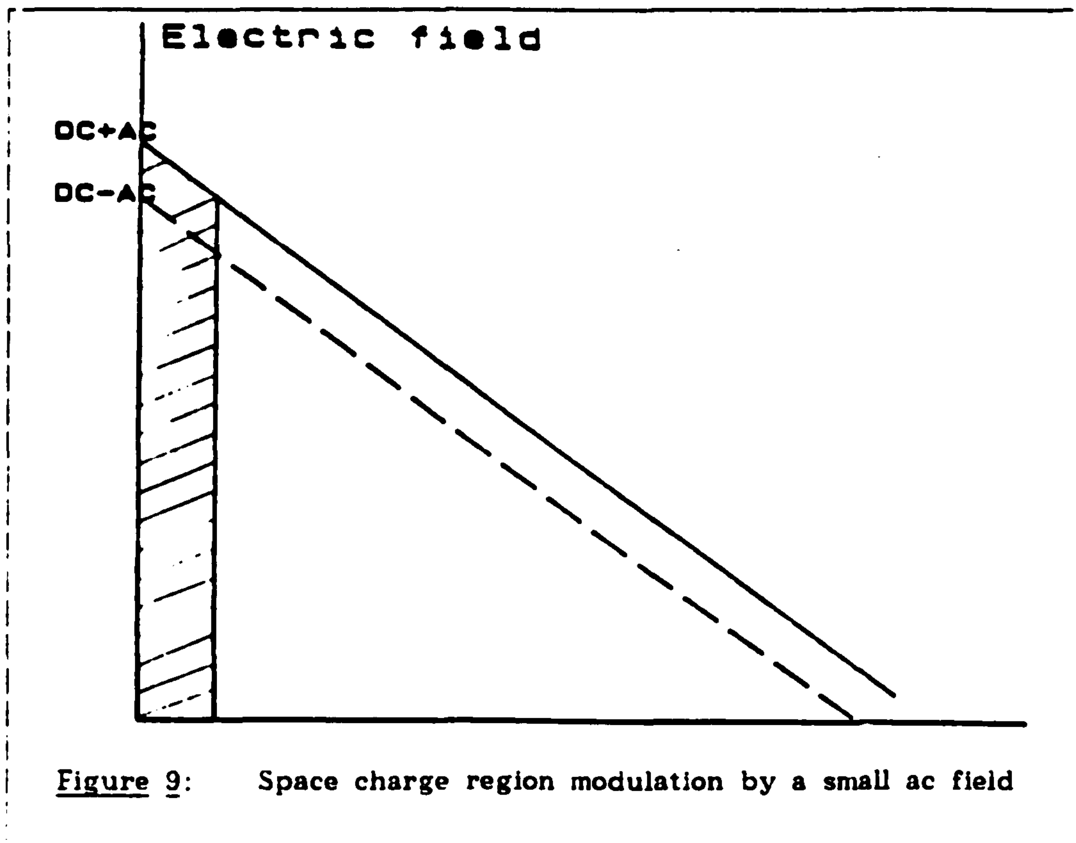

Figure 9: Space charge region modulation by a small ac field

In order to compare this result to the uniform modulation case, we write electric field in unit of $\mathcal{E}_{dc}$

$$\xi = \mathcal{E}_{ac}/\mathcal{E}_{dc} \tag{69}$$

$$\varepsilon = (E_g - E)/\hbar\theta_{dc} \tag{70}$$

$$(\hbar\theta_{dc})^3 = e^2\hbar^2\mathcal{E}_{dc}{}^2/2m^* \tag{71}$$

The lineshape of SCR modulation can be given in terms of two generalized Franz-Keldysh function $\overline{F}(\eta,\xi)$ and $\overline{G}(\eta,\xi)$

$$\delta\varepsilon(E, \mathcal{E}_{dc}, \mathcal{E}_{ac}) = C\,\mathcal{E}_{dc}{}^{1/3}\mathcal{E}_{ac}[\overline{F}(\eta,\xi) - i\overline{G}(\eta,\xi)] \tag{72}$$

where

$$\overline{F}(\eta,\xi) = (1/2\xi)\int_{1-\xi}^{1+\xi} x^{1/3}F(\eta/x^{2/3})dx \tag{73}$$

$$\overline{G}(\eta,\xi) = (1/2\xi)\int_{1-\xi}^{1+\xi} x^{1/3}G(\eta/x^{2/3})dx \tag{74}$$

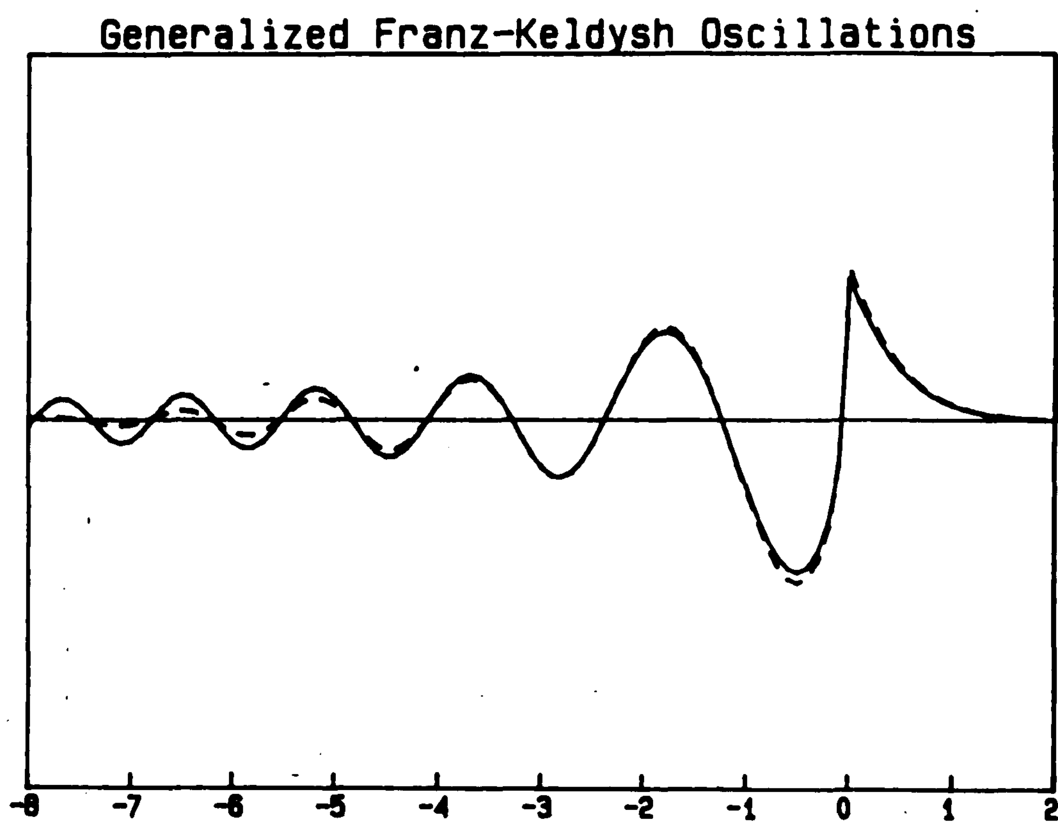

Figure 10: Generalized Franz-Keldysh oscillation (real part). Solid line $\mathcal{E}_{ac}/\mathcal{E}_{dc}=0.01$ dashed line $\mathcal{E}_{ac}/\mathcal{E}_{dc}=0.2$

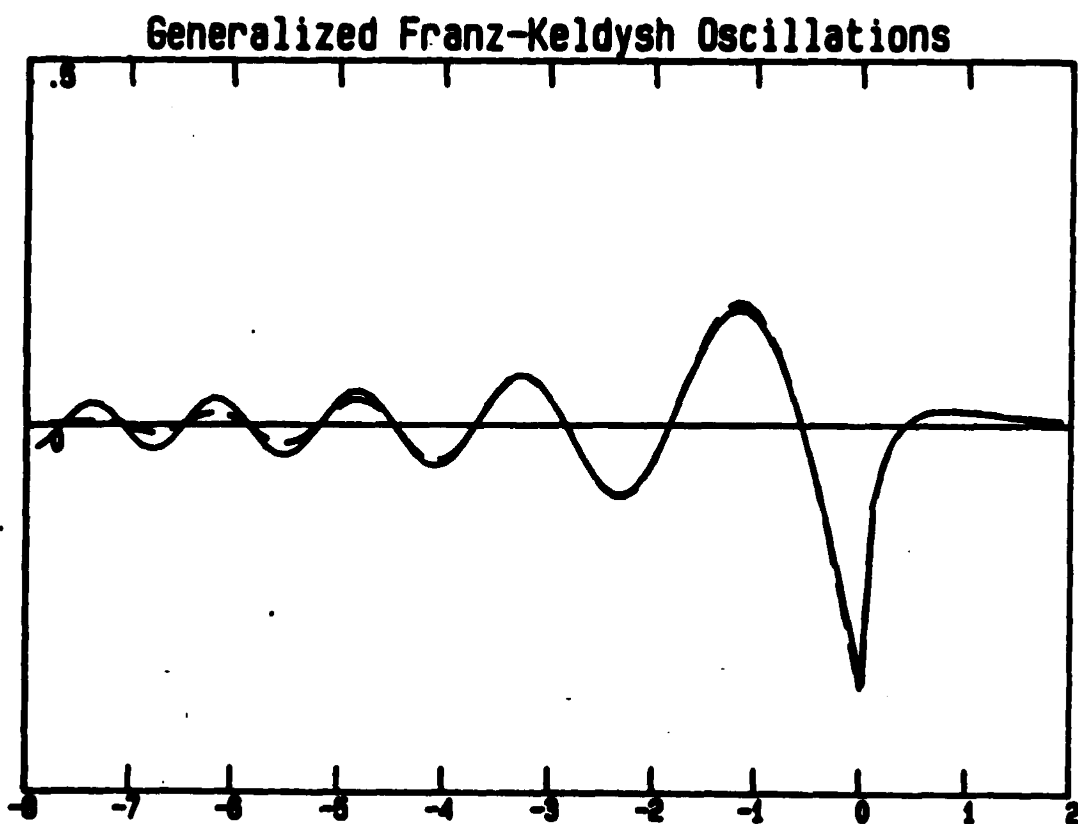

<u>Figure</u> <u>11</u>: Generalized Franz-Keldysh oscillation (imaginary part). Solid line $\mathcal{E}_{ac}/\ \mathcal{E}_{dc}=0.01$ dashed line $\mathcal{E}_{ac}/\ \mathcal{E}_{dc}=0.1$

The lineshapes $\overline{G}(\eta,\xi)$ and $\overline{F}(\eta,\xi)$, plotted in unit of $\hbar\theta_{dc}$ for different ξ, (i. e. the ac filed) are showing in Figure 10 and Figure 11 As can be seen that the period is almost independent of ξ (the ac modulation). The major effect of ac modulation is smear out the high order oscillations.

The physical picture of the above result is the effective modulation shown in Figure 9. The solid line corresponds to the positive half cycle of the ac modulation and the dashed line corresponds to the negative half cycle. The difference between them is the shadowed area. If $\mathcal{E}_{ac}$ is small, the effective modulation is from flat band to $\mathcal{E}_{dc}$. The shadowed trapezoid approaches a thin rectangle. It is also clear mathematically that

$$\lim_{\xi\to 0} \overline{G}(\eta,\xi) = G(\eta) \tag{75}$$

$$\lim_{\xi\to 0} \overline{F}(\eta,\xi) = F(\eta) \tag{76}$$

formal uniform FKO formula recovered when $\xi=0$. When ac increases the effective modulation covers a region from $\mathcal{E}_{dc}-\mathcal{E}_{ac}$ to $\mathcal{E}_{dc}+\mathcal{E}_{ac}$. Thus the $\mathcal{E}_{ac}$ field produces an equivalent non-uniformity modulation. Although it does not change the period significantly, it does smear the high order oscillations. In order to get more oscillations, a relatively

small ac (<0.05) is appropriate. On the other hand, the intensity ratio of the neighboring maximum may be used as an optical method to obtain the ac/dc ratio.

2.1.5 Mechanism of Photoreflectance

In the case of PR a modulation of the optical constants occurs because of the photoinjunction of electron-hole pairs by a secondary (or pump) light beam. These free carriers can perturb the reflectivity by various mechanisms including: 1) the screening of excitons, 2) a Burstein-Moss effect (band filling effect), 3) a reduction of the built-in surface (or interface) field through a recombination of minority species with charge in surface (or interface) states. All of the mechanisms given above may be operative and even dominant, depending on the circumstances. However, in our experiments, mechanism (3) (=electroreflectance) seems to be most important [6].

First the Burstein Moss effect (band filling effect) is negligible in our highest pump intensity (about $10mW/cm^2$ and corresponding to the free carrier concentration less than $3x10^6cm^{-3}$). Our experiment showed that the ratio of different PR features remained constant even photon energy of the secondary light beam was below those transitions as long as photon energy is above the fundamental gap of the material. Thus it rules out the band filling effect in our experiment completely.

The screening of exciton effect was also small for the carrier concentration mentioned above [59]. For most of the QW and SL we have studied, the PR spectrum was insensitive to the change in the intensity of either the pump or probe beam. It ruled out the possibility of screening effects.

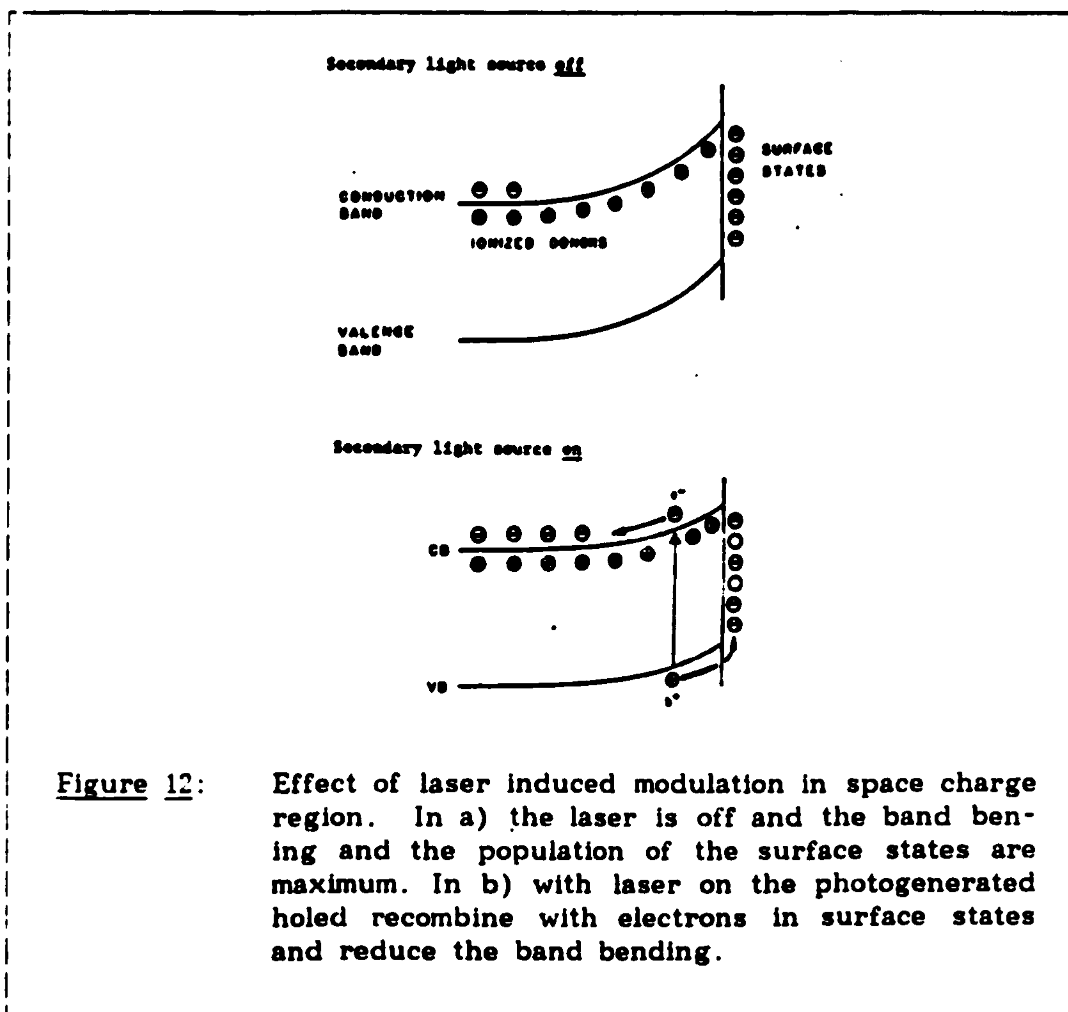

Figure 12: Effect of laser induced modulation in space charge region. In a) the laser is off and the band bending and the population of the surface states are maximum. In b) with laser on the photogenerated holed recombine with electrons in surface states and reduce the band bending.

The reduction of built-in surface electric field is shown schematically in Figure 12 for an n-type semiconductor. In the upper portion (secondary light off) the band bending and the populatic- of surface (intorface) states as at maximum. In the lower portion, with secondary light on, there are photo-excited electron-hole pairs. These photo-excited holes move toward the surface and recombine with electrons in the surface states and hence reduce the band bending. This cause a modulation of the space-charge region electric field. The lineshape of PR in this case is identical to the electroreflectance lineshape. We shall be back to this point in latter section.

2.2 Experimental Details

2.2.1 Electroreflectance

In this section we describe in detail the experimental setup and the details of the method in ER spectroscopy.

The schematic of the experimental setup for the ER system is shown in Figure 13

Light from a 150 watt Xenon arc is passed through the monochromator (in our case PTI Model 01-002 [60]). The monochromatic light coming through the exit slit is focused onto the sample by means of a spherical mirror or a lens. The modulating voltage is applied between

the sample and the indium-tin oxide (ITO) layer, which was deposited to a thickness of about 500 A by ion beam sputtering, and has a carrier concentration of about 10^{21} cm^{-3}. The energy gap of ITO is about 3.5 eV, hence it is transparent at the region of our interesting (1.2-2.0 eV).

The modulating voltage is a square wave at 200 Hz from a function generator (HP model 3311 A), which also provides reference signal to the lock-in amplifier (SR510 Lock-in amplifier made by Stanford Research Systems). The reflected light is collected by the photomultplier tube (PMT S-1 for 8000A-1100A or S-20 for 2000A-8000A) or a silicon photodiode for 3000A-10000A.

The reflected light collected by the PMT has a large dc intensity corresponding to the product of the incident light intensity I_0 and the average sample reflectivity R. Superimposed on this large dc signal is a small modulation with an amplitude $I_0\Delta R$, ΔR being the change in R due to the modulating field. Hence the output of the PMT contains a dc part proportional to I_0R and an ac part proportional to $I_0\Delta R$, which varies with the modulating frequency. Hence the ratio of the ac part to the dc part gives $\Delta R/R$. The changes $\Delta R/R$ was typically 10^{-4}~10^{-6}. These changes can easily be detected by the usual phase sensitive detection techniques. The dc output I_0R of the PMT is fed into a ser-

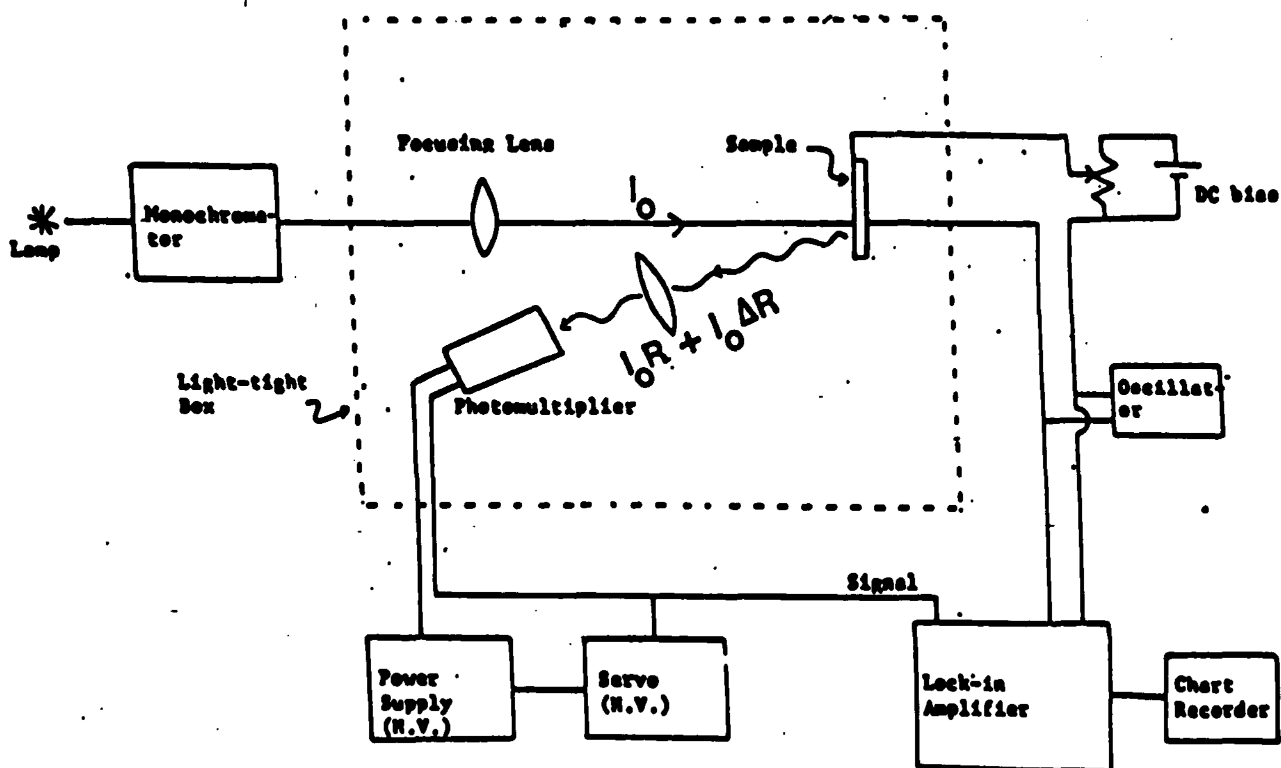

Figure 13: Schematic function block diagram of electroreflectance set up

vo amplifier (mechanical or electronic) which adjusts the high voltage of the PMT in order to keep the dc output I_0R, a constant. The ac component of the output signal $I_0\Delta R$, is detected by the lock-in amplifier. The output signal of the lock-in amplifier is proportional to $\Delta R/R$, the relative change in reflectance.

The servo mechanism automatically corrects for any fluctuations in the reflected intensity due to : (a) changes in the incident light intensity (a common problem in arc lamps), (b) changes on the surface of the sample. Thus in normalized modulated spectra, it is not necessary to collect the entire reflected light from the sample surface since the common factor I_0 is eliminated.

In the event that detector such as Si or Ge photodiodes are required, a new servo mechanism was developed. We will discuss it in the next section

2.2.2 Photoreflectance

The schematic of the experimental set up for Photoreflectance is show in Figure 14. The modulation is accomplished by mechanically chopping a laser or other secondary (pump) light source of photon energy greater than the fundamental gap of the material. In our experiment, the modulating light source was one of the following a) the 6328 A line of a He-Ne laser , b) the 4579 or 5145 A lines of a Ar^+ las-

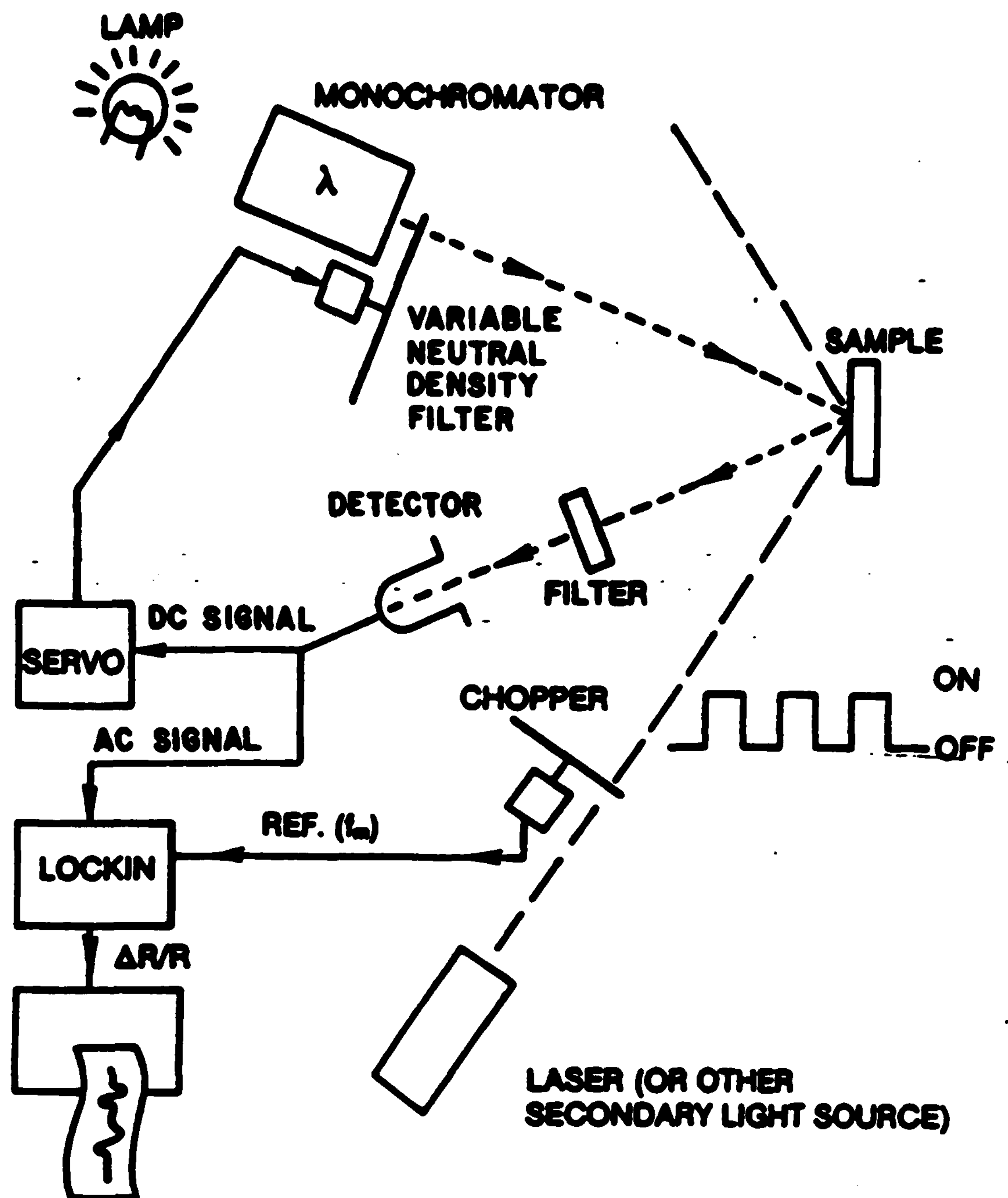

Figure 14: Schematic function block diagram of photoreflectance set up

er, c) the light in the region of 2000A to 10000A from a second monochromator with a Xenon arc source. The chopper frequency was nominally at 100Hz *^ 200Hz (PTI Model 03-0c400) [60]. The measurement is carried out similar to ER . Light from a white light source (Xenon arc, tungsten lamp) is dispersed by a monochromator (probe beam) and then reflected from the sample. The reflected light is usually pass through a filter or a pin hole collimator to limit the false signal (discussed in next section) and is then detected by a PMT or Si detector. The signal from the detector is then processed by a lock-in amplifier tuned to the modulation frequency of the second light source.

2.2.2.1 Elimination of False Signal

Two of the main problems in photoreflectance measurement is to eliminate a) diffuse reflected light from the modulation source and b) photoluminecence produced by the intense pump light. Both of them may reach the detector and be picked up by the lock-in amplifier.

The diffuse reflected light depends quite strongly on the quality of the sample surface and the optical geometry. We found that by normal incident of the pump beam, the diffuse reflectance signal can be reduced to a minimum. The best way to eliminate it is using a suitable filter to prevent the pump light from reaching to detector. For 6328A He-Ne line, a 7000A long pass filter (RG700 made by Melles Griot) was

used. For 4579A and 5145A of Ar^{+} lines, either 4900 long pass or 5900 long pass filter was used. Usually these filters cut the diffuse light to 10^{-3}. However, because of lack of good quality low pass and band pass filter, this method can not employed to observe those features above the pump energy. In order to get the spectra above the pump energy, a proper choice of filter is quite difficult and hence other methods must be applied. There are also more fundamental reasons to carrier out the experiment without using a filter. For instance ,in the pump wavelength dependence experiment or in resonant PR experiment, the pump beam is from a monochromator and its energy must step continuously into the region of PR spectra. Then no filter can be used in this case.

The spurious signal from photoluminecence has been found small for bulk material at 300K or nipi structures, except at very low temperature. But it was greatly enhanced for quantum well and superlattice because of the confinement of electron and hole inside the same well. For example, the photoluminecence signal from a typical PR experiment on a good quality QW at 77°K may be as 2-20 times bigger than the PR signal and causes the major problem in the PR experiment. Since the photoluminecence signal is at the same region as PR spectra or lower, no suitable filter can be used to prevent it from reaching the detector.

A number of alternate methods have been used to enhance the rejection of the false signal (both diffuse reflection and photoluminecence). They are discussed below:

1. A proper choice of the pumping power is essentially important. The false signal (both diffuse reflection and photoluminecence) is proportional to the pump power. However the photoreflectance signal varies approximately proportional to the logarithmic scale of the pump power. The use of more powerful light source as the pump beam does not increase significantly the signal to noise ratio, however it does increase the long term drift because the instability of the pump light source and the experimental environment. We found a power density being about $10mW/cm^2$ is sufficient for most of the samples.

2. A second spherical lens was used to focus the reflected light from the sample surface down to a very small spot (about 0.5mm in diameter). The aperture of this lens is adjusted to collect all the reflected light but nothing more. An adjustable pin hole collimator was place at the focal point and was adjusted so that the ratio of PR signal to spurious signal was optimized. This method is equivalent to restrain both the solid angle and the area of interest on the sample surface. It is found that a good

optical adjustment can reduce the false signal to a factor of 10 to 100.

3. A beam splitter was placed in the path of the pumping beam. A second detector was used to monitor the pumping power. The signal from both detectors are than sent to a difference amplifier, and the gain of the second one is adjusted so to cancel the spurious signal. This method is better than using a dc offset at the end of the lock-in. Since the false signal is proportional to the pumping power , this kind of auto offset will eliminate most of the drift from the instability of the pump beam. However the price of this method is introducing additional noise from the second detector. And also it is not a good practice in experimental physics to extract weak structures from a big background by subtraction. Therefore this method is only used with combination of other methods to eliminate the small residual background.

4. Instead of using the light from a monochromator as a probe beam, a tunable dye laser is used. Laser beam is much less divergent and makes the job of eliminating the false signal much easier. This method was suggested by O. J. Glenbocki.

2.2.2.2 A New Servo Mechanism

It should be emphasized here that the servo mechanism we discussed in ER is not very suitable for PR.

Let us first discuss why the servo mechanism used ER does not work well for PR. The output of the photodetector contains a dc part

$$V_{dc} = I_o(\lambda)R(\lambda)A(\lambda)K(\lambda) \tag{77}$$

and an ac output

$$V_{ac} = [I_o(\lambda)\Delta R(\lambda)A(\lambda)+V_{res}]*K(\lambda) \tag{78}$$

where $I_o(\lambda)$ is the incident light intensity, $A(\lambda)$ is the detector wavelength response (including filter response if it is used), V_{res} is the residual part of the spurious signal, which usually is independent of the probe beam wavelength. $K(\lambda)$ is the adjustable amplification controlled by the servo mechanism so that to keep V_{dc} constant. Let us take V_{dc} = unity , then

$$K(\lambda) = 1/I_o(\lambda)R(\lambda)A(\lambda) \tag{79}$$

The ac component to the lock-in amplifier is then:

$$V_{ac} = \Delta R(\lambda)/R(\lambda) + V_{res}/I_o(\lambda)R(\lambda)A(\lambda) \tag{80}$$

The first term $\Delta R/R$ is the normal PR signal. The second term is a false signal which is inversely proportional to the total response of the system (i. e. the structure at the lamp, the blaze of the monochromator and the wavelength dependence of the detector). This second term distorts the PR signal. Since this term involves structures dependent on the wavelength, it makes the interpretation more difficult than the unnormalized one. Showing in Figure 15 is a 300K PR spectrum from a multiple quantum well using the above servo mechanism. The specific structures labeled A to E are corresponding to the second term in the above equation. They are not real structures from the sample.

Because of the reason discussed above, most of the PR spectrum in the literature are unnormalized. Showing in Figure 16 is one of the unnormalized spectra. Compare to the proper normalized one (Figure 17), feature labeled D was greatly distorted. Any lineshape analysis based on this kind of spectra is unreliable. In order to fit experimental result to theory, normalized spectra is essentially important. An on line division does not solve this problem since it is based on the same mathematics formulation. One way to get normalized PR spectra is that first V_{ac} is measured than V_{dc} is record separately, finally divided V_{ac}-V_{res} by V_{dc}. The choice of V_{res} is quite critical and needs experience. Showing in Figure 18 is the spectra obtained by this way.

The best choice of V_{res} was made by reducing the false signal A, B, E to minimum.

We have de‥loped a new servo mechanism that dose not have the above problem (see Figure 14). A variable density filter (NDF) connected to a servo motor was placed in the optical path between the probe monochromator and the sample. The dc signal from the detector was used as input to the servo motor which varied the NDF to keep I_oR constant. The amplification factor $K(\lambda)$ is always constant and so is the residual signal $V_{res}K(\lambda)$. Thus it can be removed easily. Figure 17 shows the spectrum obtained by this new servo mechanism.

This normalization procedure has several considerable advantages over previously used methods [40] [61] [62]. It can be easily adopted to any kind of detector, such as Si, Ge photodiode, PbS detector or even PMT. The modern Si detector has better or almost the same noise to signal ratio compared to the more expensive PMT. However the linearity of Si detector is not as good as PMT. By keep I_oR constant, we can set the Si detector to the best biases condition and avoid any possible non-linearity or saturation. Since R does not vary much in the energy region of interesting, this servo mechanism essentially keeps I_o constant. There are more fundamental reasons to use this new servo mechanism i. e., this normalization procedure does not change operat-

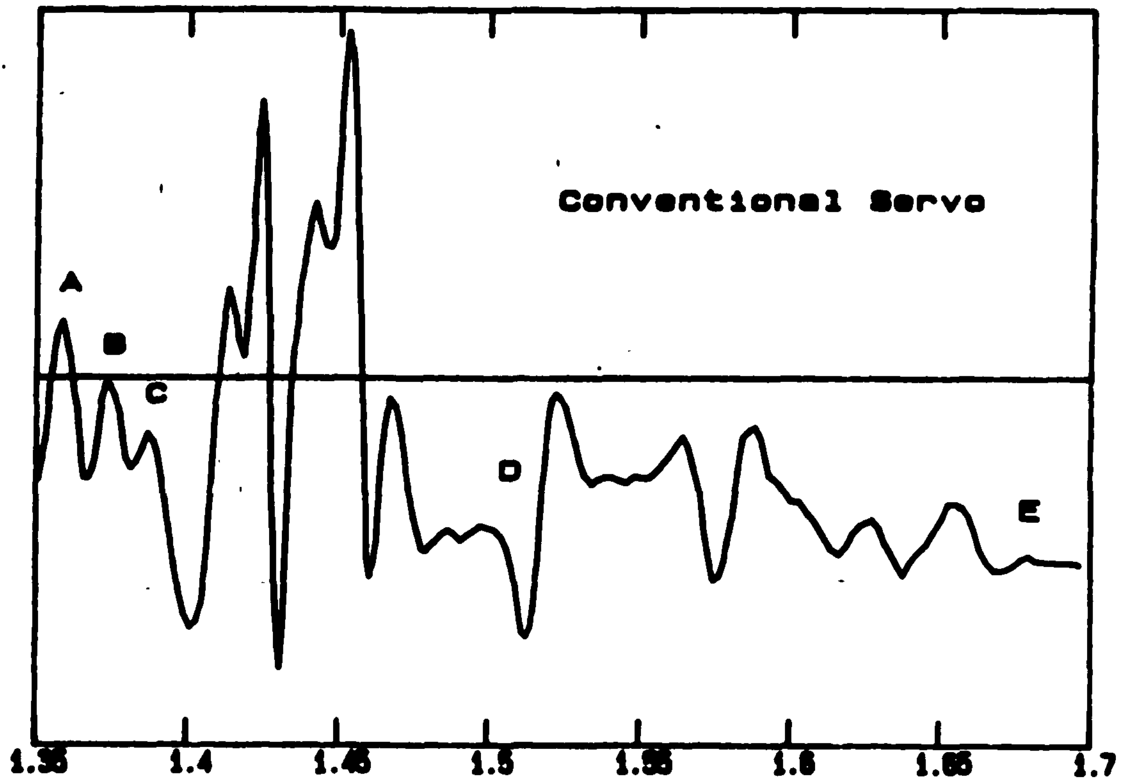

Figure 15: Photoreflectance spectrum from GaAs/GaAlAs quantum well normalized by conventional servo

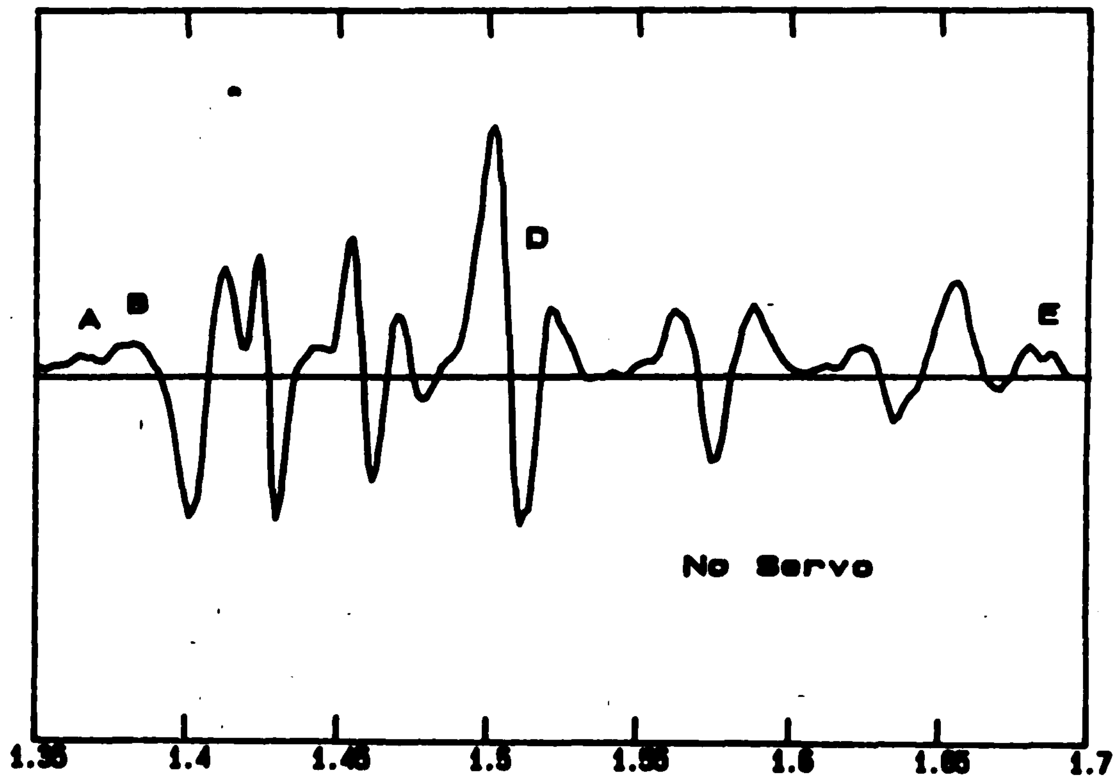

<u>Figure</u> <u>16</u>: Photorelectance spectrum from GaAs/GaAlAs quantum well unnormalized

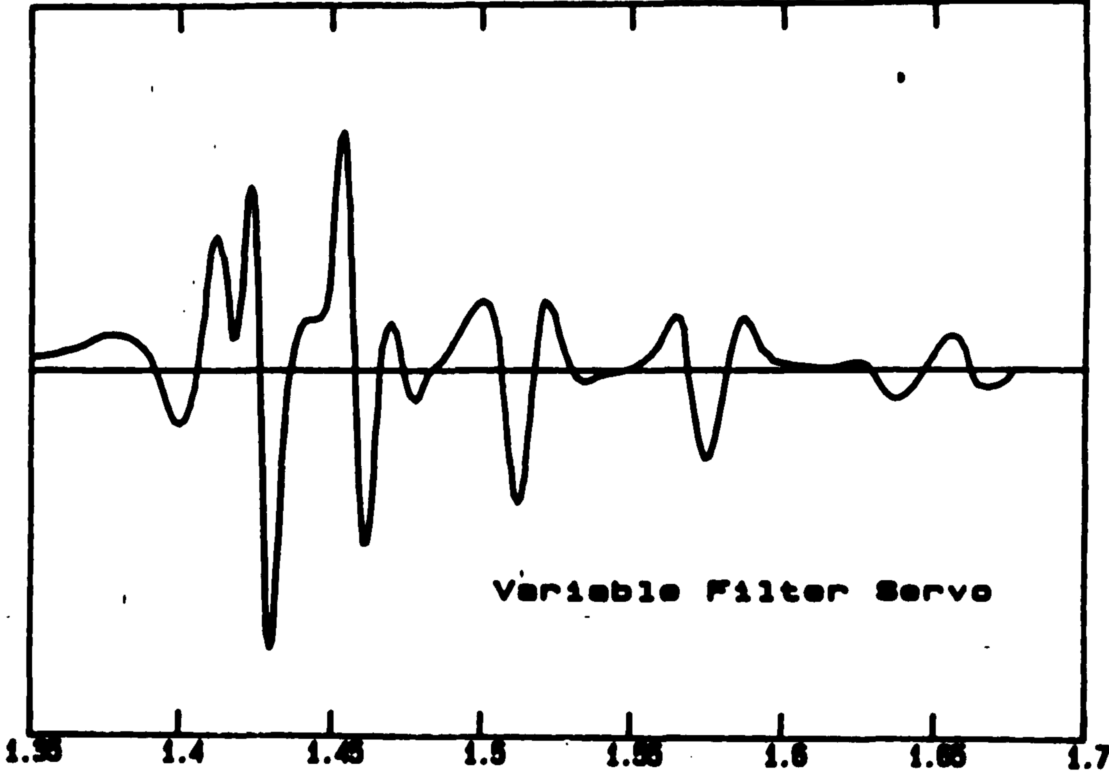

__Figure__ __17__: Photorelectance spectrum from GaAs/GaAlAs quantum well normalized by variable desity filter

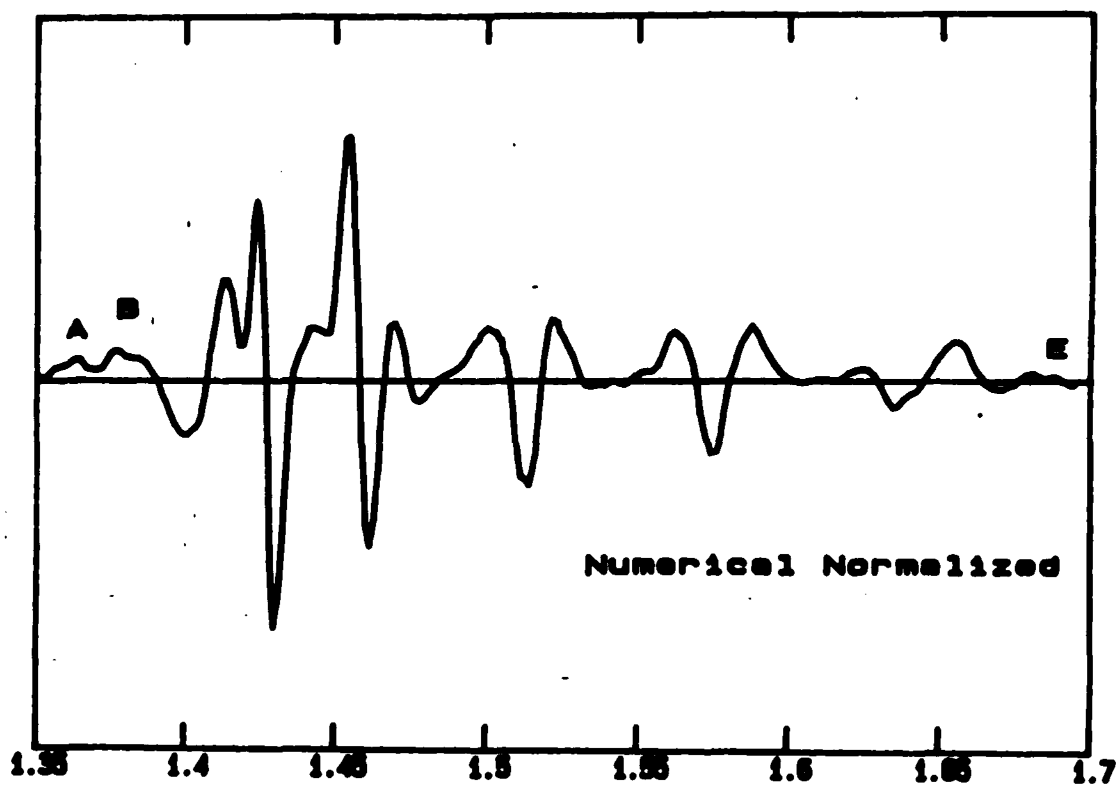

Figure 18: Photorelectance spectrum from GaAs/GaAlAS quantum well normalized by numerical division

ing condition of the system as well as the detector. Some of the physical system is very sensitive to the total light intensity (i.e. nipi structure or exciton features) . To avoid r self-modulation by the probe beam, keeping the probe beam intensity constant is intrinsically important.

2.2.2.3 Data Acquisition.

The whole system was controlled by an IBM PC/XT with IEEE interfacing. The program accomplishes following functions:

1. Automatic phase setting to maximum ac output.
2. Single or multiple scan in a preset pattern either equally spacing in the energy scale or putting emphasis on the region where same sharp feature appears thus making it possible to save running time without losing resolution.
3. For each step performs a servo cycle first, then wait a short period to let lock-in stable. This will eliminate quite a lot noise. We found that most of the noise in PR comes from the vibration of the monochromator grating induced by the step motor driving. (A proper choice of the chopping frequency to avoid resonant at the Fourier components of the step function is also important.)
4. Check lock-in status (i. e. overload or unlocking), collect data, plot on CRT and store in a floppy disk for latter analysis.

5. Interrupt routines enable users to pause , continue, discard some portion of the scan and set different scan pattern during the experiment

2.3 Experimental Results

2.3.1 Photoreflectance: GaAs/AlAs Superlattices

2.3.1.1 Fit to Electromodulation Theory

The lineshape of PR spectra in QW and SL is one of the fundamental questions in photoreflectance experiments. Is it first derivative or third derivative spectrum? We have shown in the section 2.1.2 that as long as electron and hole pairs can accelerate and gain energy from the electric field, the change of dielectric function is third derivative like(see Figure 19a). In QW ,however, electric field not only accelerates charged particles but also shifts the subband energy (so called quantized stark effect [63]). Thus energy gap modulation (first derivative) may also play a role in photoreflectance. This was first suggested by O. J. Glembocki[64]. They have fitted the low temperature PR spectra with the first derivative lineshape and compared the result to the photoluminescence spectra. The lineshape of $\delta\varepsilon/\delta E_g$ is shown in Figure 19b. However, the room temperature PR spectra of their group

[14] [65] and this experiment revealed a strong difference from the lineshape of $\delta\epsilon/\delta Eg$. In this section We demonstrate that the photoreflectance spectra of several GaAs/AlAs SLs can be fit by the Aspnes third-derivative functional form (TDFF) lineshape expression.

We have investigated PR from three <100> GaAs/AlAs SLs grown by Molecular Beam Epitaxy (MBE) with nominal quantum well/ barrier layer widths (W) of 113A (sample T0023), 85A (T0022) and 57A (T0019). These undoped SLs have a total thickness of about 1 micron and were grown on a 1 micron thick undoped GaAs buffer layer on top of a GaAs:Si ($1x10^{18}cm^{-3}$) substrate. The measurements were carried out at 300K and 77K using as the pump beam the 6328A line of a He-Ne laser.

Shown in Figure 20a and Figure 20b are the PR spectra (dotted line) from sample T0023 and 300K and 77K, respectively, using 6328A as the pump beam with a power density of several mW/cm^2. The solid line is a least square fit of the data to the Aspnes TDFF expression:

$$\Delta R/R = Re\{ \sum_{j=1}^{p} [C_j exp(i\theta_j)(E-E_{g,j}+i\Gamma_j)^{-m}]\} \qquad (81)$$

where p is the number of spectral features in the region to be fit, C_j, θ_j, $E_{g,j}$ and Γ_j are the amplitude, phase, energy and broadening

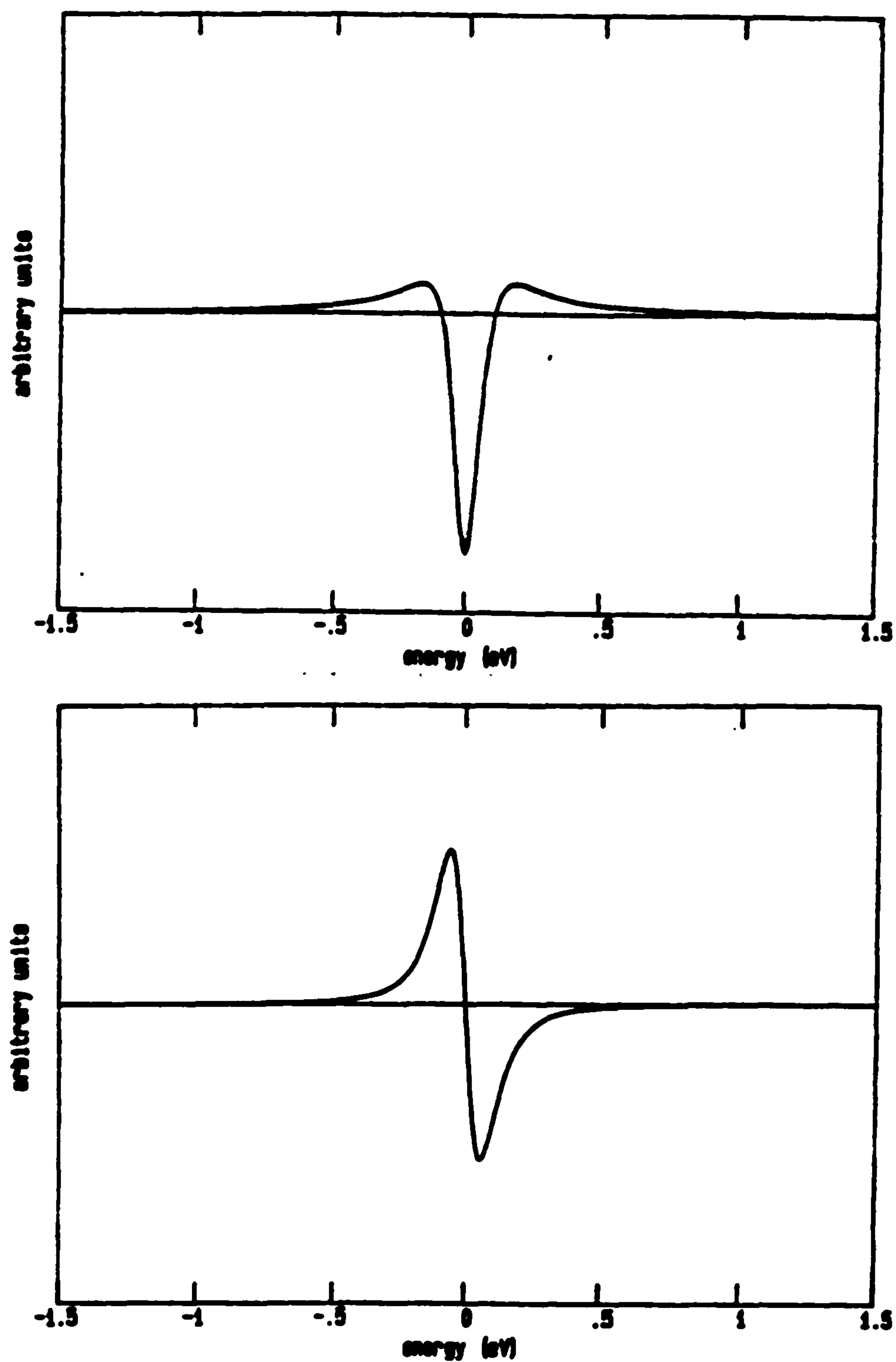

Figure 19: Comparison of third derivative and first derivative lineshapes. a)third derivative b) first derivative lineshape.

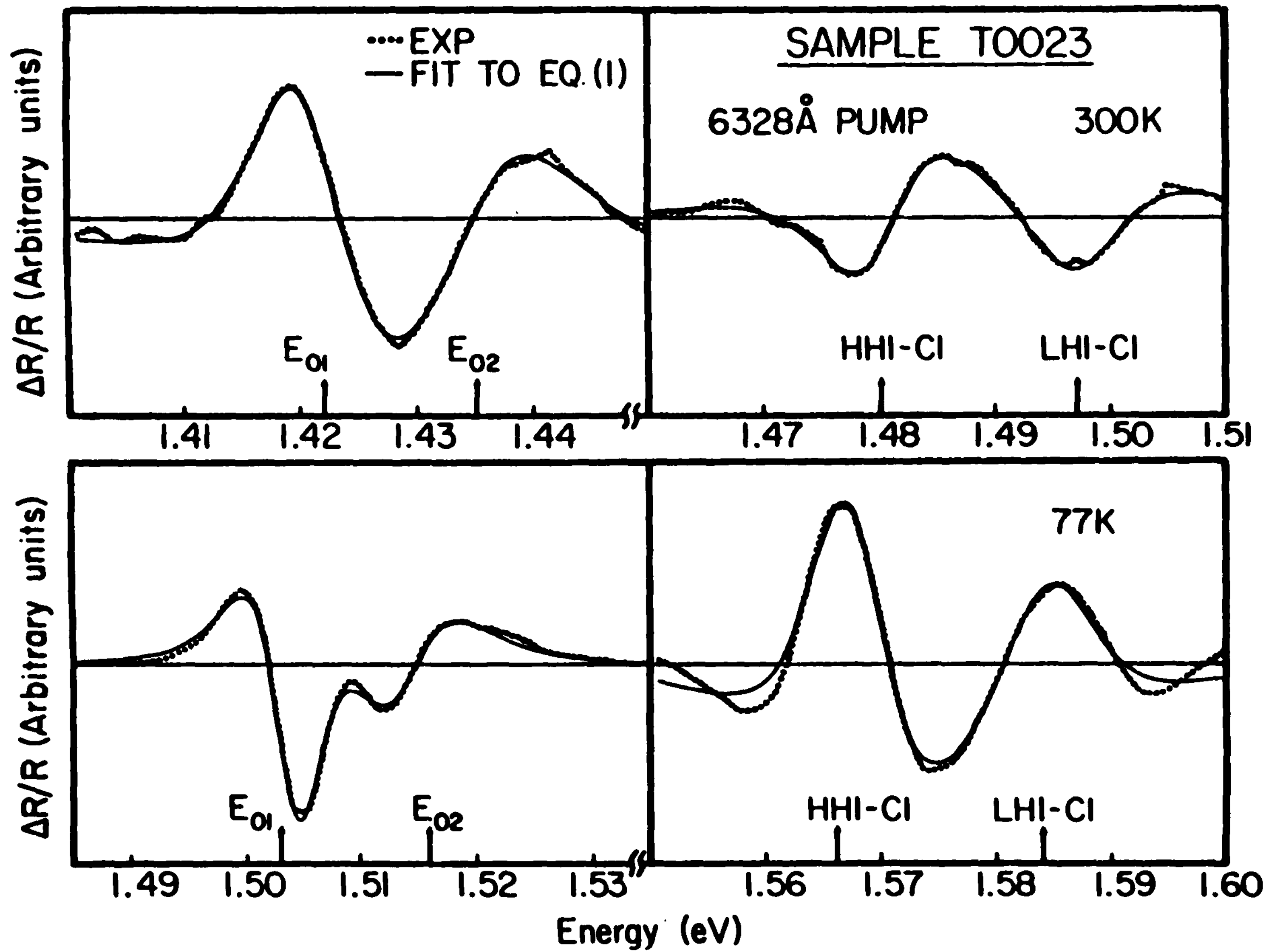

Figure 20: Photoreflectance spectra of GaAs/AlAs superlattices

parameter, respectively of the jth structure while m_j denotes the type of critical point. The measurement conditions were such that the lineshapes were independent of the intensity of the pumping beam, i. e. low field limit.

Table 1: Energies, broadening parameters from the buffer and the substrate of a GaAs/AlAs superlattice

Spectral feature	Temp (K)	Energy (eV)	Broadening parameter (meV)	Relative amplitude
E_{01}	300	1.422±0.0002	9±1	1
	77	1.503±0.0002	5±1	1
E_{02}	300	1.433±0.0002	11±1	0.29
	77	1.516±0.0002	10±1	0.42

The feature labelled E_{01} in Figure 20 corresponds to the direct band gap of GaAs. This feature appears to originate from the GaAs substrate [12] [14], even though it is about 2 microns from the surface. The second structure, denoted E_{02} is characteristic of the samples we

have studied and corresponds to the direct band gap of GaAlAs with $x \sim 0.02$ [66]. This peak originates in the "GaAs" buffer layer. It is due to the fact that during the growth of the "GaAs" portions of the sample (i.e. buffer layers and quantum wells) a small amount of Al has escaped around the shutter of the Al effusion cell. Thus, in our case the quantum wells are, strictly speaking, not GaAs but actually GaAlAs ($x \sim 0.02$). The energies, broadening parameters and amplitudes of E_{01} and E_{02}, obtained from the fit of TDFF using m=3.0, at 300°K and 77°K averaged over the three samples are listed in Table 1. The amplitude of E_{01} has arbitrarily been taken to be unity.

The doublet structure in the energy range 1.45-1.60 eV, labelled HH1-C1 and LH1-C1, are the n = 1 heavy-hole and light-hole to conduction state transitions, respectively. We did not see any other features from these superlattices. Note that the fit to TDFF is very good. This is the first fit of electromodulation spectra from superlattices or quantum wells to the Aspnes TDFF lineshape. Listed in Table 2 are the energies, broadening parameters (Γ) and amplitudes (the amplitude of HH1-C1 is taken to be unity) of HH1-C1 and LH1-C1 for all three samples as determined from TDFF for m=3.0. Also listed are the values of W from the growth conditions. In order to show that third derivative function does fit the experimental data best, we have also performed

Table 2: Comparison of experiment results and theoretical calculation of GaAs/AlAs superlattices

Sample	Spectral feature	Temp (K)	Energy (eV) experiment	Energy (eV) theory	Broadening parameter (meV)	relative amplitude
T0023	HH1-C1	300	1.480±0.0002	1.481	9.3±1	1
		77	1.568±0.0002	1.564	9.4±1	1
	HH1-C1	300	1.498±0.0002	1.502	8.4±1	0.52
		77	1.584±0.0002	1.585	10.0±1	0.52
T0022	HH1-C1	300	1.515±0.0002	1.511	11.4±1	1
		77	1.600±0.0002	1.594	10.4±1	1
	HH1-C1	300	1.544±0.0002	1.544	13.1±1	0.42
		77	1.628±0.0002	1.627	13.1±1	0.52
T0019	HH1-C1	300	1.629±0.0005	1.611	20.0±1	1
		77	1.698±0.0005	1.696	22.0±1	1
	HH1-C1	300	1.555±0.0005	1.679	45.0±1	0.67
		77	1.744±0.0005	1.763	26.0±1	0.67

least square fit of the data to Eq(81) for different m. The x^2 for different m is listed in Table 3. We have also let m in Eq(81) variable, the best fit was found to be for m=3.06.

We have performed theoretical calculations for the energies of these levels based on the Schulman-Chang model. using the parameters, i.e.,

Table 3: Comparison of fit with different order of derivatives

m	χ^2
1	18.6
2	6.2
3	2.32
3.06	2.30

effective masses and band offsets (Q) proposed by Miller et al.[67]. We have used parameters suggested by other workers[68] and find very little difference for the n=1 levels. For the energy gap of the quantum wells we have used the experimental value of E_{02} listed in Table 1. To obtain good agreement with experiment, values of W different from the growth condition had to be employed. The theoretical energy values and corresponding widths also are listed in Table 2.

In conclusion, PR from several GaAs/AlAs SL has been measured at 300K and 77K. We have demonstrated for the first time that electromodulation spectra from SL can be fit by the Aspnes TDFF lineshape thus enabling us to accurately determine energies, broadening parameters, phases and amplitudes.

2.3.1.2 Pump Wavelength Dependence (Depth Profiling)

In this section we report wavelength dependence of the PR on the same set of GaAs/AlAs superlattices (SL) mention in the previous section.

The measurements were carried out at 300K and 77K using as the pump beam light from a second monochromator with a Xenon arc source. Measurements were carried out in the range 9000A - 2700A. The pumping beam was chopped at about 100 Hz.

Plotted in Figure 21a, Figure 21b and Figure 21c are the PR spectra of sample T0023 at 300°K using pump wavelengths (from the second monochromator) of 7000A, 5000A and 3000A, respectively. Measurements have also been made at a series of wavelengths ranging from 7000 - 2700A. The pump power density was typically several microwatts/cm^2. The total pumping power was kept constant by means of a variable neutral density filter. (the same kind of filter as discussed in section 2.2.2.2, but adjusted manually.) The dotted line is the experimental data while the solid line is the least-squares fit to TDFF Eq(81). The obtained values of E_{01}, E_{02}, HH1-C1 and LH1-C1 are indicated. There is very little variation in these quantities as a function of pump wavelength (for 7000A the error bars on HH1-C1 and LH1-C1 are ±0.003 eV since the structure is weak). This indicates that the wells are quite uniform as a function of depth.

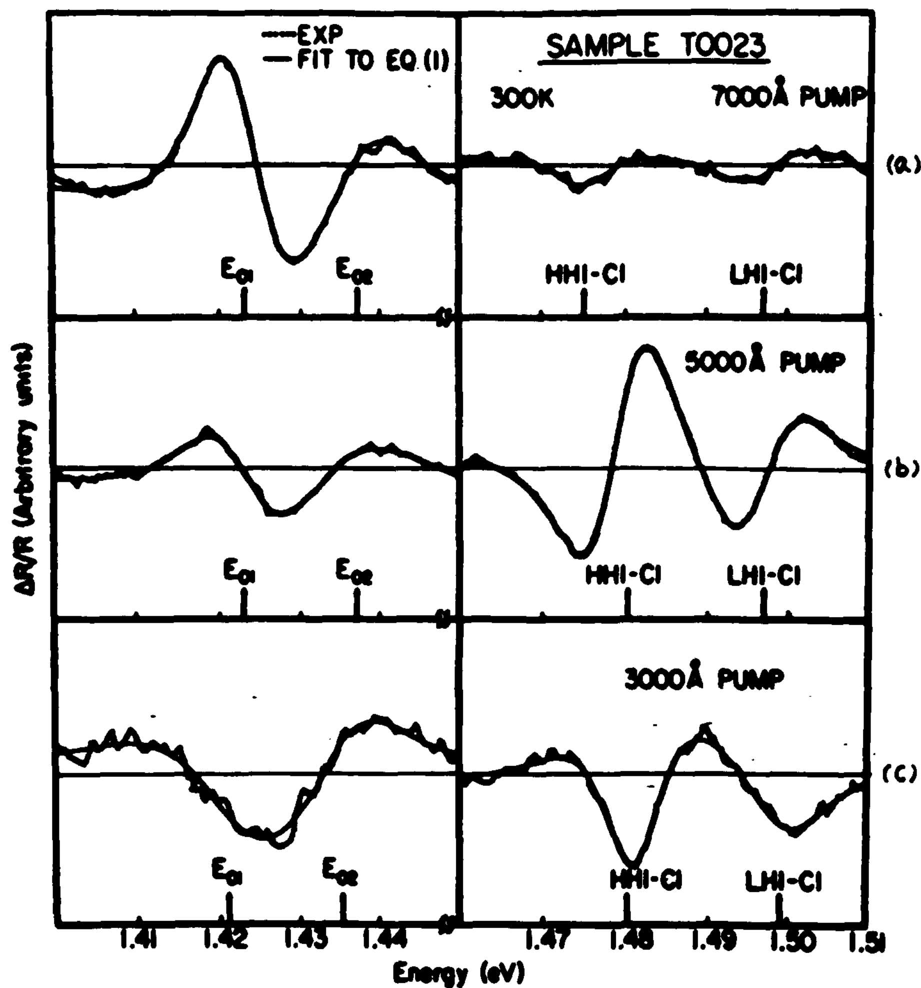

<u>Figure 21</u>: Wavelength dependence of the photoreflectance signal from GaAs/AlAs superlattices. pump wavelength a) 7000A, b) 5000A, c) 3000A. The dotted lines are the experimental data while the solid lines are the least square fit to TDFF. The energy of the various features are indicated by arrows.

Between 7000A-5000A, the signals from the QW, i. e. HH1-C1 and LH1-C1, increase but the signals from the buffer (E_{02}) and the substrate (E_{01}) decrease. This is due to the decrease in the penetration depth of the pump beam. Note that the ratio of HH1-C1/LH1/C1 remains constant, which shows that these two signals have the same wavelength dependence and they are coming from the same depth of the sample. However E_{01} decreases more rapidly than E_{02}, which shows the former one is coming from somewhere deeper in the material.

Between 5000A and 3000A there is a dramatic change in the spectrum, i.e. an inversion of the phases of E_{01}, HH1-C1 and LH1-C1 (but not E_{02}). In fact at about 4000A, which is the energy of the AlAs barrier layers [66], the entire PR signal is approximately zero. This is the first observation of a phase inversion in PR on a given sample and indicates that there is more than one mechanism responsible for the effect in superlattices, in contrast to bulk material.[69] These results suggest that the mechanism for modulation of the electric field is through light-induced charge injection, in which the nature of the field modulation (i. e. increasing or decreasing field) depends on whether the injection is below or above the wells.

It is also interesting that at pump wavelength 3000A, the features E_{02} and E_{01} can still be observed, even they are 1μm and 2μm from the

surface. In fact E_{02} even increases when the pumping photon energy is greater than the the energy gap of AlAs barrier layers. Note that the penetration depth of 3000A pump beam is only about 40^^\. This result indicates that the modulation at the buffer region is through the diffusing of photoinjected carriers. When the photoinjection is above the wells, carrier are more mobile and hence it is easier for them to reach the buffer layer. Thus the PR signal increases.

In conclusion we have studied the dependence of the PR signal on the pump wavelength from GaAs/AlAs superlattices. We have demonstrated that by using different pump wavelengths, it is possible a) to accentuate certain spectral features, (b) perform non-destructive depth profiling. The wavelength dependence of the PR has also revealed that there is more than one mechanism responsible for the PR effect in SLs, which depends on whether the injection is below or above the walls.

2.3.2 Photoreflectance: GaAlAs/GaAs Multiple Quantum Wells

2.3.2.1 Topographical Variations

In this section we report the use of room temperature PR to evaluate the topographical variations in barrier height (alloy composition) and quantum well thickness (W) across the surface of a GaAs/GaAlAs (x~0.24) multiple quantum well (MQW) sample with a spatial resolution of

about 100 microns [65]. Even at 300°K, it is possible to observe sharp structure from all n=5 confined quantum levels, as well as a signal related to the GaAlAs barrier layers [15]. The latter observation allows us to differentiate between the effects of barrier height and W on the energy of the quantum transitions. It is possible to valuate variations in barrier height to within several millivolts and W to within 2A. Since the penetration depth of the light is such that we are laterally sampling a number of quantum wells in this experiment, evaluations of barrier heights and W should be considered to represent averaged quantities. This method is contactless, (and hence non-destructive), can be employed conveniently at room temperature and the spectrum has a well-defined lineshape Eq(81). These latter two results gives this technique a significant advantage over other optical characterization methods such as photoluminescence (PL) and photoluminescence excitation spectroscopy (PLE) [67].

The MQW sample used in our experiment was grown by MBE at the Naval Research Laboratory. It consists of about 1 micron of alternating GaAs/GaAlAs layers on top of a GaAs substrate. From the growth conditions the nominal thicknesses of the quantum wells and barriers were 220A and 150A, respectively. The sample was mounted on an X-Y stage and the probe beam was focussed to a spot size of about 100 microns

using a high quality camera lens[70]. The pump beam, from a 1 mW He-Ne laser, was defocussed to cover an area somewhat larger than the region to be scanned. The pump beam power density wa~ only about 0.3 mW/cm^2. At this low power level the spectra were independent of power density. Photoreflectance data were taken on 16 spots in a square array on the sample covering an area of about 1 cm x 1 cm. The modulating frequency was 220 Hz.

Plotted in Figure 22 are four PR spectra across the diagonal of the sample in the energy range 1.4 -1.8 eV (dotted lines). We have identified the origin of the peaks by arrows at the top of the figure. The peak at about 1.42 eV corresponds to the direct gap of GaAs (E_{01}) and originates from the GaAs substrate. The features between 1.43 eV and 1.68 eV are the allowed ($\Delta n=0$) heavy hole to conduction ($h_1,\ldots h_5$) and light hole to conduction ($\ell_1,\ldots \ell_4$) transitions, [15] where the subscript indicates the quantum number. We do not observe the ℓ_5 transition. The spectral peak in the range 1.7 -1.8 eV labeled A is related to the direct gap of the GaAlAs barrier layer. The observation of this feature is an important aspect of electromodulation spectra since it enables the investigator to determine confinement energies.

The solid lines in Figure 22 are a least-squares fit of the experimental data to the Eq (81) for electromodulation spectra. Shown in

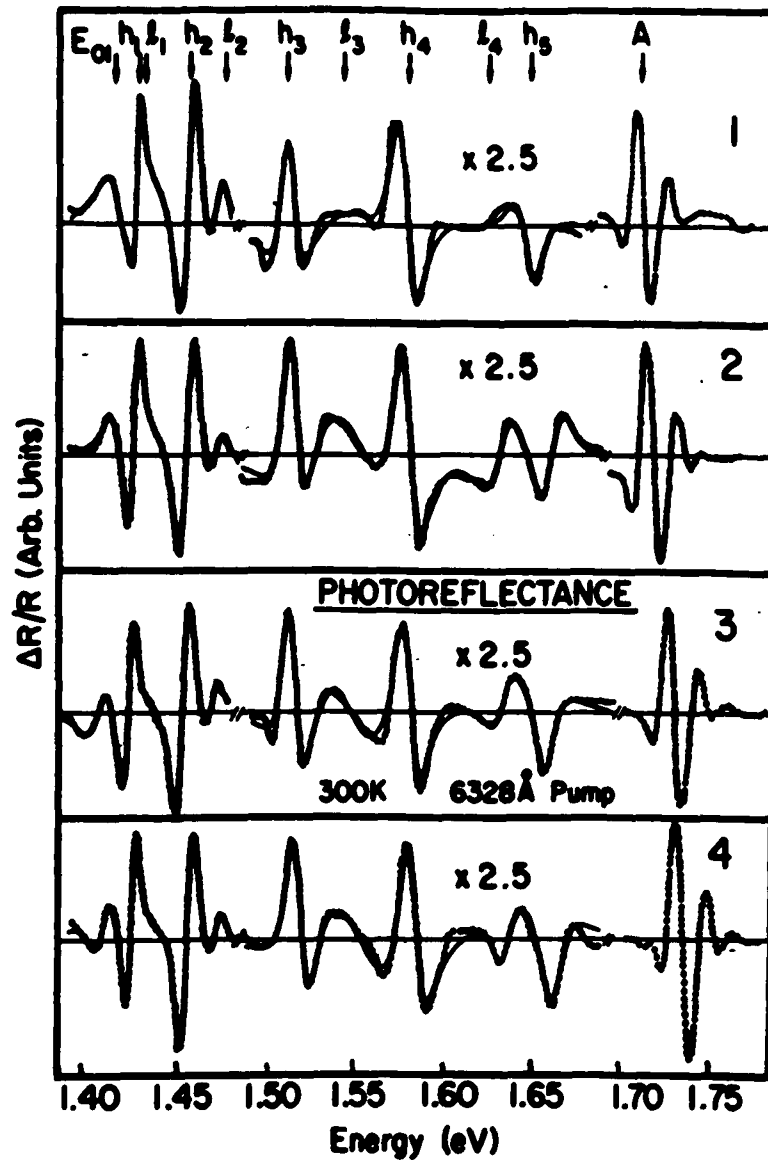

Figure 22: Photoreflectance spectra from GaAs/$Ga_{0.76}Al_{0.24}As$ multiple quantum well. dotted lines are the experimental results The solid lines are a least square fit to Eq(81).

Figure 23 is an expend version of Figure 22. Where the dotted line is then experimental data, then dashed line is a fit to the TDFF using only heavy hole transitions(h_1,h_2) whil~ the solid line includes the light hole transitions(l_1, l_2). The signal from the barrier layers appears to exhibit Franz-Keldysh oscillations and hence could not be fit by TDFF. However,it is still possible to obtain accurate values for A from a three-point fit to the spectrum [6]. Because of the quantum effects, the feature A occurs at an energy higher than GaAlAs barrier layers, the energy difference is a function of the well and the barrier parameter. In our case, the energy of A is 30meV above the GaAlAS barrier. From the relation $E_{02}(x) = E_o(GaAs) + 1.247x$, valid for $0< x <0.45$ [15], we can determine the value of the aluminum concentration to be about 24%.

Listed in Table 4 are the experimentally determined values of $E_{g,j}$ and Γ_j for the various quantum transitions as well as A at the four different spots on the sample across the body diagonal. Note that there is a systematic variation in the energy of the quantum transitions as well as A in going across the sample. We shall show below that the changes in $E_{g,j}$ are due to variations in W as well as barrier height. At all points E_{01} is found to be 1.415±0.002 eV with Γ= 6.7 meV. The values of Γ=6-7 meV for the h_1, ℓ_1 transitions is indicative of the high

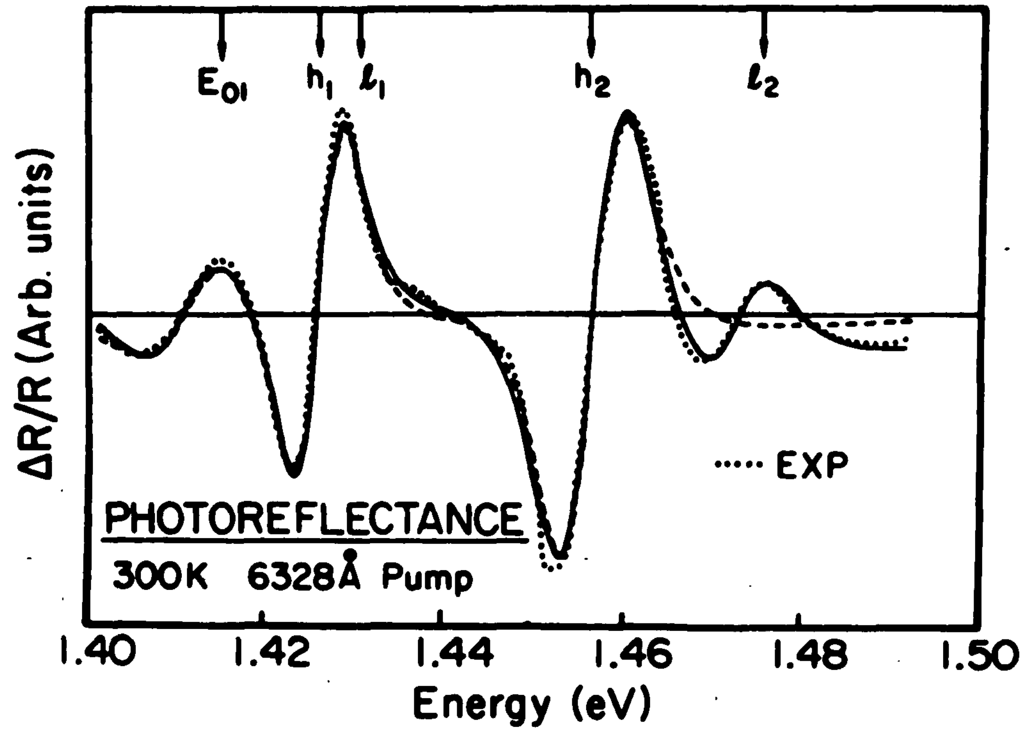

Figure 23: Expand version of photoreflectance spectra from $GaAs/Ga_{0.76}Al_{0.24}As$ multiple quantum well

quality of this material. Note that there is a systematic broadening of both the heavy and light hole transitions as a function of quantum number. Glembocki et al. have recently reported the temperature dependence of Γ for h_1 for a similar MQW [71].

Also listed in Table 4 are the theoretical values of the energies of the various quantum transitions (in parenthesis) using the model of Bastard (see section of 1.1.2), band offset(Q) parameters and well width W indicated in the table. The confinement energies for the electrons and holes are determined by Q and the experimentally measured E_{02}. The values of W listed in Table 4 are in good agreement with that deduced from growth conditions, i.e. 220A. We find that there is a variation not only in A but also in W in going from position A to D.

The need for a detailed lineshape fit also is clearly evident in determining variations in W, which are only about 2 monolayers in going from A to D. Plotted in Figure 24 is the experimental data (dotted lines) for the h_3, ℓ_3, h_4, ℓ_4 and h_5 quantum transitions for position D. This spectra has first been fit by using TDFF (solid line) and values of $E_{g,j}$, Γ_j, θ_j have been evaluated. The best agreement between the experimental and theoretical values of $E_{g,j}{}^{th}$ is obtained using W=210A (see Table 4). In order to evaluate the effects of a change in W the following procedure has been used. We first calculate $E_{g,j}{}^{th}$ for

Table 4: Energy and broadening parameters for various quantum transition at four position alone the body diagnal

Also listed are the energy value of the feature A and its broadening parameters. In parentheses are the theoretical value of the MQW transitionsusing (A-30meV) as the barrier height, and the widths W indicated at the bottom of the table.

	position 1		position 2		position 3		position 4	
	E (meV)	Γ	E (meV)	Γ	E (meV)	Γ	E (meV)	Γ
H1	1426±1 (1426)	5.8±1	1426±1 (1426)	6.5±1	1426± 1 (1426)	6.9±1	1426±1 (1426)	6.4±1
L1	1430±5 (1430)	5.6±2	1430±5 (1430)	6.3±2	1429± 5 (1430)	6.3±2	1431±5 (1430)	6.4±2
H2	1455±2 (1458)	9.1±1	1456±2 (1459)	9.1±1	1456±2 (1459)	9.1±1	1456±2 (1460)	9.1±1
L2	1474±5 (1473)	12.0±3	1475±5 (1473)	12.4±3	1473±5 (1474)	10.7±3	1475±5 (1475)	9.3±3
H3	1506±3 (1508)	10.6±2	1510±3 (1510)	11.4±2	1511±3 (1511)	10.3±2	1515±3 (1512)	11.7±2
L3	1537±5 (1540)	49±5	1540±5 (1542)	42±5	1541±5 (1543)	25±5	1544±5 (1546)	35±5
H4	1572±3 (1573)	12.6±3	1574±3 (1576)	13.5±3	1577±3 (1578)	12.2±3	1580±3 (1581)	13.1±3
L4	1618±5 (1620)	39±5	1626±5 (1625)	42±5	1628±5 (1626)	25±5	1633±5 (1632)	35±5
H5	1641±5 (1643)	13.7±4	1655±5 (1648)	15.6±4	1653±5 (1650)	15.2±4	1658±5 (1656)	16.8±4
A	1706±1	6.9±1	1714±1	7.1±1	1723±1	7.1±1	1732±1	6.1±1
w	214A		211A		211A		210A	

W=208A and 212A. Using the experimentally determined values of Γ_j, θ_j and C_j (as well as A) but quantum transition energies equal to $E_{g,j}(W)=E_{g,j}^{exp} \pm [E_{g,j}^{th}(W) - E_{g,j}^{th}(210A)]$ we employ TDFF function to generate the spectra for the 212A (dashed line) and 208A (dot-dashed line) cases shown in the figure. It is clear that variations corresponding to changes in W of about 2A can be determined. We would like to emphasize the fact that even though the relation between W and $E_{g,j}$ is somewhat model and parameter dependent (i.e values of masses and Q [67] [72]) the variations in $E_{g,j}$ with W is relatively independent of model parameters used.

In the analysis discussed in the sections we have considered only allowed transitions in fitting the data to TDFF function). The addition of forbidden features would probably further improve the fit. For example there is a forbidden transition (HH2-C1) at about 1.44 eV which would make the agreement between experiment and fit even better in this region (see Figure 23) The addition of such weak forbidden features is expected to have very little effect on the parameters of the allowed transitions. In the next section we will discuss forbidden transitions.

In conclusion, we have used room temperature PR to investigate the topographical variations in barrier height (and hence confinement ener-

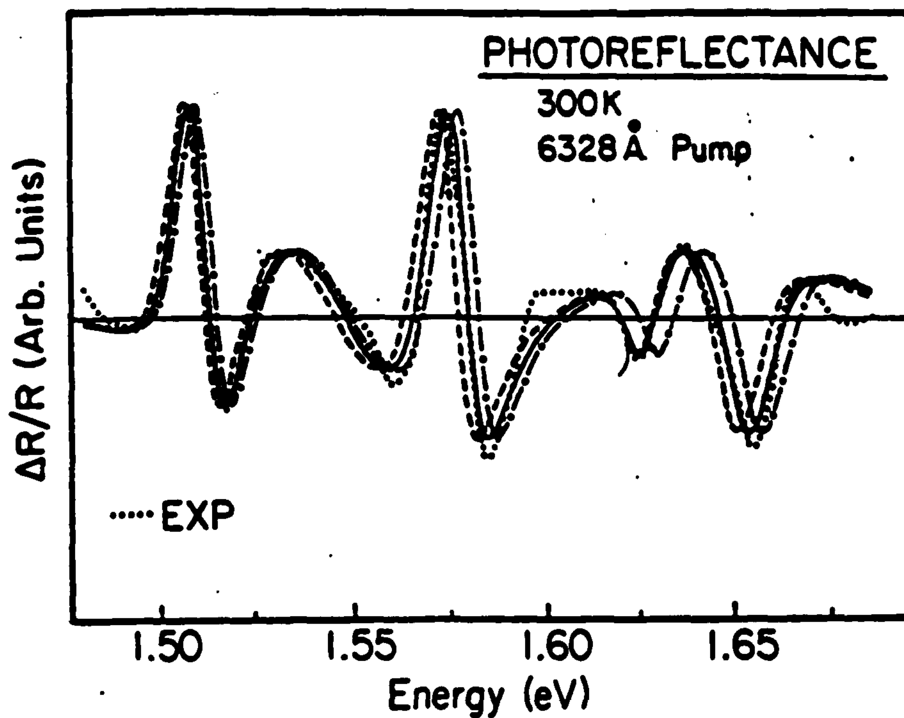

<u>Figure</u> <u>24</u>: Photoreflectance spectra from $Ga_{0.76}Al_{0.24}As/GaAs$ multiple quantum well. dotted line Experimental data. solid line lest square fit to the experimental data. dashed(208A) and(212A) TDFF generated spectrum.

gy) and quantum well width W with a spatial resolution of about 100

microns in a GaAs/GaAlAs MQW. The spectra exhibits features from all confined quantum levels as well as from the GaAlAs barrier layers. This latter feat··~e makes it possible to differentiate the effect of changes in barrier height and W on the quantum levels. By employing a detailed lineshape fit (Aspnes third-derivative functional form) variations in W as small as one monolayer can clearly be detected.

2.3.2.2 Forbidden Transitions

In this section we report a room temperature PR study of a GaAs/GaAlAs multiple quantum well (MQW) in which, for the first time, forbidden transitions have been clearly observed at 300K. We have detected three symmetry forbidden features from the MQW in addition to all the allowed quantum transitions. Also, there are features in the spectra which may be due to transitions involving unconfined states [30]. Glembocki et al. have recently reported the temperature dependence of PR in GaAs/$Ga_{1-x}Al_xAs$ multiple quantum wells [71]. Although they clearly observe forbidden features at low temperatures (149K and 125K) their room temperature spectra reveals only two very weak structures which correspond to the forbidden transitions.

The sample used in this study was a 100A/150A GaAs/$Ga_{1-x}Al_xAs$ MQW ($x \sim 0.17$) grown by molecular beam epitaxy at the Hughes Research Laboratory. All measurements were made in the "low-field" limit, i.e., the lineshape was independent of pump power density.

Shown by the dotted line of Figure 25 is the experimental PR spectra. The solid line in Figure 25 shows a least-squares fit of Eq(81) to the experimental data originating from the MQW (we have not fit E_{01} and will return to this point later) for p = 10 (i.e., ten spectral features). The energies of the various features are given by arrows at the top of the figure. The E_{01} structure at 1.415±0.002 eV corresponds to the lowest direct band of GaAs and originates from the GaAs substrate. Similar observations of E_{01} have been reported by other authors [12] [15] [74] on superlattice or quantum well systems.

The structure B is related to the direct band gap of the GaAlAs barrier layers. However, because of quantum effects it occurs at a somewhat higher energy, the energy difference being a function of the well and barrier parameters. The observation of this feature in electromodulation[13] [15][74] is important since it is an indirect measure of the barrier height. The notation nmH or nmL for several of the peaks represents transitions between the nth conduction subband and the mth valence subband of heavy hole (H) or light hole (L) character. Allowed transitions have m=n while for symmetry forbidden transitions m≠n. The features A,B and C will be discussed in more detail below. The energies and broadening parameters of the various features from the MQW are listed in Table 5 We find that the E_{01} structure could not

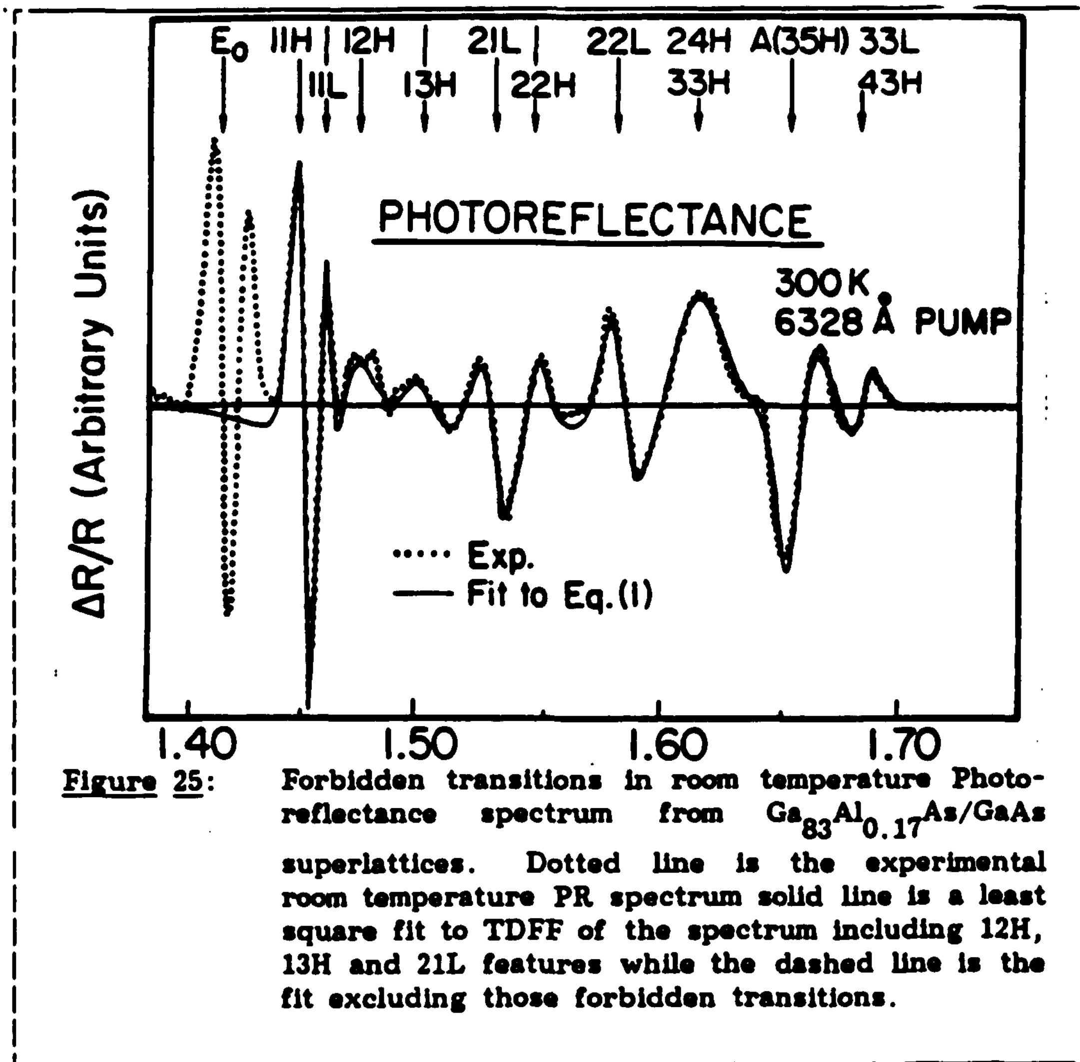

Figure 25: Forbidden transitions in room temperature Photoreflectance spectrum from $Ga_{83}Al_{0.17}As/GaAs$ superlattices. Dotted line is the experimental room temperature PR spectrum solid line is a least square fit to TDFF of the spectrum including 12H, 13H and 21L features while the dashed line is the fit excluding those forbidden transitions.

be fit to TDFF, since it apparently exhibits Franz-Keldysh oscillations. However, an accurate value for the energy of E_{01} can be obtained from a three-point fit [6].

In order to demonstrate that the forbidden features 12H, 13H and 21L are indeed real we have attempted a fit to the experimental data by excluding these transitions (i.e., p=8). This is shown by the dashed line in Figure 25. The fit which includes the forbidden transitions (solid line) is clearly better than the dashed line, particularly for the resolved peaks for 12H and 13H. By adding 21L, which is not clearly resolved from 22H, we have substantially improved the fit to the amplitude in the region of the allowed features 22H and 22L. This result demonstrates that there are features at the positions of these three forbidden transitions.

In order to verify the origins of the structures from the quantum wells in Figure 25, we have performed a calculation based on the two-band tight-binding model [75]. We have employed the energy of E_{01} for the energy gap of the quantum well layers. The structure B cannot be interpreted as the energy gap of the barrier layers, however. calculations show that the barrier gap is not directly observable as an optical transition. The quantum effect due to the finite layer widths raises the energy of the lowest allowed transition above the barrier transition to slightly higher than the barrier band gap. We find the 35H transition is the first unconfined to unconfined feature. The tight-binding model indicates it should be strong and easily observable.

A good fit is achieved for the various transitions (including B) using a barrier height of 1.634 eV (x~0.17) and a well width (W) of 99.1 A (35 layers of 2.83A per layer). This value of W is in good agreement with the growth conditions. The various theoretical energies corresponding transitions also are listed in Table 5. For several of the transitions we give a range of energies due to the dispersion along the direction of the minizone corresponding to the growth axis.

As can be seen from Table 5, there is very good agreement between the experimentally determined energies of the various quantum transitions and the theoretical values, thus verifying the origins of the different allowed and forbidden features. The forbidden features 12H, 13H and 21L have recently been reported in the low temperature photoluminescence excitation spectra [76] of quantum wells GaAs/GaAlAs (x~0.30)quantum wells having dimensions similar to our sample. With respect to broadening parameters Ref [30] finds the relation $\Gamma = C_o hm$ meV, C_o being an adjustable parameter equal to the linewidth of the 11L transitions. As can be seen from Table 5 our room temperature broadening parameters do not follow this relationship. The relative intensities of our observed transitions (except for A,B and C) appear to be in good agreement with those of [30]. For example, we also find 21L and 22H to have about the same magnitude.

Table 5: Comparison of experiment results and theoretical calculation of GaAs/$Ga_{0.83}Al_{0.17}As$ superlattices including forbidden transitions

Experimental values of the energies, broadening parameters for the various transition from a fit of Eq(81) to the experimental data. Also listed are theoretical values for the various transitions.

	Experiment		Theory	
Spectral features	Energy (eV)	Γ (meV)	Energy (eV)	Transition
11H	1.448±0.002	8±1	1.449	11H
11L	1.456±0.002	7±2	1.461	11L
12H	1.470±0.010	25±5	1.471	12H
13H	1.498±0.005	19±5	1.503	13L
21H	1.529±0.005	10±2	1.531	21H
22H	1.545±0.005	10±2	1.541	22H
22L	1.580±0.003	13±2	1.581	22L
A	1.614±0.005	30±5	1.602	24H
			1.618-1.632	33H
B	1.653±0.003	13±2	1.650-1.670	35H
C	1.682±0.003	11±2	1.654-1.680	33L
			1.678-1.640	43H

The origins of the A and C features are not clear at this point. The former could be due to either the forbidden 24H transition (1.598-1.595 eV from Table 5) or possibly the 33H transition (1.610-1.624 eV). This latter transition is from a confined hole state to

an unconfined conduction level. The C peak at 1.682 eV could be attributed to a 33L transition (both states being unbound), a 43H transition, or possibly a Franz-Keldysh oscillation of the B feature. These spectral features are under further investigation.

In conclusion we have investigated the room temperature PR spectra of a GaAs/GaAlAs superlattice. In addition to the allowed transitions we have clearly observed, for the first time at room temperature, three features corresponding to forbidden transitions. The fit to the Aspnes TDFF has allowed us to accurately determine the energies and broadening parameters for all the transitions. For the energies there is very good agreement between experiment and theory based on a two band tight-binding model. There are three features which may be related to transition involving unconfined states.

2.3.3 Electroreflectance: InP/ITO Space Charge Region

In this section we present a study of the ER spectra of the indium-tin oxide InP (ITO/InP) system in the vicinity of the direct gap (E_o) of InP as a function of the applied dc bias voltage (V_{dc}) and ac modulation voltage(V_{ac}). The samples studied were <100> p-InP (Zn-doped) with a nominal acceptor concentration (N_a-N_d) of (1.3-1.7 x10^{16}cm^{-3}. The surfaces were prepared by polishing with 1 μm diamond paste and then by 0.3 μm and 0.05 μm alumina polishing powder, respectively.

This was followed by a chemo-mechanical polish in 0.05% Br_2/Methanol and a rinse in NH_4OH. The ITO was deposited to a thickness of about 650A by ion-beam sputtering. The deposited ITO had a carrier concentration of about 10^{21} cm^{-3}.

Experiments were carried out at room temperature with dc voltage ranging from 0-15V (reverse dc bias) and ac modulation voltage ranging from 0.1-12V. The modulating ac voltage was a bipolar square wave at 120 Hz. At positive half cycle, the total applied voltage is $V_{dc}+V_{ac}$ While at the negative half cycle it is $V_{dc}-V_{ac}$. The whole system was operated at almost open circuit condition. The maximum current was found not exceed 1mA. And also the photovoltage induced by the probe beam was found to be small.

Shown in Figure 26 are the ER spectra the energy region of the direct band gap of InP for various dc bias voltages (reverse bias) but fixed ac modulation voltage (V_{ac}=0.1V). The features denoted A,B and C are due to excitonic effects in a portion of the SCR where the electric fields are low enough not to quench the exciton. Similar phenomenon have been reported for electrolyte electroreflectance in GaAs[77] and have been discussed further by Kiselev[78]. These features can be used to gain information about the SCR but will not be the main focus of this experiment.

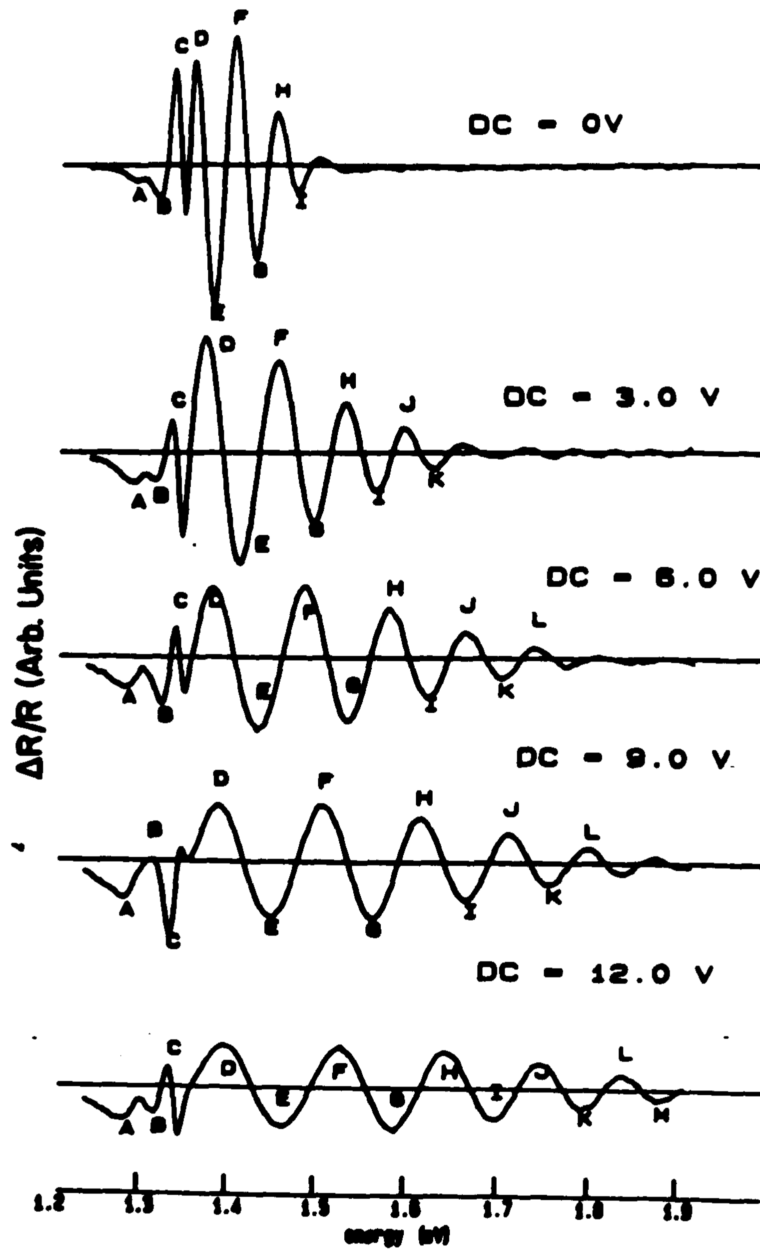

Figure 26: Electroreflectance of InP/ITO at various dc bias

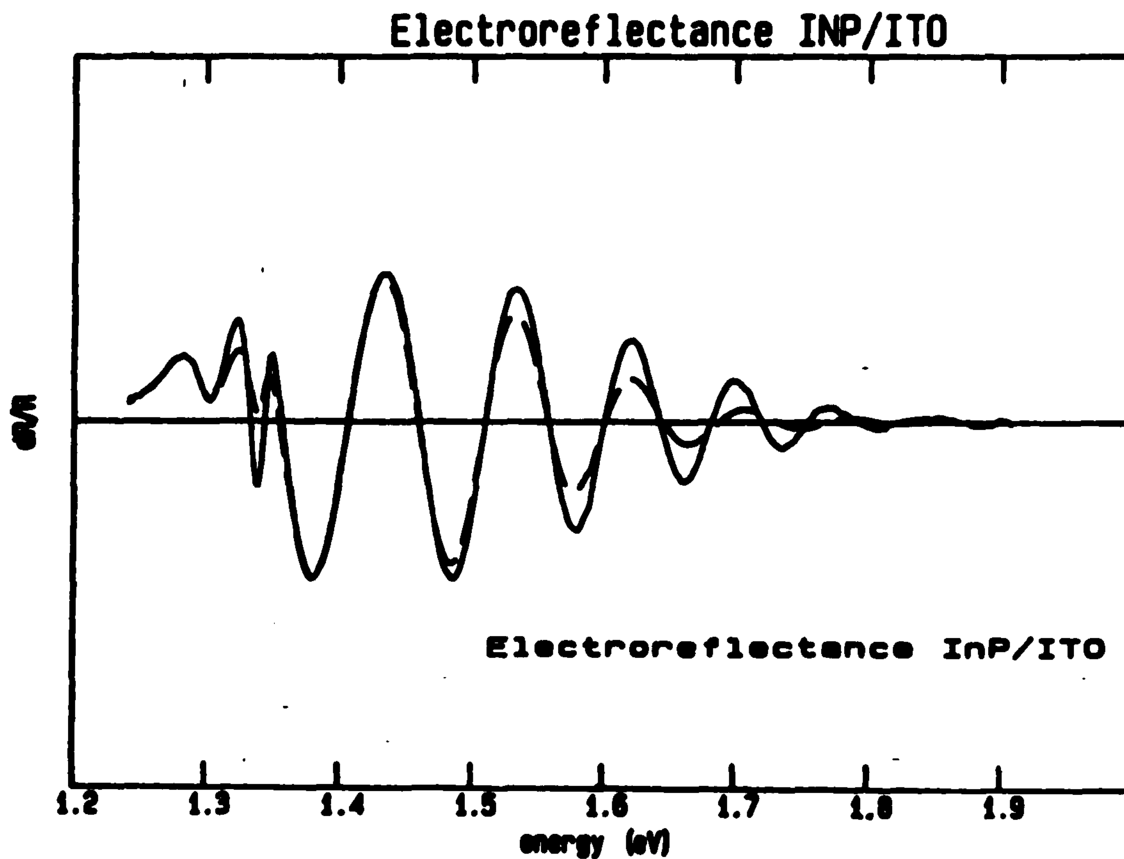

Figure 27: Electroreflectance of InP/ITO at various ac modulation voltage. The solid line is V_{ac}=0.1V, the dashed line V_{ac}=1.5V. All lines are at V_{dc}=6V.

The peaks D,E,F,G,H and I at zero bias are FKO originating in the SCR. However, as we have demonstrated in the section 2.1.4 that these FKO are significantly different than those report~~d in previous experimental and theoretical studies [6][79]. As the reverse dc bias is applied to the sample, the energy spacing between the FKO increases, indicating an increase in the electric field in the SCR. Also note that the high order FKOs become clearer and clearer when the dc bias increases.

Shown in Figure 27 are the ER spectra from the same sample. with fixed dc bias but various ac modulation voltage. The solid line is V_{ac}=0.1V, and the dashed line V_{ac}=1.5V. The spacing between the FKO is almost independent of the ac voltage. However, as the ac voltage increased, the high order FKO oscillation decreased rapidly, indicate an increase in the inhomogenity of the modulation field.

The above result is in good agreement with the generlized FK theory developed in section 2.1.4.

2.3.4 Photoreflectance: InP/ITO Space Charge Region

In this section we present a study of the PR spectra of the indium-tin oxide InP (ITO/InP) system in the vicinity of the direct gap (E_o) of InP as a function of the applied dc bias voltage (V_{bias}). From the observed Franz-Keldysh oscillations. we can quantitatively evaluate the

dc surface electric field ($\mathcal{E}_s$) as a function of V_{bias}. This allows us to obtain, in essence, an optical Mott-Schottky plot from which we can determine the build-in potential (V_{bi}) as well as the net carrier concentration. The samples studied were the same as we discussed in the last section. Two samples were investigated: one consisted of unannealed InP and a second in which the InP had been annealed at 450°C in forming gas before the ITO was applied.

Shown in Figure 28 are the PR spectra for the unannealed ITO/InP sample in the energy region of the direct band gap of InP for various dc bias voltages (reverse bias). The notations A-J are the same as we used in Figure 26. Note that the lineshapes of Figure 28 and Figure 26 were almost identical, which indicate that the electromodulation is the dominant mechanisms for photoreflectance. Also note that in the spectrum with V_{dc}=11.5V, the high order FKO up to 1.75V was quite clear, which indicated that the photoreflectance gave rise a more uniform modulation than electroreflectance. According to the GFKO theory this result suggested that potoinjected carriers only created a very small modulation. Compare Figure 28 to Figure 27 we concluded that the photoinjected modulation is less than 0.1V.

As we mentioned in section 2.1.3 the electric field in the SCR can be obtained from the slope of $(E_n-E_o)^{3/2}$ as function of index number

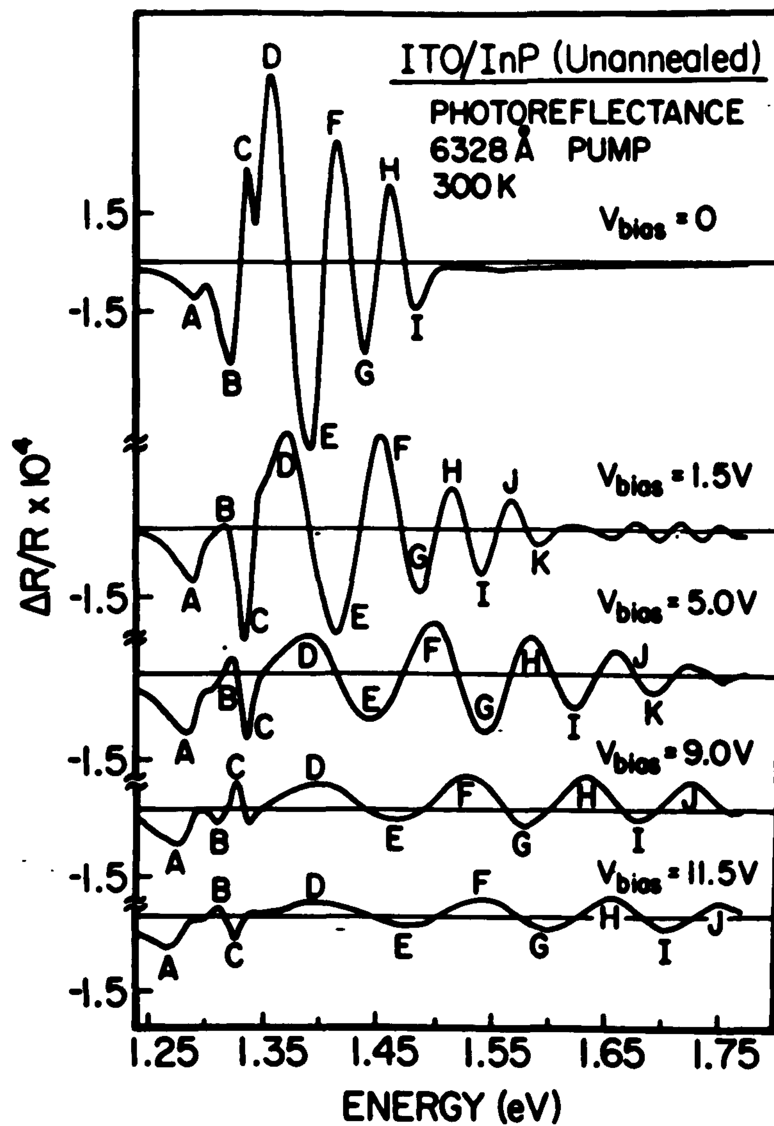

Figure 28: Photoreflectance spectra of InP/ITO at various dc bias.

n. For example, in Figure 28 feature D corresponds to n=1, feature E has n=2, etc. We find that such plots are indeed linear, thus enabling us to evaluate $\mathcal{E}$ as a function of V_{bias}.

In a fully depleted p-type SCR the surface electric field and potential are related by

$$\mathcal{E}_s^2=2[e(N_a-N_d)/k\varepsilon_o](V_{bi}+V_{bias}) \tag{82}$$

where N_a-N_d is the net impurity concentration, ε_o is the permittivity of free space, κ is the dc dielectric constant of the material (14.2 for InP) and V_{bi} is the built-in potential.

Plotted in Figure 29 is $\mathcal{E}_s^2$(dc) as a function of V_{bias} for both unannealed (open circles) and annealed (closed circles) samples, where $\mathcal{E}_s^2$(dc) has been evaluated from the period of the FKO. The solid lines are least-square fits to the experimental points. We have taken $m^*=0.073\ m_o$, where m_o is the free-electron mass. This value of m^* assumes that the PR spectra is due predominantly to transitions from the heavy-hole band to conduction band[80] [81]. The light-hole to conduction transitions should be a factor of three weaker due to matrix element effects.

As can be seen from Figure 29 $\mathcal{E}_s^2$ is linear in V_{bias}, thus enabling us to determine V_{bi} and N_a-N_d. We find that for the unann-

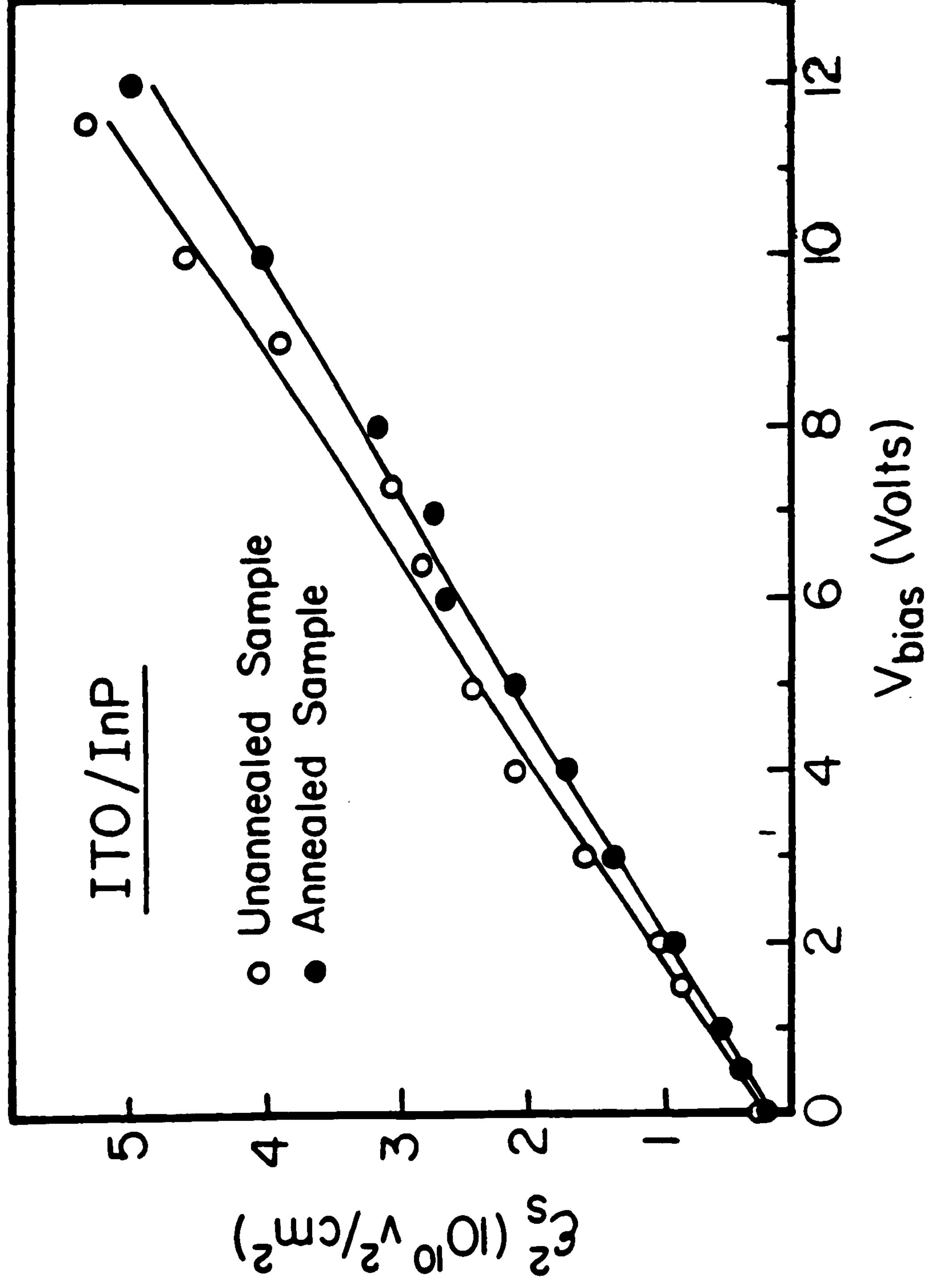

Figure 29: Surface filed as a function of bias voltage

ealed sample V_{bi}=-0.45±0.1 V and N_a-N_d=(1.55±0.1)x$10^{16}$$cm^{-3}$ while for the annealed sample V_{bi}=-0.35±0.1 V and N_a-N_d =(1.45±0.1)x10^{16} cm^{-3} The d‘‘ferences in V_{bi} and N_a-N_d are just outside the experimental error and may represent a real effect. This will be the subject of a future study. These values of N_a-N_d are in good agreement with those quoted above which were obtained from Hall effect measurements on similar material. The values of V_{bi} measured in this experiment are somewhat smaller than those deduced from prior studies on InP, which has Fermi level pinning states at 1.2 eV and 0.9 eV above the valence band. Thus, the surface preparation and ITO treatment of our samples has served to lower the built-in potential of the InP. The annealing may also have an effect.

Let us now return to the exciton features A-C. The sensitivity of these structures to V_{bias} arises from a surface interference effect. In the SCR there is a spatial variation in the dielectric constant due to the exciton oscillator strength for a particular photon energy. Over most of the SCR absorption due to the excitons is negligible because the dc electric field (which varies linearly with distance from the surface) exceeds that necessary to ionize the exciton (of order several kV/cm). However, near the "boundary" between the SCR and the bulk, the field is low enough for excitons to become stable and thus interact with the

light. Thus an interference effect occurs between the light reflected from the ITO/InP interface and the light reflected from the region of the SCR where the exciton is not quenched. As V_{bias} is changed the width of the SCR also varies thus giving rise to an interference pattern in the electromodulation spectra for photon energies somewhat below E_o. Note that there is a change of phase of the exciton feature between 0 V and 1.5 V bias, between 5.0 V and 9.0 V bias and again between 9.0 V and 11.5 V.

In conclusion we have investigated the photoreflectance spectra from the SCR in the model system ITO/InP as a function of V_{bias}. In addition to exciton interference effects we observe FKO which are functions of V_{bias}. By plotting $\mathcal{E}_s^2$ as a function of V_{bias} we can obtain V_{bi} and the net carrier concentration. This technique is essentially an optical Mott-Schottky method and can be used on other semiconductors. It would be possible to obtain topographical scans of the electric field and carrier concentration distributions in actual device configurations by focussing the probe beam down to a small spot size (about 100 µm has been achieved [65]). It should also be pointed out that since PR is a contactless technique measurements of $\mathcal{E}_s$ could be performed on the bare semiconductor surface (although, of course a bias dependence study could not be performed under these conditions).

2.3.5 Photoreflectance: GaAs Doping Superlattices

Semiconductors with a periodic profile of n- and p-doped layers, possibly separated by undoped (intrinsic, i) regions (n-i-p-i superstructures), exhibit interesting properties not found in either bulk crystals or compositional superlattices [24] [35]. These nipi structures have an "indirect gap" in real-space, long electron-hole recombination lifetime because of the spatial separation of the carriers, and a two-dimensional subband structure for the electrons and holes that can tailored independently for each carrier type. Even though there have been considerable optical studies on these semiconductor structures, most of the investigations have deal with the near band gap and below band gap regions [24] [35] [36]. Recently, work on the above band gap optical properties has also been reported [82]. The quantization of the electron states has been observed in resonance Raman scattering [83] and photoreflectance [82]. Investigators, however, have not reported on the quatization of the holes.

In this section we report room temperature measurements on two GaAs nipi superlattices having considerable different periods, i. e., 2200A and 460A and therefore considerably different built-in potentials, i. e., 85 meV and 1220 meV. In the thin period sample (460A) we observed a number of features in the spectrum both below and above

the band gap of GaAs. The spectrum was fit by a Derivative Functional Form (DFF) procedure, and we performed a theoretical calculation of the energy levels and intensities using a two band tight-binding model [84] with material parameters deduced from the growth conditions. In the thick period sample (2200Å) the spectrum is caused by Franz-Keldysh (FK) oscillations [6], the period being related to the large built-in dc field [85]. We used a second dc pump beam to change the electron-hole concentration and hence the built-in field. This variation in turn resulted in a change in FK oscillations, enabling us to gain information about the nature of the built-in field.

2.3.5.1 Small Period Sample -- Quantum size effect

The nipi superlattices used in this experiment were fabricated by molecular beam epitaxy at Hughes Research Laboratories. Sample nipi 497 has nominal $n=7\times10^{7}cm^{-3}$ and $p=5\times10^{17}\ cm^{-3}$ with $d_n=d_p=233Å$. The values of the built-in potential, $2V_n=85meV$, has been deduced from the growth parameters by assuming that the uncompensated carriers (electrons in this case) is exactly in the central region of the n layers (see section 1.2).

The dotted line in Figure 30 shows the 300K PR spectrum of sample nipi 497 in the 1.30-1.55 eV range using 6328A as the as pump at pump chopping frequency $\Omega_m= 150$ Hz. Experimental condition were in the

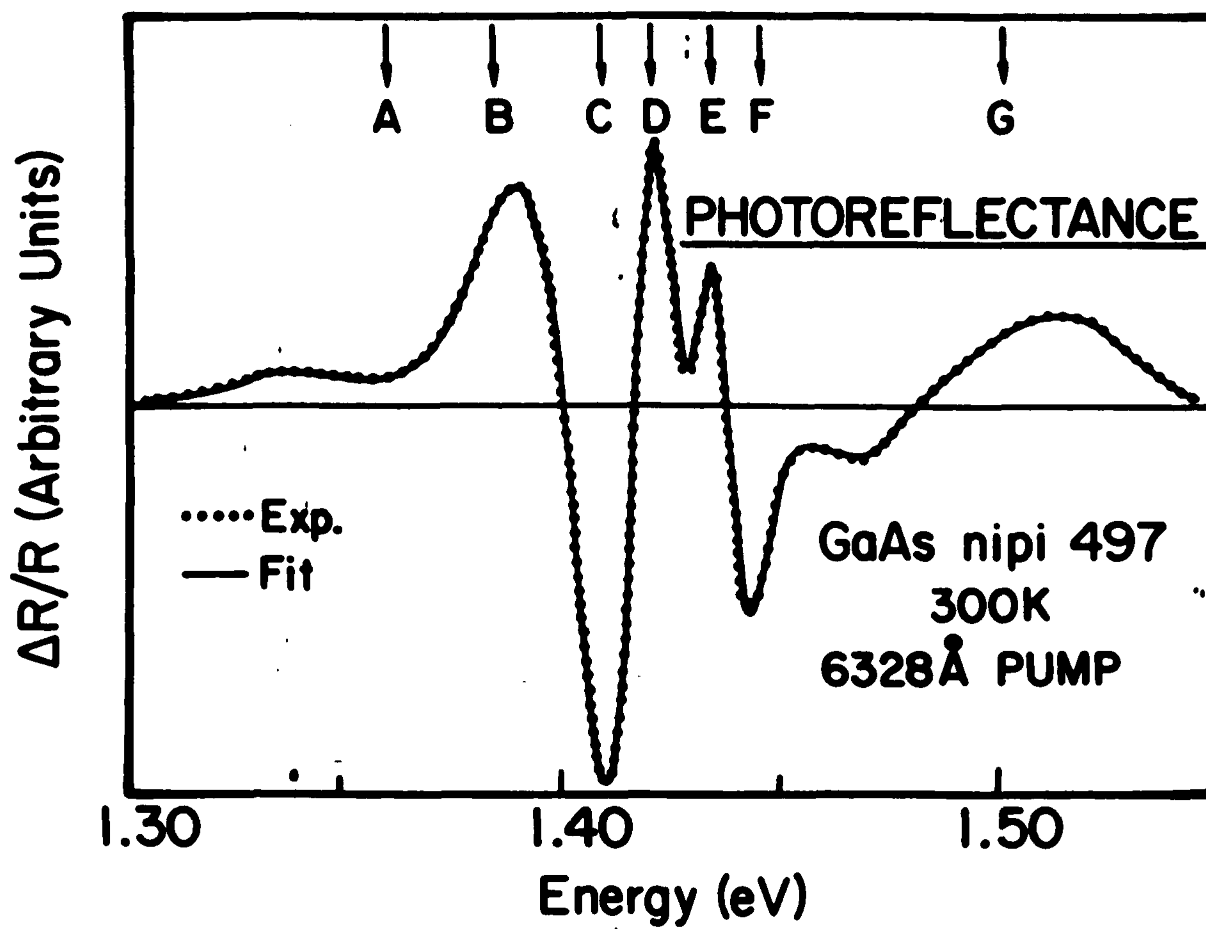

Figure 30: Photoreflectance GaAs doping superlattices nipi497

"low-field regime"; i. e., lineshape independent of ac pump beam intensity.

Before discussing the least-squares fit of the above result to derivative function from Eq(81), we would like to point out that the PR lineshape of nipi may be quite different from that of QW or SL. It has been proven that the subband energies of nipi structures are strong function of light intensity [86] [87] [88]. The recombination lifetime of electrons and holes are so long that very low electron-hole generation rate may induce large deviation of the carrier concentration [24]. The spatial separation between electron in n layer and holes in p layer flattens the self-consistent potential (see section 1.3). Thus the photo-injected carriers not only change the electric field but also change the subband energies. A first derivative function form for PR spectrum must be operative and possibly dominant. This corresponds to m=1 in Eq(81). However if third derivative is still dominant, m=3.

The solid line in Figure 30 is a least square fit of the experimental data to Eq(81) with m=1. The energies obtained are indicated by arrows at the top of the figure and are listed in Table 6, along with the corresponding m. We find the fit for m=3 is indistinguishable from the former fit, but that it yields somewhat different energies and broadening parameters. There are also given in Table 6. Thus, at pres-

Table 6: Comparison of experimental result and theoretical calculation of GaAs doping superlattices

A) obtained with m=1 in Eq(81), B) obtained with m=3 in Eq (81).

	Experiment				Theory	
	(A)		(B)			
Spectral Feature	Energy (eV)	Γ (meV)	Energy (eV)	Γ (meV)	Energy (eV)	Transition
A	1.360	21	1.350	74	1.369	13H(0)
B	1.385	20	1.386	27	1.381	22H(0)
C	1.408	12	1.4114	23	1.408	16H(π)
					1.408	24H(0)
D	1.420	6	1.419	17	1.417	17H(0)
					1.421	25H(π)
E	1.434	4	1.432	13	1.433	26H(0)
F	1.444	5	1.443	16	1.445	35H(0)
G	1.500	20	1.507	54	1.491	55H(π)

ent, we cannot make a definitive statement about the order of the derivative [64] [82] to fit PR spectra of nipi structures.

We have performed a theoretical calculation of the quantized energy levels and transition intensities using a two-band tight-binding model [84] with material parameters cited above. Listed in Table 6 are the energies of the most intense transitions (based on matrix elements and density of states) in the region of the the various spectral features.

The notation nmH(0) or nmH(π) denotes a transition from the nth conduction subband to the mth valence band of heavy-hole (H) character at the minizone center (0) or edge (π), respectively. We have fou~1 that transitions involving light-hole valence bands have considerably less amplitude than heavy-hole transitions. For example, if we examine the energy region in the vicinity of the D feature there is a theoretical 33H(0) transition at 1.419 eV but it is weak than 17H(0) or 25H(π) [see Table 6] and therefore has not been included.

Unfortunately, theoretical calculation using the growth parameters does not give a unique assignment to the experimental data. We have also performed the calculation using other values of n, p, d_n, and d_p such that $2V_n$ is kept constant at 85 meV. It is also possible to make a correspondence between theory and experiment, but not necessarily with the same transitions. Thus, for other material parameters (keeping $2V_n$ constant) there are also fairly strong theoretical transitions in the energy range of the various experimental features, but they do not necessarily correspond to the same transitions. For example, in other calculations the theoretical energies around the D feature (1.420 eV) are not 17H(0) or 25H(π).

The PR of InP nipi structures at 300K and 80K has been reported in Ref.[82]. The lineshapes have been fit by an expression based on a

Lorentzian oscillator model originally developed for the electroreflectance of excitons. This corresponds to m=2 in Eq(81). In interpreting their data the above-referenced authors considered only the quantization of the electron subbands and not the valence (and spin-orbit split) states. We found that the valence band quantization is an important consideration for our case.

The optical transition selection rules between confined valence and conduction band states are similar to those for a Type II superlattice, in which the electron and holes are spatially separated [89]. Thus $|n-m|$ must be even at the minizone center, while $|n-m|$ must be odd at the minizone edge. These selection rules do not hold for unconfined states. Since miniband dispersion was not considered in Ref. [82] these authors report contributions to the PR spectra from all miniband transitions.

2.3.5.2 Large Period Sample -- FKO

The nipi superlattice used in this section was sample NIPI 498. It consists of 21 layers of n (n_D=6.5 x 10^{17} cm^{-3}) and p (n_A=2.5x10^{17} cm^{-3}) doped GaAs layers with thicknesses of 800A (d_n) and 1400A (d_p), respectively. The build-in potential was estimated as about 1220 meV.

Plotted in Figure 31 is the PR spectrum from this sample. This spectrum of Figure 31 looks considerably different than that of Figure 30. PR spectrum from nipi 498 showed no evidence of any quantum confinement effect. However it exhibited the FKO features from the fundamental gap of GaAs E_g. We denoted them by A-E. The feature denoted F was corresponding to the spin orbit split component of E_g.

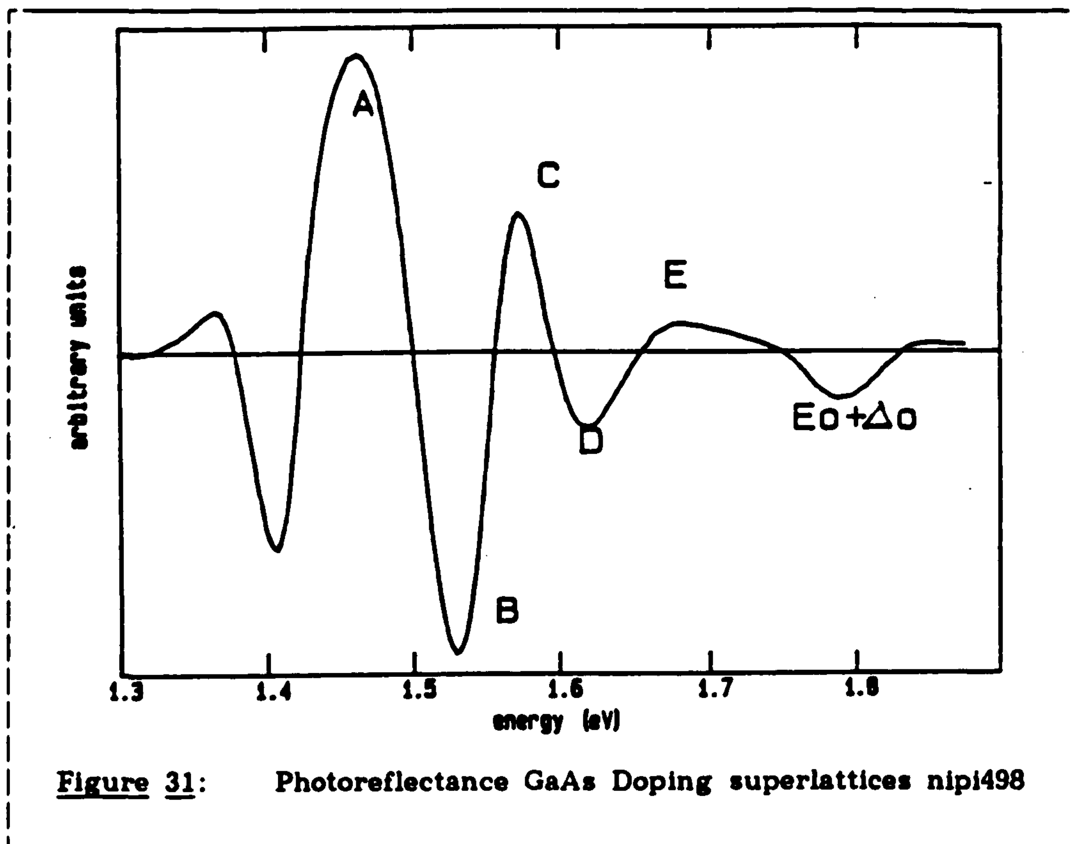

Figure 31: Photoreflectance GaAs Doping superlattices nipi498

The missing of the quantum confinement effect is due to the large separation of electron and hole pairs in the n and p type layers. The overlap of the quantized electron and hole wave functions is so small that almost no spatially indirect transition are possible. D. Miller, et al. have recently reported a theoretical calculation [90] on the compositional quantum wells and showed that if the slab thickness is great than 150A, then the classical FKO was recovered. This theory should alse applicable to the nipi structures. As we mentioned in the section (2.1.4), the periods of the FKO in modulation spectra were determined by the dc field not by the ac modulation field. Thus the FKO showed in Figure 31 was a measurement of the build-in nipi potential $2V_o$. From Figure 31 we deduced a field of $1.2x10^5$ V/cm. This agreed quit well with the result of average build-in field

$$2V_n/[(d_n+d_n)/2]=1.5x10^5 V/cm \quad (83)$$

It is also interesting to compare the result from nipi498 to that from InP/ITO. Both of them exhibited Franz-Keldysh Oscillations. However the signal intensity from nipi was two order of magnitude bigger than that from SCR. The biggest FKO we observed in InP SCR was about $\Delta R/R=3x10^{-4}$, in nipi 498 $\Delta R/R=3x10^{-2}$. There are two reasons for such a great enhancement: 1) the extremely long life time of photo-exited

carriers in nipi structure made the pump much more efficient. 2) The probe volume in nipi was much more bigger than that in SCR. For example, in InP/ITO the investigating depth was the depletion width, which was about 2000A. However in the nipi structure electric field covered a depth of 21x(800A+1400a)=46200A. For this case, the investigating depth should be the skin depth of the probe beam, which is about 10000A. Note also that, in contrast to the SCR, the spectrum from nipi shows no exciton features and no higher order FKO, which is also the result of thicker region of strong electric field.

2.3.5.3 Pumping Power Dependence

The experimental setup in this section is somewhat different from Figure 14. A three beam system was used here. In addition to the probe beam and the pump beam (which is chopped and we call it the ac pump beam), a third beam from an Ar^+ laser was focus on the sample surface. This third beam usually has a power much stronger than the ac pump beam. Since it is not chopped, we call it dc pump.

Plotted in Figure 32 is the PR spectra of sample NIPI 498 with dc pump power densities of 0.0, 5.8 and 37 mW/cm^2. As the dc pump power increases, the energy spacing between the FKO decreases, indicating an decreasing in the electric field in the nipi structure.

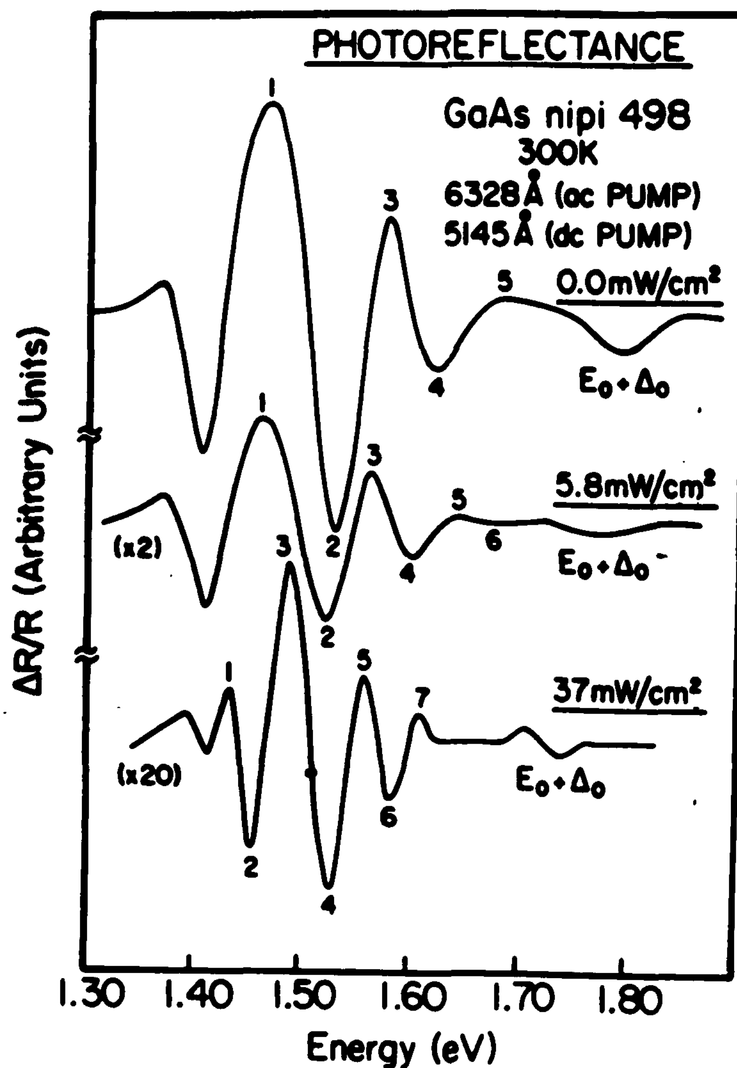

Figure 32: Photoreflectance PR spectra of GaAs nipi 498 for different dc pump power density.

The effect of the dc pump is to create more electron and hole pairs. Those electrons and holes stay at the center of the n and p type layers respectively (see section of nipi) and reduce the value of $2V_0$) and

hence the electric field. From the Frnz-keldysh Oscillations in Figure 32c, we deduct a build-in field of 0.3×10^5V/cm, a significant decrease in relation to the case of zero pump power (Figure 32a, 1.2×10^5V/cm).

2.3.5.4 Chopping Frequency Dependence

We have also investigated the dependence of the amplitude of PR signal on the chopping frequency Ω. Showing in Figure 33 are the result from sample nipi 497 and nipi 498. Curve A is the frequency dependence of nipi 497 (no dc pump). Curve B, C and D corresponds the power density of 0,60,and 600 mw/cm^2 for sample nipi 498. As the chopping frequency increases, the PR signal decreases. This change can be accounted for on the basis of the following considerations.

The chopped pump light is a square wave driver. When the light is on, it injects electron and hole pairs. These extra carriers change the built-in potential abruptly (see Figure 34). When the light is off, due to the large separation of electron and holes in nipi structure, these extra carriers decrease slowly and so dose the electric field. (Figure 34). Thus the effective modulation field can be written as

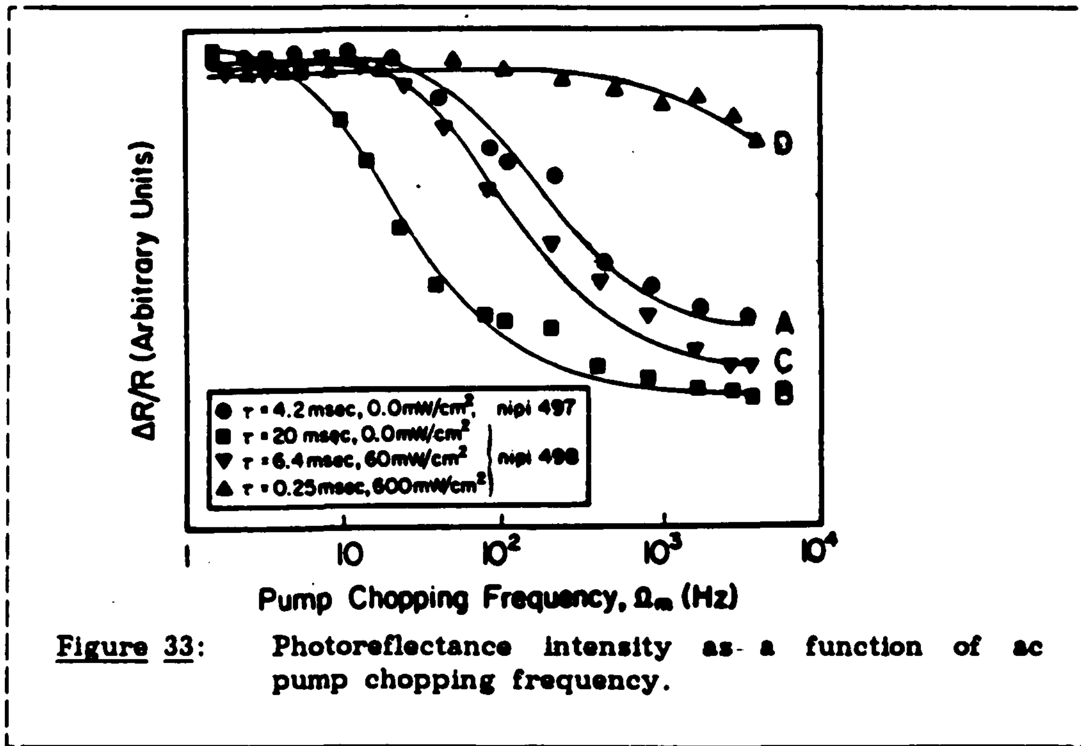

Figure 33: Photoreflectance intensity as a function of ac pump chopping frequency.

$$\Delta\mathcal{E} = \begin{cases} \exp(-t/\tau) & 0<t<T/2 \\ 1 & T/2<t<T \end{cases} \tag{84}$$

Where τ is the electron and hole recombination life time, T is the period of the chopping frequency Ω. The Fourier component at frequency Ω is

$$|C(\Omega)|^2 = |C(\Omega)=0|^2[(1-\exp(-\pi/\Omega\tau)^2\Omega^2\tau^2+4]/(4\Omega^2\tau^2+4) \tag{85}$$

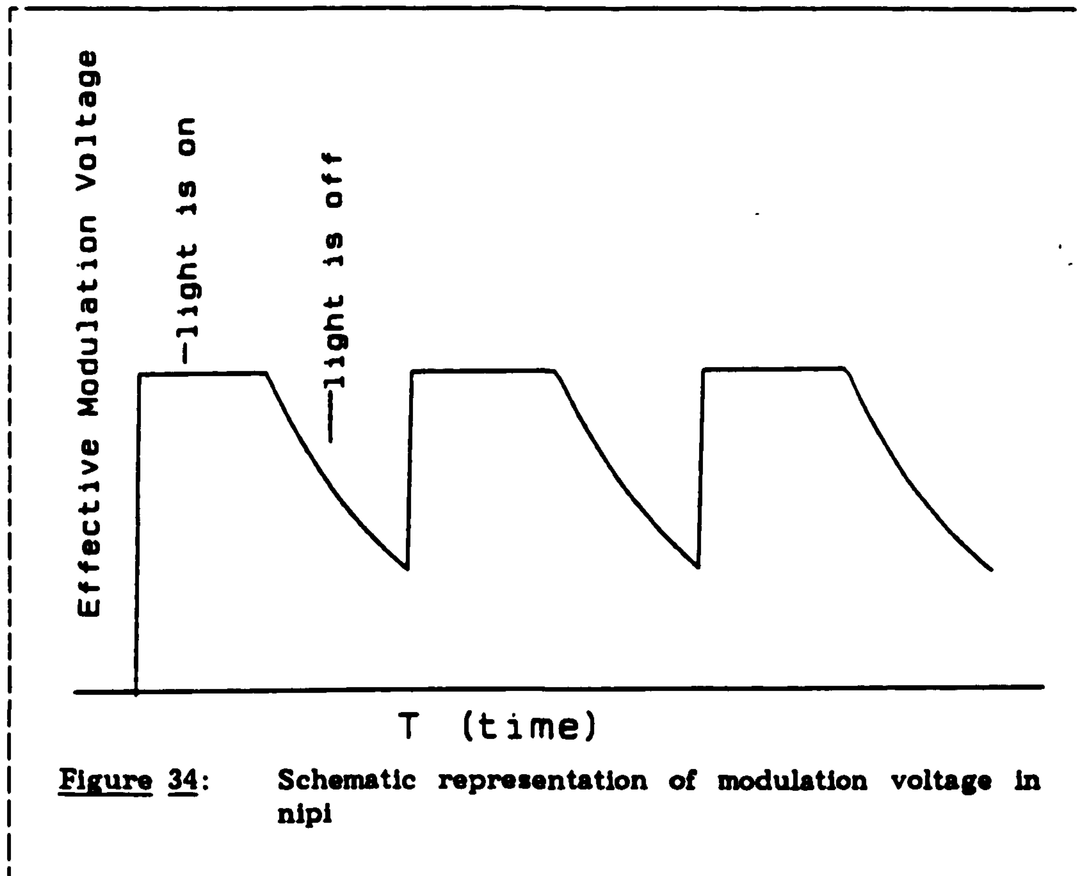

Figure 34: Schematic representation of modulation voltage in nipi

The solid lines in Figure 33 are least square fit to the above equation. From the fit we extract a time constant τ of 4.2 msec for sample nipi 497. For sample NIPI 498 with different dc pump power, the corresponding τ are listed Table 7. Increasing the dc pump power decreases the recombination lifetime since the built-in potential is decreased and hence there is less separation of carriers.

Table 7: Recombination life time of extra carriers in nipi498

sample	dc pump power (mW/cm^2)	recombination time (msec)
	0	20
nipi 498	60	6.4
	600	0.25

In conclusion, we have measured the room temperature PR spectra from two GaAs doping superlattices with substantially different layer thickness. In the small period sample PR structure are observed which are caused by transitions between quantized electron and hole states. A correspondence between experiment and theory can be made, although not uniquely. The other sample exhibits FK oscillations, the period being related to the dc built-in field rather than the ac modulation field. A second dc pump beam was used to reduced the built-in potential. The dependence of the PR on pump chopping frequency is a measure of the recombination lifetime.

Chapter III

RAMAN SPECTROSCOPY

3.1 General Background of Raman Scattering

In recent years, with the advent of lasers, light scattering has become one of the most powerful optical techniques for investigating elementary excitations in solids. In semiconductors, Raman scattering has been used to study phonons, single particle and collective charge carrier excitations, electron-phonon interaction, and the properties of defects or disorder in semiconductor alloys and amorphous materials[91] [8][92] [93] [94]. Depth profiling can be accomplished by using different excitation energies with different penetration depths. In addition, since it is a second-order process Raman scattering can provide symmetry information not available from first-order processes. Raman spectroscopy is complimentary to infrared absorption techniques in the sense that the symmetry of the modes coupled to the radiation field can be different, for example in the diamond structure the infrared inactive modes are Raman active.

3.1.1 Polarizability Theory of Raman Scattering

In Raman scattering (RS) the incident electromagnetic field couples with the phonon (lattice vibration field through the induced dipole moment [91] [8]. This is accomplished by the variation of the polarization tensor χ_{lm} which is defined by:

$$P = \chi\vec{\mathcal{E}} \tag{86}$$

where P is the dielectric polarization (dipole moment per unit volume) and $\mathcal{E}$ is the electric field.

The polarization tensor can be expended as:

$$\chi_{lm}=\chi^{(0)}{}_{lm}+\chi^{(1)}{}_{lm}*u+\chi^{(2)}{}_{lm}*u^{2}+\ldots \tag{87}$$

where u is a nuclear displacement during a normal vibration. Thus, for the jth normal mode:

$$u_j=u_{j0}\exp(i\omega_j t) \tag{88}$$

$$\chi^{(1)}{}_{lm}=\chi_{lm,j}=(\partial\chi_{lm}/\partial u_j) \tag{89}$$

Since

$$\mathcal{E}= \mathcal{E}_o\exp(i\omega_i t) \tag{90}$$

denotes the electric field of frequency ω_i we can write

$$P = \chi^{(0)}\mathcal{E}_0\exp(i\omega_i t) + \chi^{(1)}u_{j0}\mathcal{E}_0\exp[i(\omega_i \pm \omega_j)t]$$
$$+ \chi^{(2)}u^2_{j0}\mathcal{E}_0\exp[i(\omega_i \pm 2\omega_j)t] + \dots\dots\dots\dots \tag{91}$$

The first term of the above equation gives rise to Rayleigh scattering in which the frequency of the radiation remains unchanged during the scattering process (i. e., elastic scattering). The second term, involving the derivative of the polarizability, constitutes first-order Raman scattering, which is an inelastic scattering process. The incident photon (ω_i, k_i) is absorbed, and the system makes a transition from an initial state (n,v) where n and v represent the electronic and vibrational quantum numbers, to an intermediate state(n', v'). The system eventually decays to the final state (n, v±1). In the process a phonon (ω_j, q_j) is created or annihilated and a photon of different frequency and wavevector (ω_s, k_s) is emitted so that energy and momentum are conserved

$$\hbar\omega_s = \hbar\omega_i \pm \hbar\omega_j \tag{92}$$

$$\hbar k_s = \hbar k_i \pm \hbar q_j \tag{93}$$

where the (+) sign is denoted as anti-Stokes scattering, while the (-) sign is Stokes scattering (see Figure 35).

The magnitude of the scattering wavevector depends on the scattering geometry. The largest value for $|q_j|$ is obtained for backscattering in which case

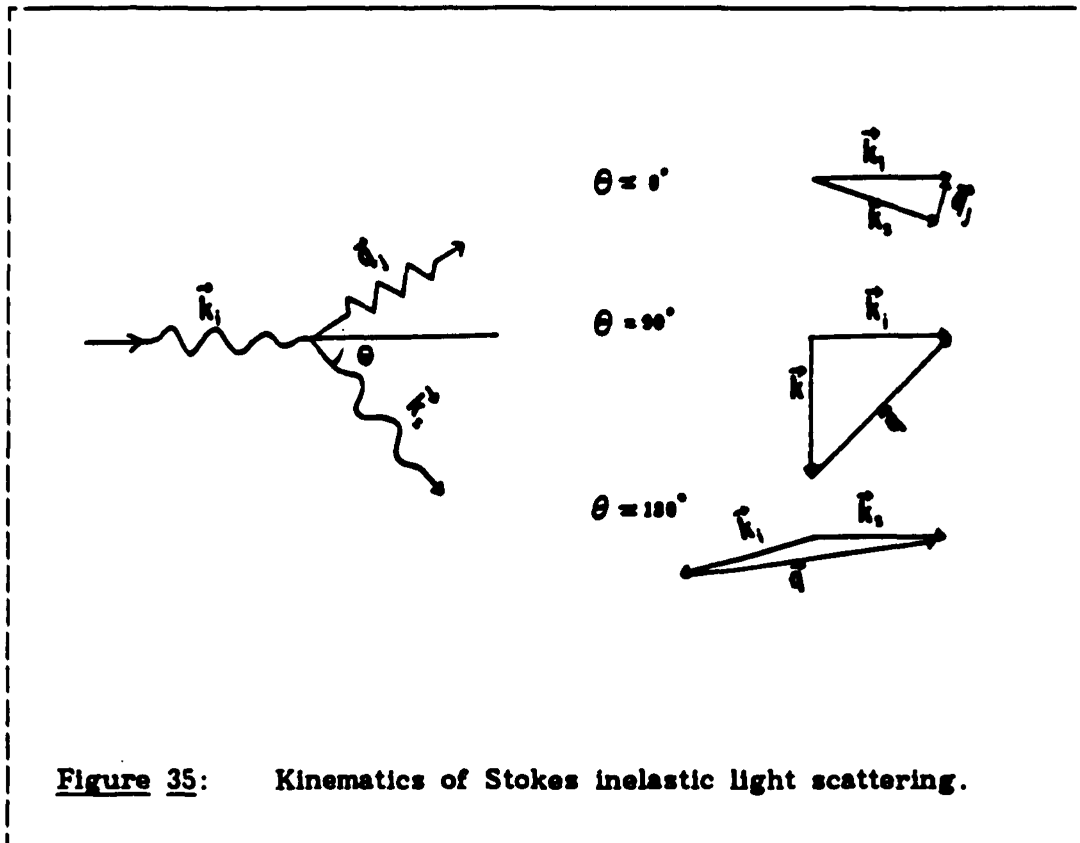

Figure 35: Kinematics of Stokes inelastic light scattering.

$$|q_j| = |k_i| + |k_s| = \{n(\omega_i)\omega_i + n(\omega_s)\omega_s\}/c \tag{94}$$

where $n(\omega)$ is the refractive index of the medium at frequency ω and c is the velocity of light. In typical Raman scattering experiments (in visible or near visible) $\hbar\omega_i \approx \hbar\omega_s \approx 2.5$ ev and $n \sim 4$ and hence the maximum wavevector transfer $|q_j| \leq 10^6$ cm^{-1}. This is only a small fraction of the typical wavevector of the Brillouin zone (BZ) edge phonons ($\sim 2\pi/a_l \approx 10^8$ cm^{-1}). Thus under conditions of wavevector conser-

vation only phonons near the zone center participate in first order Raman scattering.

3.1.2 Microscopic Description

In a microscopic description the first order Raman scattering is viewed as a three step process[8] [92] [95]. (see Figure 36)

1. a photon with energy ω_l is absorbed creating an electron-hole pair in the state $|l\rangle$
2. a phonon with energy ω_j is created (or destroyed) and the electron-hole pair is scattered to the state $|m\rangle$
3. the electron-hole pair recombines and a photon with energy ω_s is emitted.

The momentum is conserved in each step whereas as energy is conserved only in the total process, i.e., each of the above transitions can be real or virtual. These processes can occur in any time order giving rise to six types of processes. Using third order time dependent perturbation theory one obtains the following expression for the first order susceptibility[95].

$$\chi^1_{\alpha\beta}(j)=R\Sigma\langle 0|p_\alpha|m\rangle\langle m|H_{EL}|l\rangle\langle l|p_\beta|0\rangle/(E_m-h\omega_s)(E_l-h\omega_l)$$

$$+ \text{ five permutation terms.} \qquad (95)$$

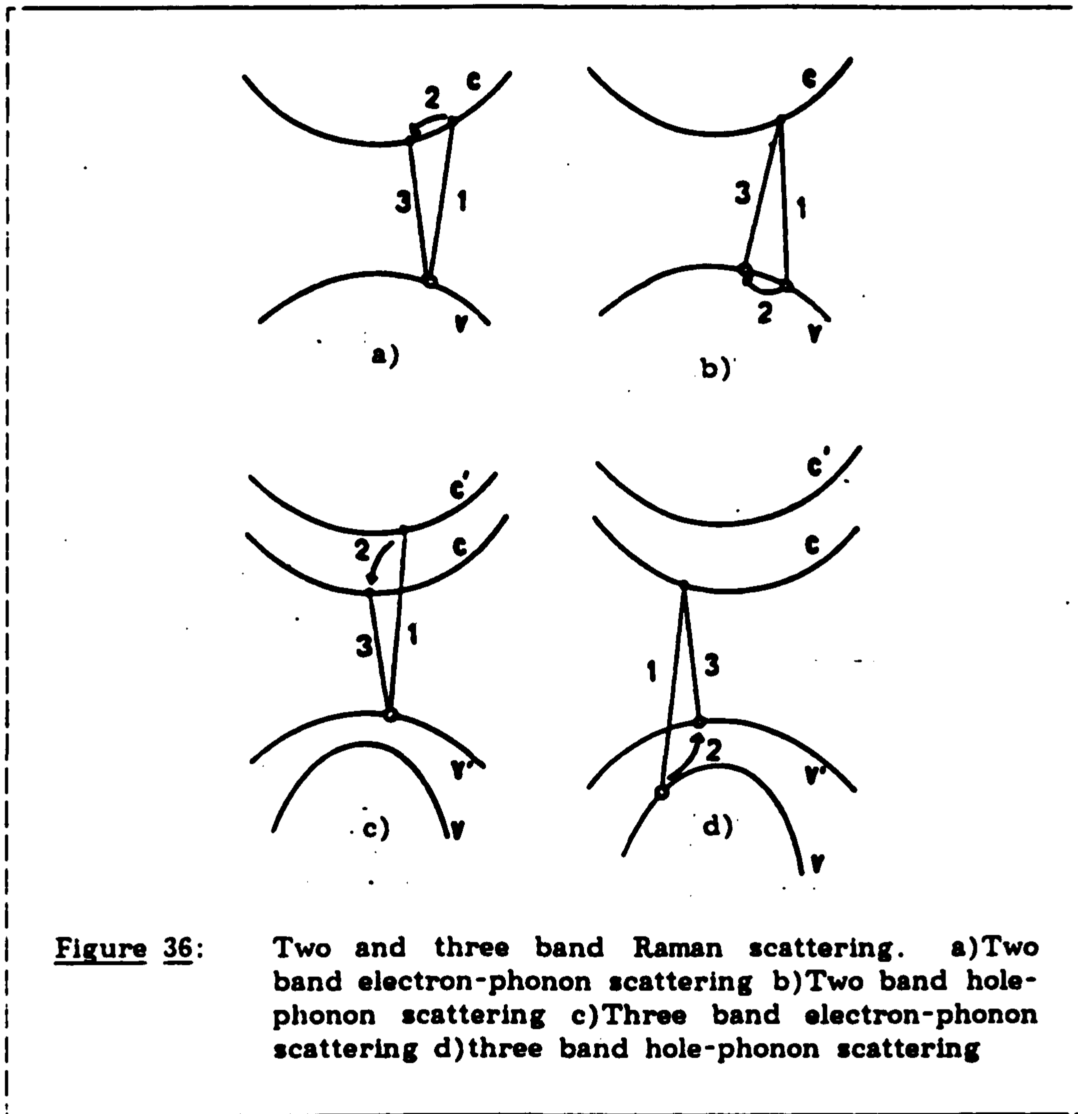

Figure 36: Two and three band Raman scattering. a)Two band electron-phonon scattering b)Two band hole-phonon scattering c)Three band electron-phonon scattering d)three band hole-phonon scattering

where

$$R = \mathcal{E}^2 / m^2 \omega_s^{\ 2} V \tag{96}$$

and H_{EL} is the electron-phonon Hamiltonian, p_α and p_β are electron momentum operators and |0> is the "one electron" wave function for the ground state. Under resonance conditions $h\omega_i$ and/or $h\omega_s$ are close to the energies of the intermediate states E_m or E_l giving rise to large enhancements in $\chi^{(1)}{}_{\alpha\beta}(j)$. Figure 36a and Figure 36b distinguish two and three band processes. The two band processes involve intraband matrix elements of H_{EL} whereas three band processes involve interband matrix elements.

In addition to the allowed scattering mechanisms other perturbations (applied or built-in electric field, stress etc.) may also affect the phonon induced change in the susceptibility thus contributing to the first order Raman scattering. Including these contributions we obtain [92][96]:

$$\chi^{(1)}{}_{\alpha\beta}(\omega_i,\omega_s)=(\partial\chi_{\alpha\beta}/\partial u_j)u_j+(\partial\chi_{\alpha\beta}/\partial\nabla u_j)iu_jq_j+ \\ (\partial\chi_{\alpha\beta}/\partial u_j\partial\mathcal{E}_a)u_j\mathcal{E}_a+(\partial\chi_{\alpha\beta}/\partial u_j\partial\eta)u_j\eta+\ldots\ldots \quad (97)$$

$$\chi^{(1)}{}_{\alpha\beta}(\omega_i,\omega_s)=\chi^{(1)}{}_{\alpha\beta}(j)+i\chi^{(1)}{}_{\alpha\beta q}(j)+\chi^{(1)}{}_{\alpha\beta E}(j)+\ldots \quad (98)$$

where we have expanded $\chi^{(1)}{}_{\alpha\beta}$ in u_j, ∇u_j, $\mathcal{E}_a$ (the applied electric field) and η, the strain. $\chi^{(1)}{}_{\alpha\beta}(j)$ which depends only on u_j describes the "allowed" one phonon scattering, $\chi^{(1)}{}_{\alpha\beta E}(j)$ describes the contribu-

tion to the first order Raman scattering due to the field induced atomic displacements. $\chi_{\alpha\beta q}$ represents the linear q-dependent contribution in the case of longitudinal optic (LO) phonon-Frolich interaction and $\chi_{\alpha\beta\eta}$ represents the contribution to $\chi^{(1)}_{\alpha\beta}$ due to stress. The selection rules for scattering due to $\chi_{\alpha\beta E}$, $\chi_{\alpha\beta q}$ and $\chi_{\alpha\beta\eta}$ are usually different from $\chi^{(1)}_{\alpha\beta}$ and hence are called "forbidden" scattering.

The scattering efficiency (Raman cross section), S, defined as the ratio of the scattered intensity into unit solid angle per unit time per unit frequency interval, to the incident intensity is given by[92]

$$S^{(1)}(j) = |e_s.\chi.e_i|^2 \, V\omega^4_s/c^4 \tag{99}$$

where e_i and e_s are the unit polarization vectors of the incident and scattered light, respectively, V is the scattering volume and c is the velocity of light.

3.1.3 Selection Rules

In addition to the restrictions on scattered light imposed by the kinematics of the scattering process (see Figure 35) selection rules arise for the tensor components $\chi_{\alpha\beta}$ from the crystal symmetry. From group theory, one obtains the condition for the existence of the nonzero components $\chi^{(1)}_{\alpha\beta}(j)$ as

$$\Gamma(u_j) \times \xi_{\alpha\beta} \rightarrow \Gamma_1 \tag{100}$$

where Γ's are the irreducible representations of the crystal point group under consideration. $\Gamma(u_j)$ corresponds to the normal co-ordinate u_j, $\xi_{\alpha\beta}$ transforms like the components of a second-rank tensor and Γ_1 is the totally symmetric representation. Similarly the selection rule for other terms of $\chi_{\alpha\beta}$ can be written as[92] [95]

$$\xi_{\alpha\beta q}: \quad \Gamma(u_j) \times \Gamma(q) \times \xi_{\alpha\beta} \rightarrow \Gamma_1 \tag{101}$$

$$\xi_{\alpha\beta E}: \quad \Gamma(u_j) \times \Gamma(E) \times \xi_{\alpha\beta} \rightarrow \Gamma_1 \tag{102}$$

$$\xi_{\alpha\beta\eta}: \quad \Gamma(u_j) \times \Gamma(\eta) \times \xi_{\alpha\beta} \rightarrow \Gamma_1 \tag{103}$$

Γ(E) and Γ(q) are irreducible representations transforming like the vectors q and E, respectively. Γ(η) transforms like a second-rank tensor.

The materials under study have a zincblende structure and hence belong to the T_d point group. The optic vibrations belong to Γ_{15} representation of the T_d group which has a three fold degenerate irreducible representation at q=0.

Choosing our co-ordinate system to coincide with the crystal axes x = (100), y = (010) and z = (001) the "allowed" Raman tensor ${\chi^{(1)}}_{\alpha\beta}$ for the three optic modes are listed in Table 8. Since the scattered intensity is proportional to $|e_i . \chi . e_s|^2$ the polarization of the incident and scattered light further imposes restrictions on the first order scatter-

Table 8: The allowed Raman tensor

x	y	z
$\begin{vmatrix} 0 & 0 & 0 \\ 0 & 0 & d \\ 0 & d & 0 \end{vmatrix}$	$\begin{vmatrix} 0 & 0 & d \\ 0 & 0 & 0 \\ d & 0 & 0 \end{vmatrix}$	$\begin{vmatrix} 0 & d & 0 \\ d & 0 & 0 \\ 0 & 0 & 0 \end{vmatrix}$

ing. For example, in backscattering from (100) surface only LO phonon is allowed. Table 8 [96].

Table 9: The linear q induced Raman tensor

$$\begin{vmatrix} cq_x & bq_y & bq_z \\ bq_y & aq_x & 0 \\ bq_z & 0 & aq_x \end{vmatrix} \quad \begin{vmatrix} aq_y & bq_x & 0 \\ bq_x & cq_y & bq_z \\ 0 & bq_z & aq_y \end{vmatrix} \quad \begin{vmatrix} q_x & 0 & bq_x \\ 0 & aq_z & bq_y \\ bq_x & bq_y & cq_z \end{vmatrix}$$

The q-dependent and electric field induced and strain induced Raman tensors $\chi^{(1)}_{\alpha\beta q}$ and $\chi^{(1)}_{\alpha\beta\eta}$ and $\chi^{(1)}_{\alpha\beta E}$ and are also listed in Table 9, Table 10 and

Table 10: Electric field induced Raman tensor

$$\begin{vmatrix} cE_x & bE_y & bE_z \\ bE_y & aE_x & 0 \\ bE_z & 0 & aE_x \end{vmatrix} \quad \begin{vmatrix} aE_y & bE_x & 0 \\ bE_x & cE_y & bE_z \\ 0 & bE_z & aE_y \end{vmatrix} \quad \begin{vmatrix} aE_x & 0 & bE_x \\ 0 & aE_z & bE_y \\ bE_x & bE_y & cE_z \end{vmatrix}$$

Table 11: Strain induced Raman tensor

$$\begin{vmatrix} c\eta_{yz} & f\eta_{zx} & f\eta_{xy} \\ f\eta_{zx} & e\eta_{yz} & b\eta_{xx}+g(\eta_{yy}+\eta_{zz}) \\ f\eta_{xy} & b\eta_{xx}+g(\eta_{yy}+\eta_{xx}) & e\eta_{yz} \end{vmatrix}$$

$$\begin{vmatrix} e\eta_{zx} & f\eta_{yz} & b\eta_{yy}+g(\eta_{zz}+\eta_{xx}) \\ f\eta_{yz} & c\eta_{zx} & f\eta_{xy} \\ b\eta_{yy}+g(\eta_{zz}+\eta_{xx}) & f\eta_{xy} & e\eta_{yz} \end{vmatrix}$$

$$\begin{vmatrix} e\eta_{xy} & b\eta_{xx}+g(\eta_{yy}+\eta_{xx}) & f\eta_{yz} \\ b\eta_{zz}+g(\eta_{xx}+\eta_{yy}) & e\eta_{xy} & f\eta_{zx} \\ f\eta_{yz} & f\eta_{zx} & c\eta_{xy} \end{vmatrix}$$

3.1.4 Coupled LO Phonon Plasmon Modes.

The presence of charge carriers in heavily doped semiconductors give rise to plasma oscillations with a frequency

$$\omega_p^2(q) = (4\pi Ne^2/\varepsilon_\infty m^*)^{\frac{1}{2}} + (3/5)*(qV_F)^2 \qquad (104)$$

where $\omega_p(q)$ is the plasma frequency, N is the number density and m^* is the effective mass of the charge carriers, ε_∞ is the high frequency dielectric constant , e is the electronic charge and $V_F=hk/m^*$ is the Fermi velocity. If the plasma frequency is close to that of the LO phonon frequency the two modes of collective oscillations (electronic and atomic) will be strongly coupled with each other through the depolarizing field they produce.

The frequencies of the coupled LO phonon-plasmon modes are the roots of the total dielectric response, i.e.,

$$\varepsilon(q,\omega) = \varepsilon_\infty + \varepsilon_{lattice}(\omega) + \varepsilon_{plasma}(q,\omega) \tag{105}$$

$$= \varepsilon_\infty[(\omega^2_{LO}-\omega^2)/(\omega^2_{TO}-\omega^2)] + \varepsilon_\infty\omega_p{}^2/\omega^2 = 0 \tag{106}$$

where ω_{LO} and ω_{TO} are the frequencies of the LO and TO phonons. From the above Eqn. one obtains the frequencies of the coupled modes as:

$$\omega_\pm = \tfrac{1}{2}[\omega_p{}^2 + \omega_{LO}{}^2 \pm ((\omega_p{}^2 + \omega^2{}_{LO})^2 - 4\omega_p{}^2\omega^2{}_{TO})^{\frac{1}{2}})] \tag{107}$$

Shown in Figure 37 is the frequencies of the coupled modes as a function of the electron concentration in GaAs, calculated for 5145 A laser line.

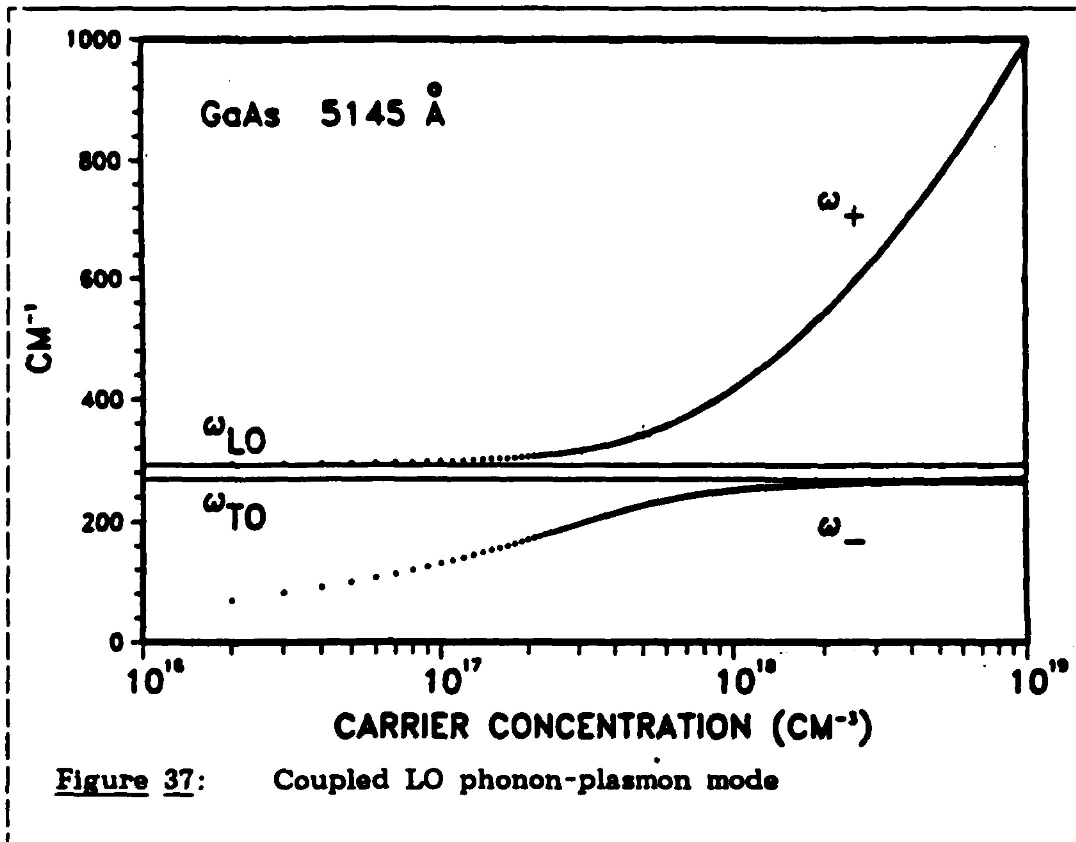

Figure 37: Coupled LO phonon-plasmon mode

3.2 Experimental Details

The functional block diagram of the experimental setup for Raman scattering is shown in Figure 38. The collimated, monochromatic beam from a 6 watt Coherent Ar^+ laser was used as the incident radiation. The laser beam is reflected from two mirrors, passes through an interference filter (I.F.) having a band pass of ~ 5 A which eliminates any spurious emissions, (such as the plasma oscillations from the laser

medium), a pin hole collimator, and is then focused onto the sample by a cylindrical lens (focal length=6 cm). The purpose of this lens was to focus the beam to a line rather than a point, thus reducing the incident power density and hence minimizing the sample heating. Typically the laser power used was ~ 250 mw. The backscattered light was collected at the entrance slit of the spectrometer by a camera lens composed of a series of lenses (focal length = 13.5 cm and f number = 1.8). The large index of refraction (~ 4) of the semiconductor ensures that both the incident and scattered angles inside the semiconductor are small (typically ~10°).

The Raman spectrometer is a Spex 1401 double monochromator which consists of two identical units. Each unit has two identical spherical mirrors and one vertically mounted grating. The gratings were holographic and were blazed at 5000 A. A synchronous rotation of the two gratings provides a scanning in photon energy. The photons which emerge from the exit slit of the spectrometer are focussed onto the GaAs cathode of the cooled photomultiplier (RCA N-40436). The thermoelectrical cooling of the photomultiplier cathode significantly reduces the "dark current" which is due to thermionic emissions of electrons from the cathode and dynodes even in the absence of any incident light. The anode current pulses are converted to voltage pulses which

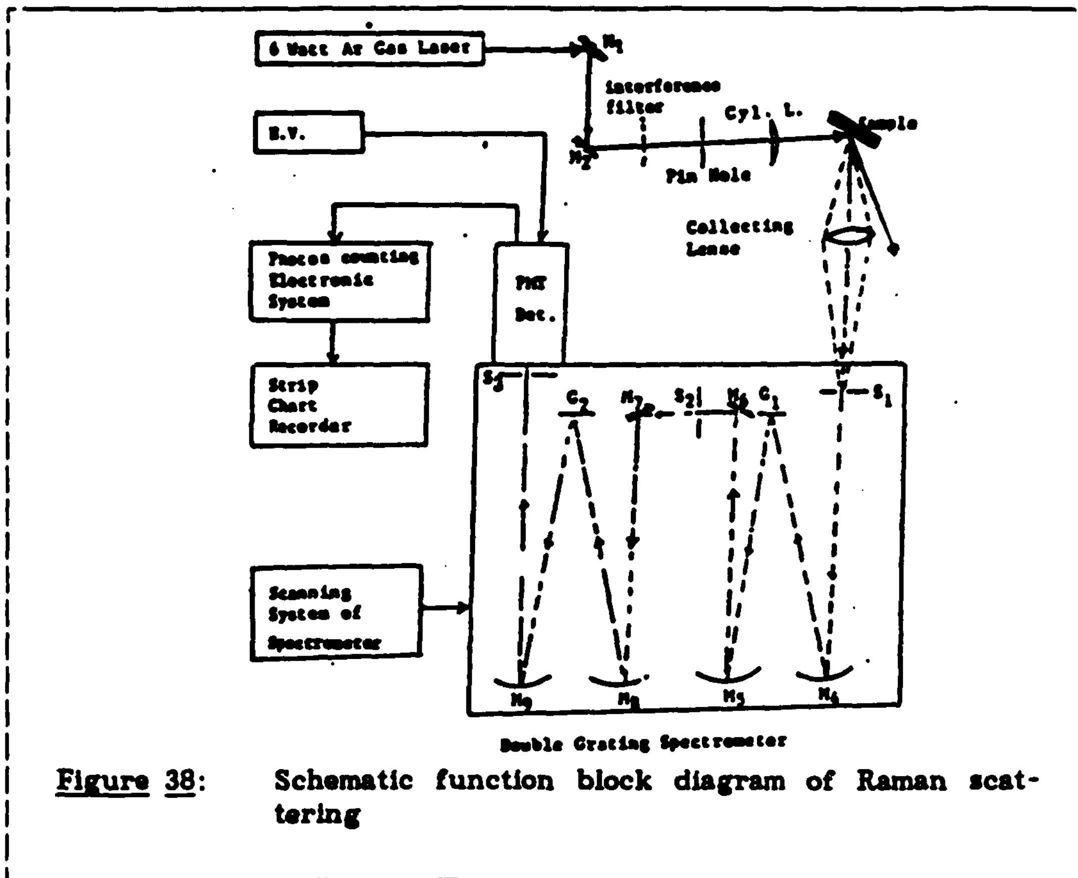

Figure 38: Schematic function block diagram of Raman scattering

are fed through a discriminator which filters voltage pulses which are below a preset level thus reducing the effects of dark current. These voltage pulses are collected by a photon counting system and the time averaged results are recorded on a chart recorder.

3.3 Experimental Results

3.3.1 Surface Charge Layer in <100> GaAs

Although Raman scattering (RS) from the longitudinal optic (LO) phonon mode has been used as a nondestructive, contactless method to gain information about surface electric fields and space charge region (SCR) from the <110> surfaces [11] [97] and <111> surfaces [11] [98] [99] of zincblende-type semiconductors, relatively little work has been done on the <100> face [94] [100] [101]. The underlying reason is that from the <110> and <111> surfaces there is a field-independent reference, i.e. the transverse optic (TO) phonon mode (surface electric fields affect only the LO-mode see Table 9 [96]). On the other hand, in backscattering from the <100> face, the TO-phonon is forbidden (even in the presence of an electric field[96]) and hence quantitative measurements from this crystallographic direction are much more difficult. However, since the <100> surface is of much more technological interest, we have undertaken the present study.

In this section we report measurements using LO phonon RS to gain quantitative information about the width of the SCR (and hence surface electric fields) as well as the bulk carrier concentration, n, from <100> n-GaAs. The room temperature RS, in the backscattering geometry, has been studied from a number of GaAs samples with 4×10^{17} cm^{-3}

$<n<1 \times 10^{19}$ cm^{-3} using as an excitation source several different wavelengths of an Ar^{+} laser. From the position of the coupled plasmon-LO phonon (CP-LOP) modes we have determined the carrier concentration, n[94] [102]. By comparing the intensity (at different wavelengths) of the observed uncoupled LO mode, origination in the SCR, with the signal from a piece of undoped <100> material it is possible to experimentally determine L_s, the width of the SCR. There is very good agreement between experiment and a generalized theory which considers both non-degenerate and degenerate charge carrier cases.

In the general case, for optical penetration depths larger than the depletion width, the Raman spectra from an n-type zincblende-type semiconductor will show the peaks of the CP-LOP modes (L_+,L_-) from the bulk as well as the uncoupled LO phonon mode originating in the depletion layer[94] [98]. The frequencies of L_+ and L_- are ω_+ and ω_- in Figure 37. The intensity of the unscreened LO phonon depends on the width of the layer and the penetration of the incident light [98] [94]. Pinczuk et al.[98] pointed out that by assuming the Raman scattering from the LO phonon in the depletion layer is similar to that in an undoped crystal, the intensity of the unscreened LO phonon $I^{\lambda}(LO)$, originating in the SCR can be written as[98]

$$I^{\lambda}(LO) = I_o^{\lambda}(LO)\{1-\exp[-2L_s/d_o(\lambda)]\} \qquad (108)$$

where $I^{\lambda}_{e}(LO)$ is the intensity of the LO mode (at excitation wavelength λ) from a piece of undoped material, L_s is the width of the SCR and $d_o(\lambda)$ is the optical skin depth. Equation (108) can be used to determine L_s from measurements of the ratio $I^{\lambda}(LO)/I^{\lambda}_{o}(LO)$. The quantity L_s can be related to the surface band bending in a doped zincblende-type semiconductor.

We have investigated nine different GaAs samples, both bulk and thin film, all Si-doped. Eight were MBE grown epitaxial layers fabricated at Eaton Corp/AIL Division. They are designated samples SUM12C ($n=5.0\times10^{17}$ cm^{-3}), CS5B ($n=5.7\times10^{17}$ cm^{-3}), SUM5G ($n=1.1\times10^{18}$ cm^{-3}), 798-7C ($n=3\times10^{18}$ cm^{-3}), SUNG-4D ($n=5\times10^{18}$ cm^{-3}), 782-8A ($n=6\times10^{18}$ cm^{-3}), SUM-2D ($n=7.0\times10^{18}$ cm^{-3}) and 798-5G ($n=1\times10^{19}$ cm^{-3}), The ninth sample was a piece of bulk material ($n=1.5\times10^{18}$ cm^{-3}). The carrier concentrations listed in parentheses were determined from transport measurements. The <100> face of the bulk sample was oriented to 1° by X-ray Laue backscattering. The surface was then prepared by polishing with 1μm, and 0.05μm, grit alumina powder for 60 min, 1:4 Syton in de-ionized water polishing for 60 min. and 0.1% Br/Methanol chemo-mechanical polish for 5 min. The reference samples (semi-insulating) were CS(MBE), SUMITOMO (MBE) and 798-4 (LEC) with carrier concentration less than 1×10^{14} cm^{-3}. To eval-

uate the possible influence on the RS intensity of a thin oxide film, several samples (both doped and undoped) were free-etched in a 0.5% Br/Methanol solution for two minutes. No difference in the RS intensity before and after etching was found.

3.3.1.1 Determination of Free Carrier Concentration

In order to determine n we measured the CP-LOP features (L_+,L_-) using the 4880A line of an Ar^+ laser. The relation between the peak position of L_+ and L_- as a function of n for different wavelengths is given by Eq (107). Non-parabolic corrections to m_o^* are considered here, as discussed in Ref.[94],[102] and [103].

The incident power was about 300 mW. The laser beam was line focused onto the sample by a cylindrical lens to minimize heating effects. The temperature at the surface was estimated to be about 340°-350°K from the intensity ratio between the Stokes and anti-Stokes phonon lines.

Shown in Figure 39a, Figure 39b and Figure 39c are typical Raman spectra obtained from <100> GaAs samples CS5B, SUM5G, 782-8A, respectively. The CP-LOP modes are designated L_+ and L_-. In the free-carrier density range of $N>1x10^{18}$ cm^{-3} L_- is almost independent of n (see Figure 37), and hence only L_+ was employed to determine the bulk carrier concentration in this region. On the other hand, in the

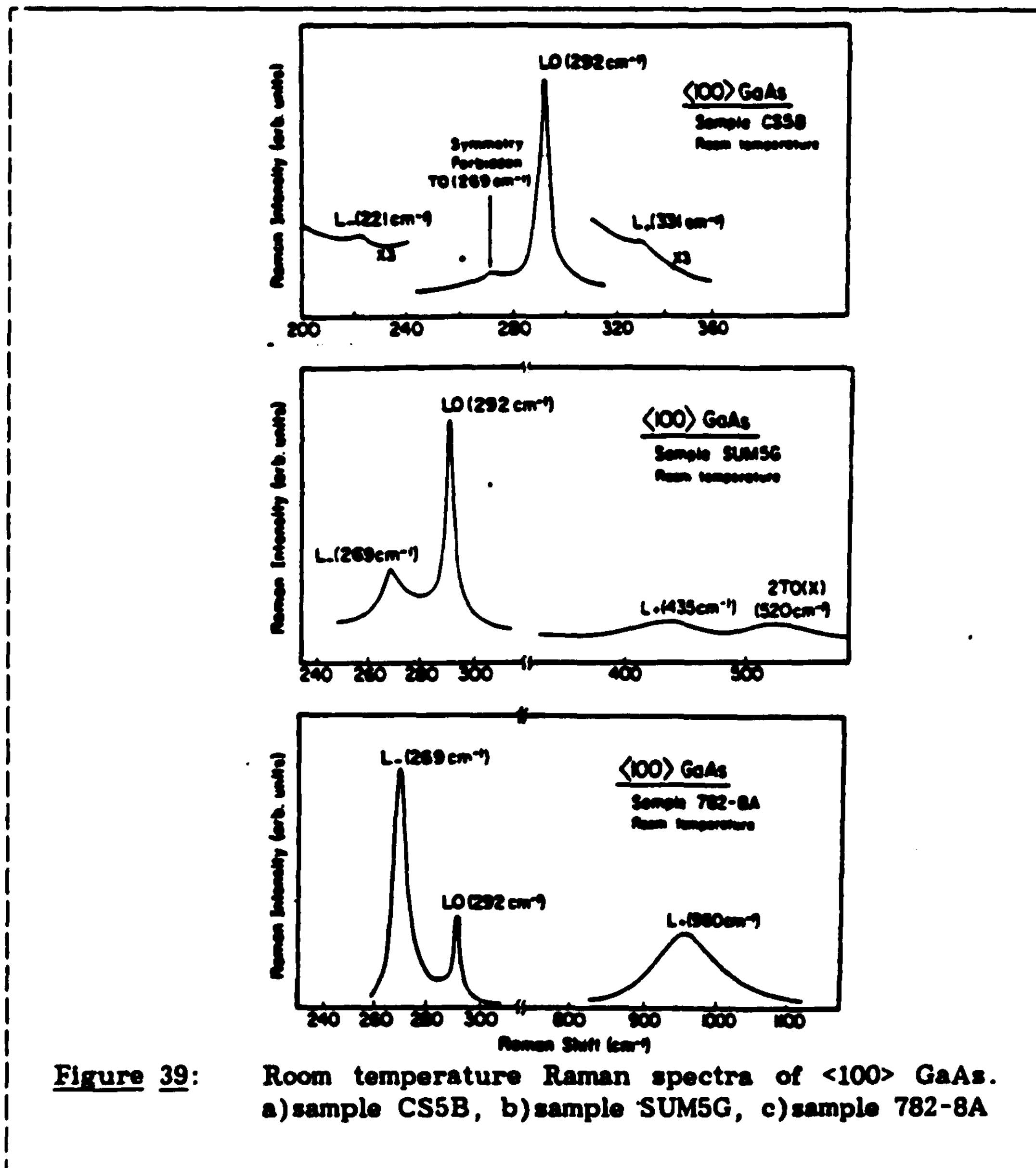

Figure 39: Room temperature Raman spectra of <100> GaAs. a)sample CS5B, b)sample SUM5G, c)sample 782-8A

region of $n<1x10^{18}$ cm^{-3} both L_- and L_+ were used. The measured

positions of L_+, L_- for the five samples and the corresponding carrier concentrations n are summarized in Table 12 Also listed are values of n from transport measurements.

Table 12: Free carrier concentration measurements

SAMPLE	$\omega_+(cm^{-1})$	$\omega_-(cm^{-1})$	$n(cm^{-3})^{(a)}$	$n(cm^{-3})^{(b)}$
CS5B	333±10	221±3	$4.0X10^{17}±0.3X10^{17}$	$5.7X10^{17}$
SUM12C	338±10	225±3	$4.5X10^{17}±0.3X10^{17}$	$5.0X10^{17}$
SUM5G	435±10	269±2	$1.1X10^{18}±0.1X10^{18}$	$1.1X10^{18}$
BULK	470±10	269±2	$1.3X10^{18}±0.1X10^{18}$	$1.5X10^{18}$
798-7C	617±10	269±2	$2.7X10^{18}±1.0X10^{18}$	$3.0X10^{18}$
SUNG-4D	839±10	269±2	$6.4X10^{18}±1.0X10^{18}$	$5.0X10^{18}$
SUNG-2D	903±10	269±2	$7.7X10^{18}±1.0X10^{18}$	$7.0X10^{18}$
782-8A	960±10	269±2	$9.0X10^{18}±1.0X10^{18}$	$6.0X10^{18}$
798-5G	1015±10	269±2	$1.05X10^{19}±1.0X10^{18}$	$1.0X10^{19}$

a) From position of L_+, L_- .

b) From transport measurement .

Note that in Figure 39a in addition to the CP-LOP modes, RS is observed from the uncoupled LO phonon (292 cm^{-1}) originating in the depletion layer. As n increases the intensity of the uncoupled LO mode decreases relative to L_+ and L_-. The intensity of this feature is of

major interest in this section. The linewidths Γ of the uncoupled LO phonon mode are less than 3 cm^{-1}. This demonstrates that the quality of the crystals is quite good [21]. Some other aspects of the spectra should also be pointed out. The features at 269 cm^{-1} in Figure 39a is the symmetry forbidden TO-mode which may be activated by the surface morphology or slight misorientation of the sample surface while the feature at 520 cm^{-1} of Figure 39b is due to a two-phonon process [2TO(X)].

3.3.1.2 Measurements of Depletion Widths

The measurements of the relative intensity of RS from the LO phonon in the SCR of the doped materials $I^{\lambda}(LO)$ to that from the undoped samples $I^{\lambda}_{o}(LO)$ were carried out with special care. Two samples, doped and undoped, with their crystal axes oriented in the same directions (to avoid polarization differences) were mounted close together on an aluminum plate using heat conducting epoxy. The aluminum plate was mounted on a movable holder to enable us to alternate samples with minimum change in the focusing conditions. Since in this aspect of the experiment we were not interested in the details of the line shape or exact peak position, but rather in optimal intensity, the instrument resolution was not important. Hence, the slits were set for 6 cm^{-1} resolution. The ratio of LO intensities i.e. $I^{\lambda}(LO)/I^{\lambda}_{o}(LO)$ was reprodu-

cible to within 10% at all wavelengths. The reference quantity $I^{\lambda}_{o}(LO)$ from different undoped samples also was reproducible to better than 10%.

Previous studies have shown that the effects of optically excited carriers will reduce the measured depletion layer [98] [104]. To avoid this effect, we employed a very low power density for the intensity measurements. The laser power used was 5mW and the power density on the sample surface was about $0.1W/cm^2$. In order to enhance the scattering light intensity without increasing the power density on the surface, we maximized the illuminated area on the material. The geometrical arrangement of the optics was as follows. Two cylindrical lenses, A and B, of focal lengths 10cm and 3.5cm, respectively, were used. The axis of lens A was arranged horizontally and 50cm in front of the sample. The axis of lens B was placed vertically (i.e. crossed to that of lens A) and was placed about 4cm in front of the sample. Lens B focused the laser beam into a long vertical line of dimension 1.5cm x 300μm = $4.5 \times 10^{-2} cm^{-2}$. The long axis coincided with the entrance slit of the monochromator. The scattered light from the sample was collected by a high quality camera lens (focal length = 13.5 cm, f=1.8). The entrance slit of the spectrometer (about 2 cm x 400μm) was fully illuminated. This optical arrangement reduced the power density by a factor

of 5 as compared to the usual set up when only one cylindrical lens was used, i.e. for the evaluation of L_+, L_-. Hence, with the same power density, we can increase the signal by a factor of 5.

To enhance the scattering light even more, the polarization of the incident light was in the plane of incidence and the angle of incidence was set at the Brewster's angle. This reduced the reflected light intensity, hence increasing the light penetration in the crystal.

Table 13: Depletion width measurement using 5 lines of an Ar^+ lasor

Excitation Wavelength (A)	Optical Skin Depth $d_o(\lambda)$ (A)	$I^{\lambda}(LO)/I_o^{\lambda}(LO)$	Depletion Width L_s^{exp}(A)
5145	1093	0.37	256
4965	899	0.39	226
4880	816	0.43	236
4765	704	0.48	231
4579	517	0.62	253

Data were digitally recorded at the unscreened LO peak position (292 cm^{-1}). The sample dependent background (taken near 310 cm^{-1})

was subtracted from this value. The integration time per data point was 50 sec. Each experimental point was an average of 10 data points.

Listed in Table 13 is the ratio of $I^{\lambda}(LO)/I^{\lambda}_{o}(LO)$ from sample SUM5G using the 5145A, 4965A, 4880A, 4765A, 4579A Ar^{+} laser lines. Also listed are values of d_{e} (λ) taken from Ref. [105]. Therefore, by using Eq.(108) it was possible to evaluate L^{exp} at five different wavelengths. Note, from Table 13, that even though $I^{\lambda}(LO)/I^{\lambda}_{o}(LO)$ are 0.37 for 5145A and 0.62 for 4579A, the measured depletion widths are 256A and 253A respectively. This demonstrates the high degree of consistency of our approach.

Listed in Table 14 is the summary of our results for the determination on n and the depletion widths L^{exp} (averaged over the five wavelengths) for the various samples. The values of Lth displayed in Table 14 will be discussed in the next section.

Table 14: Depletion width of various <100> GaAs samples experimentally measured and theoretically correlated

SAMPLE	$n(cm^{-3})$	$L_s^{exp}(A)$	$L_s^{th}(A)$
A(CS5B)	$4.0X10^{17}$	250±25	230
B(SUM12C)	$4.5X10^{17}$	232±25	210
C(SUM5G)	$1.1X10^{18}$	240±25	230
D(BULK)	$1.3X10^{18}$	241±25	210
E(798-7C)	$2.7X10^{18}$	106±7	136
F(782-8A)	$9.0X10^{18}$	65±7	66
G(798-5G)	$10.5X10^{18}$	63±7	60

3.3.1.3 Depletion Width at Finite Temperature

To compare our experimental results with theory, care must be taken in determining whether or not the material is degenerate. For example, GaAs becomes degenerate at about $n = 1 \times 10^{18}$ cm^{-3}[106].

We present below a generalized theory of the width of the depletion region, at finite temperatures, for both degenerate and non-degenerate material[106]. Shown in Figure 40 is a schematic representation of the space charge region for n-type material, where V(x) is the electron potential in the SCR, x is the distance from the surface, V_b is the

surface band bending, (for GaAs it is approximately 0.8 eV[107]), E_F is the Fermi level, E_D is the impurity ionization energy, (for Si doped GaAs E_D is 0.002eV[106]), and V_e is the electron potential at the edge of the SCR denoted by L_s For our purposes we define the extent of the SCR as follows. From Eqs.(104) and (107), it can be seen that for $n<1 \times 10^{16}$ cm^{-3}, the positions of L_+ and LO are indistinguishable. Hence, we define the optical SCR as the region with free carrier concentration $n_o<1 \times 10^{16}$ cm^{-3}. We shall show in the following section that L_s is quite insensitive to the choice of n_o as long as this quantity is less than 1×10^{16} cm^{-3}.

Posson's equation for V(x) is

$$d^2V(x)/dx^2 = 4\pi e^2\rho(x)/\varepsilon_o \tag{109}$$

where ε_o is the static dielectric constant, and $\rho(x)$ is the net positive charge density. For non-degenerate case $\rho(x)$ is given by

$$\rho(x) = \frac{n_D}{1+2\exp\{[E_F+E_D-V(x)]/kT\}} -(2n_c/\pi)F_{\frac{1}{2}}\{[E_F-V(x)]/kT\} \tag{110}$$

and for degenerate case

$$\rho(x) = n_D-(2n_c/\pi)F_{\frac{1}{2}}\{[E_F-V(x)]/kT\} \tag{111}$$

where n_D is the donor concentration, n_c is given by[106]

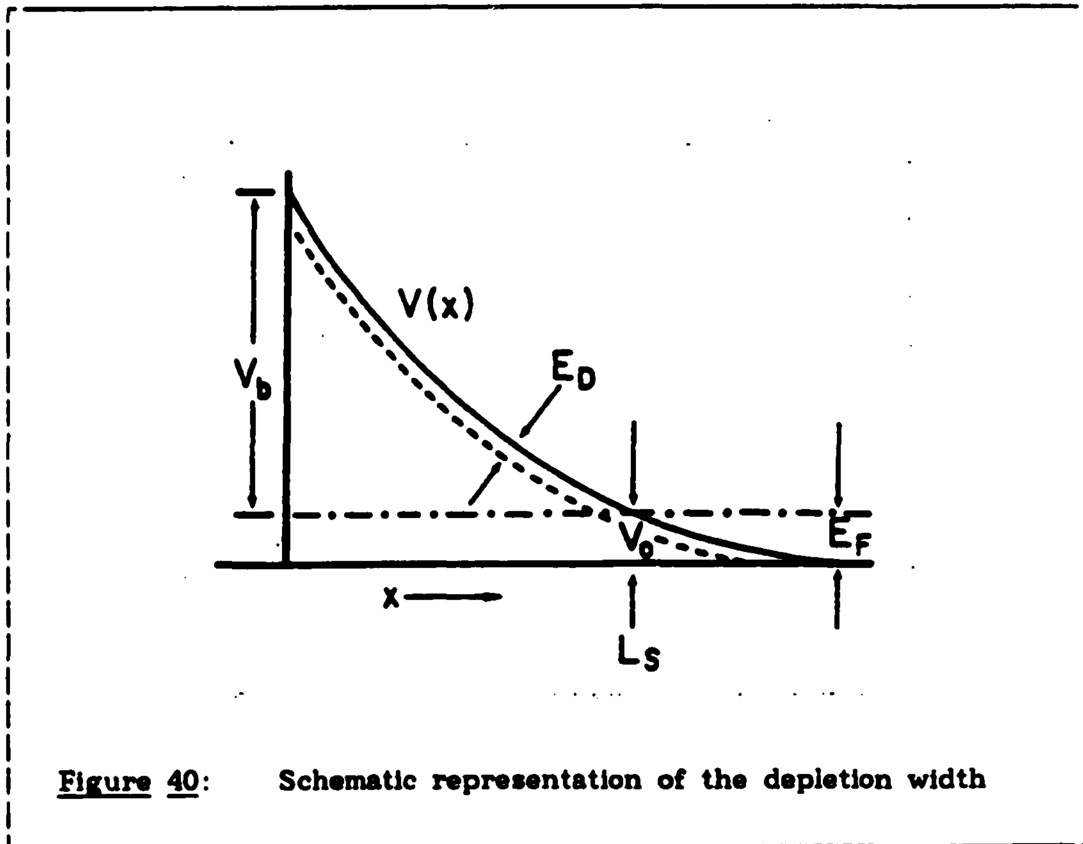

Figure 40: Schematic representation of the depletion width

$$n_c = 2(2\pi m^* kT/\hbar^2)^{3/2} \tag{112}$$

and $F_{\frac{1}{2}}(y)$ is the Fermi function

$$F_{\frac{1}{2}}(y_f) = \int_0^{\infty} y^{\frac{1}{2}}/[1+\exp(y-y_f)]dy \tag{113}$$

The boundary conditions on V(x) are

$$V(0)=V_b+E_F \tag{114}$$

$$V(\infty)=0 \tag{115}$$

$$V'(\infty)=0 \tag{116}$$

The solution is given by

$$x = L_o \int_{V(x)/V_b}^{1+E_F/V_b} dz/2\sqrt{\int_0^z \rho(\eta)d\eta} \tag{117}$$

where $L_o=(\varepsilon_o V_b/2\pi e^2 n_D)^{\frac{1}{2}}$ (118)

and $\rho(\eta)$ is the reduced charge density given by,

$$\rho(\eta)=\rho(V)/n_D \tag{119}$$

and

$$\eta=V(x)/V_b \tag{120}$$

Thus the depletion width L_s is given by

$$L_s = L_o\alpha(n_D,T) \tag{121}$$

where

$$\alpha = L_o \int_{V_0/V_b}^{1+E_F/V_b} dz/2\sqrt{\int_0^z \rho(\eta)d\eta} \tag{122}$$

As discussed above the quantity V_o can be determined by the relation,

$$n_o \leq 1\times10^{16}cm^{-3} = (2n_c/\pi)F_{\frac{1}{2}}\{[E_F-V(x)]/kT\} \tag{123}$$

Note that since the Fermi function $F_{\frac{1}{2}}$ is quite sharp even at finite temperatures the quantity V_o (and hence L_s) is quite insensitive to our choice of n_o as long as it is less than 1×10^{16} cm^{-3}.

In the case of a degenerate sample at T = 0°K, we have

$$F_{\frac{1}{2}}(y_f) = \begin{cases} (2/3)y_f^{3/2} & y_f>0 \\ 0 & y_f<0 \end{cases} \quad (124)$$

Thus using for degenerate material

$$n_D = N = (2m^*E_F)^{3/2}/3\pi^2 h^3 \quad (125)$$

and we can write

$$\rho(\eta) = \begin{cases} 1-(1-\eta V_b/E_F)^{3/2} & \eta<E_F/V_b \\ 1 & \eta<E_F/V_b \end{cases} \quad (126)$$

For the degenerate case the quantity V_o at T = 0°K can be determined to be

$$V_o = E_F$$

since $F_{\frac{1}{2}}$ is essentially a step function. It is then easy to verify that at T = 0°K the above Equations lead to the same result of Eq.(2.46) in Ref. [108].

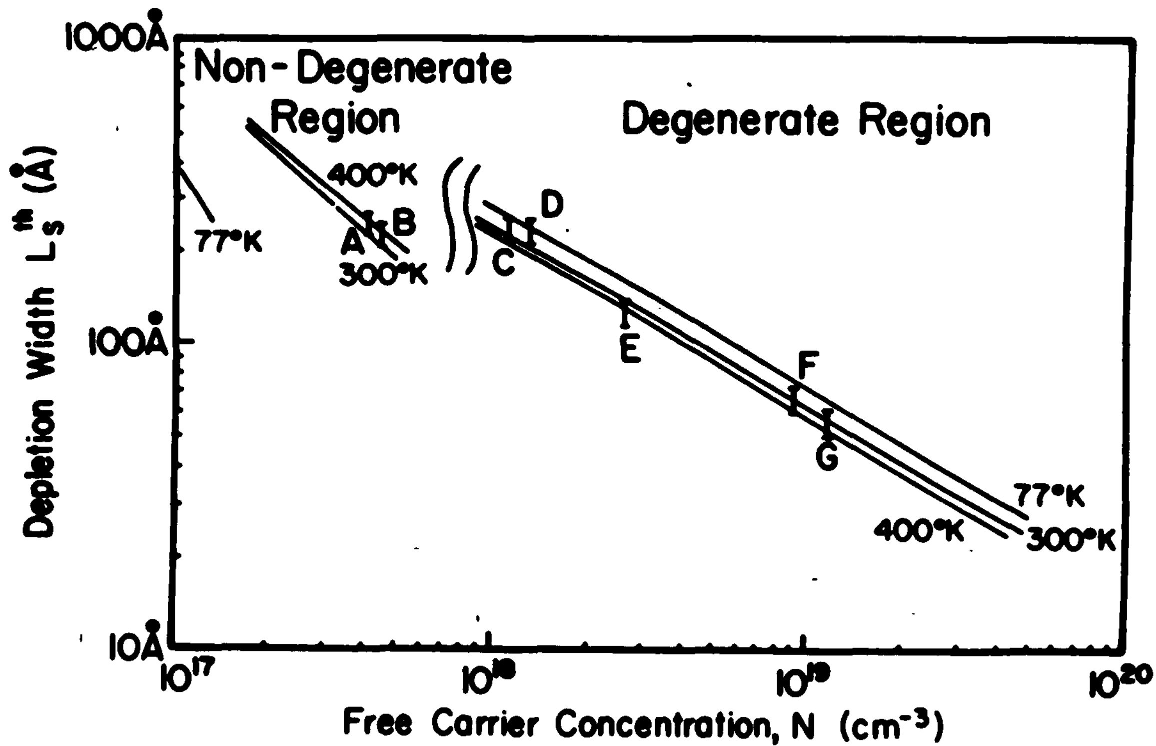

Figure 41: Depletion width as a functiiotn of free carrier concentration and temperature.. Solid lines calculated from the relevant equation in the text. Bars are the experimental values for sample A-E.

Plotted by the solid lines in Figure 41 is L^{th} as a function of carrier concentration n for the both non-degenerate case ($n<10^{18}$ cm^{-3}) and the degenerate situation ($n>10^{18}$ cm^{-3}) for three temperatures, i.e 77°K, 300°K, and 400°K. The values of Lth listed in Table 14 were taken from this figure for the corresponding values of n. Also plotted in Figure 41 are L^{exp} for th five measured samples. Table 14 and Figure 41 show that there is very good agreement between experiment and theory.

Since a specific value of E_D was used in our calculation, the curves for the non-degenerate case are only valid for Si-doped GaAs. The discontinuity in L^{th} at n about 10^{18} cm^{-3} is due to the approximation used concerning the ionization energy E_D. In a real material E_D is a function of n_D for heavy doping levels, a situation we have not taken into account.

In conclusion we have succeeded in gaining quantitative information about the widths of the space charge region from <100> n-GaAs with carrier concentrations in the range of 4 x 10^{17} cm^{-3} to 1 x 10^{19} cm^{-3} by RS from the LO phonons. We have presented a generalized theory of the depletion width for both degenerate and non-degenerate cases, at finite temperatures. The experimental results are in very good agreement with the theory. Thus, this work demonstrates that RS can be

used as a non-destructive, contactless probe of the SCR of <100> oriented zincblende-type semiconductors.

3.3.1.4 Electric Field and Impurity Induced Forbidden LO Scattering

The observation of dipole-forbidden Raman scattering (RS) by LO phonons in zincblende-type semiconductors has been reported by a number of authors [9] [92] [109]. This scattering does not follow the selection rules imposed on the Raman tensor of the Γ-point phonons due to the translational symmetry of the material. Different mechanisms may be responsible for the reduction of the crystal symmetry and hence the activation of normally forbidden RS. Such mechanisms may include electric fields (surface and/or bulk) [96] [110] [111], finite q-vectors [96] [111], impurities [112] [113], etc. Recently Menendez and Cardona have reported a study in which interference effects have been used to separate intrinsic from extrinsic (impurity-related) contributions to the forbidden scattering [112] [113].

In this section we report on investigation of the symmetry forbidden longitudinal optic (LO) phonon RS from the <100> surface of heavily doped n-GaAs:Si due to the high impurity levels and surface electric fields. Only MBE grown samples with carrier concentration $n>1x10^{18}cm^{-3}$ in Table 12 were used in this section. They are labeled as A SUM5G, B 798-7C, C 798-4D, D SUMG-2D, E 782-8A and F

798-5G. The carrier concentrations of these samples are listed in Table 12. Since GaAs is degenerate for $n>1x10^{18}cm^{-3}$ we take the impurity concentration n_i equal to the free carrier concentration, n. The measurements of forbidden scattering were made at room temperature in the backscattering geometry using the 4579A line of an Ar-ion laser. We have studied the RS for all four possible polarization configurations, i.e. $I_1[x(y,z)x]$, $I_2[x(y,y)x]$, $I_3[x(y',y')x]$ and $I_4[x(z',x')x]$, where x =<100>, y = <010>, z = <001>, y' = <011> and z' =<011>. From these measurements we have evaluated the coefficients of the electric field-and impurity- induced terms.

Shown in Figure 42 we display, by the points , the experimentally determined ratios I_2/I_1, I_3/I_1 and I_4/I_1 as a function of impurity concentration n_i for a laser excitation wavelength of 4579A. Note that as $n_i \to 0$, the ratio $I_2/I_1 \to 0$ while both I_3/I_1 and $I_4/I_1 \to 1$. We will show below that the difference between I_3/I_1 and I_4/I_1 with increasing n_i is due to an interference effect similar to that reported in Refs. [112] [113].

Several mechanisms may be responsible for the activation of normally forbidden RS. They are: linear-q terms (see Table 9), electric field induced terms (see Table 10), and impurity induced terms [112] [113].

For the linear-q terms there some evidence to indicate that for dimensions down to about 50A they are not important. For example,

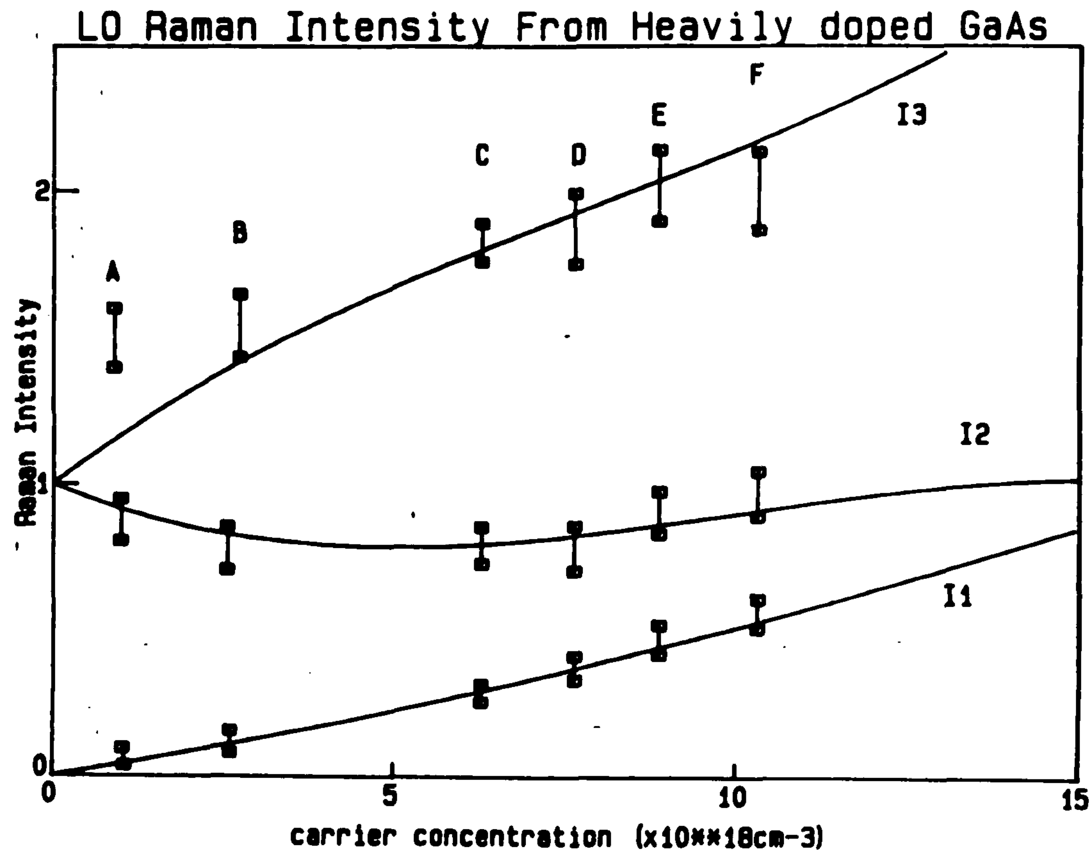

Figure 42: Electric field and impurity induced LO Raman scattering

polarization dependent Raman scattering has been performed on ion-damaged GaAs in which the average size of the undamaged region extends down to about 40A [114]. They showed that no significant symmetry forbidden transitions were observed in these samples. Thus we will neglect the linear-q terms.

The electric filed induced Raman tensors are listed in Table 10. They corresponding to the intrinsic forbidden scattering [112] [113] and must be added to the allowed Raman tensor (deformation potential, see Table 8) before squaring. In our case of LO-phonon scattering <100> with the electric field $\mathcal{E}(x)$ also along this crystallographic direction the Raman tensor can be written as:

$$\begin{vmatrix} a_1 e^{i\phi_1}\mathcal{E}(x) & 0 & 0 \\ 0 & a_2 e^{i\phi_2}\mathcal{E}(x) & d e^{i\phi_3} \\ 0 & d e^{i\phi_3} & a_2 e^{i\phi_2}\mathcal{E}(x) \end{vmatrix} \qquad (127)$$

where $a_1(a_2)$ and ϕ_1 (ϕ_2) are the coefficients of the electric field-induced term while d and ϕ_3 are related to the normally allowed atomic-deformation (AD) scattering process. Note that we have taken into account the fact that d in Table 8, a and c in Table 10 are complex. For our scattering geometry, i.e. from the <100> surface, it can be shown that only $a_2(\phi_2)$ and $d(\phi_3)$ can be observed.

The Raman tensor for impurity-induced scattering can be written as [112] [113]

$$\begin{vmatrix} 1 & 0 & 0 \\ 0 & 1 & 0 \\ 0 & 0 & 1 \end{vmatrix} ce^{i\phi_4} n^{\frac{1}{2}} \tag{128}$$

where c and ϕ_4 are the magnitude and phase, respectively, of the coefficient for this process. It has been demonstrated by Menendez and Cardona that Eqs. (127) and (128) represent independent scattering processes [112] [113]. Therefore, in order to calculate the total scattering intensity the two processes must be added after squaring, not before squaring.

From Eqs. (127) and (128) we can write expressions for the intensities of ratios the various polarization configurations:

$$I_1 = \int_0^{L_s} d^2 e^{-2\alpha(\lambda)x}\, dx \tag{129}$$

$$I_2 = \int_0^{L_s} [a_2{}^2 \mathcal{E}^2(x) + c^2 n_i] e^{-2\alpha(\lambda)x}\, dx \tag{130}$$

$$I_2 = \int_0^{L_s} [|a_2 e^{i\phi} \mathcal{E}(x) - d|^2 + c^2 n_i] e^{-2\alpha(\lambda)x}\, dx \tag{131}$$

$$I_2 = \int_0^{L_s} [|a_2 e^{i\phi} \mathcal{E}(x) + d|^2 + c^2 n_i] e^{-2\alpha(\lambda)x}\, dx \tag{132}$$

where $\phi=\phi_2-\phi_3$, is the depletion region and $\alpha(\lambda)$ is the penetration depth of the light at wavelength λ). In Eqs. (129)-(132) we have neglected the small difference in wavelength between the incident and scattered light. Expressions for L_s and $\mathcal{E}(x)$ as a function of n_i are given by Eqs(121) and (66). The quantity $\alpha(\lambda)$ is obtained from the work of Aspnes and Studna[105]. Note that Eqs. (131) and (132) exhibit an interference between the electric-field-induced and AD terms similar to that discussed in Refs. [112] and [113].

The solid lines in Figure 42 are a least squares fit of Eqs. (129)-(132) to the experimental points. From such an analysis we can evaluate

$$a_2/d=(4.8\pm0.2)\times10^{-7}\ \text{cm/V} \tag{133}$$

$$c^2/d^2=(2.1\pm0.2)\times10^{-20}\ \text{cm}^3 \tag{134}$$

$$\phi=58\pm2^{\circ} \tag{135}$$

Grimsdich et al have measured and calculated the quantity d in GaAs as a function of λ[115]. At 4579A Ref.[115] reports d=100A Thus we can write from 4579A

$$|a_2|=4.8\times10^{-5}\text{cm/v (A)}^2 \tag{136}$$

$$|c|^2=(2.1\pm0.7)\times10^{-16}\text{cm}^3(\text{A})^4 \tag{137}$$

This is the first evaluation of $|a_2|$ and ϕ, the relative phase angle between a_2 and d. Also this is the first determination of |C| in this wavelength region.

In Ref.[113] a value of $c^2\approx1.5\times10^{-12}A^4cm^3$ for GaAs is presented corresponding to the wavelength of $E_0+\Delta_0$ resonance. Our value of $C^2\approx2.1\times10^{-16}$ A^4cm^3 is considerable smaller since we are far from any interband resonance.

3.3.2 Polish-Induced Surface Strain

In diamond and zincblende-type semiconductors surface damage induced by processing procedures such as polishing is an area of considerable technological interest. Polish-induced damage has been studied by various methods [116] including optical techniques such as photoluminescence,[117] reflectance,[118] [119] [120] absorption,[121] and Raman spectroscopy (RS)[122] [123] [124]. RS is a particularly useful tool for a number of reasons. The influence on the Raman spectrum of

damage-induced perturbations such as strain [96] [125] and disorder[114] (which produce different effects) is well understood. Nondestructive depth profiling can be performed by using various laser lines. In zincblende-type materials the longitudinal optical (LO) phonon is a singlet; hence certain complications which occur in electronic transition spectroscopies are avoided such as strain-induced interband and interband splittings.[126]

In this section we report an investigation of the effects of polish-induced strain on the line shape of LO phonon RS of <100> and <111> InP and GaAs. Measurements were made at room temperature in the backscattering geometry from the <100> and <111> surfaces of GaAs and InP single crystals polished under various conditions of grit size and polish time. The Raman source was an Ar^+ laser with outputs at 5145, 5017, 4965, 4880, 4765, 4579 A. A line focus (300μm x 3mm) was used in order to avoid heating effects. The laser power was 300 mW except at 4579 and 5017 A, in which case it was 130 mW. For the <100> surface, the cross polarization configuration [x(y,z)x] was used to reduce the Rayleigh scattering from the rough surface, where x,y,z denote [100], [010], [001], respectively. For the <111> surface, since the cross configuration is forbidden, the scattered light was not analyzed. No significant difference in line shape was found between different

polarization configurations. It was sometimes not possible to obtain meaningful data at all the above wavelengths, because of the influence of plasma lines on the weak Raman signal of the damaged sample~

Polishing was performed using a Beuhler Model AB Low Speed Polisher (Buehler Ltd., Evanston, III. 8-in. wheel) with a Politex Supreme 125 polishing pad (Geosciences Corporation, Stamford, Conn.). Samples were mounted on a holder which was placed in a Buehler Model AB Whirliment attachment, making it possible to rotate the sample holder in a direction opposite to that of the polishing wheel. Typical speeds were 5 rev/s for the polishing wheel and 0.5 revs for the Whirliment attachment. Pressures due to the sample holders were 1.12×10^5 and 1.47×10^4 dyn/cm^2 for GaAs and InP, respectively.

Both the GaAs and InP samples employed were semi-insulating in order to avoid free carrier effects[102]. Samples were obtained to <100> or<111> within 1° using X-ray Laue backscattering. The undamaged surfaces were prepared by 1μm, and 0.05μm alumina powder polishing for 60 minutes, followed by 1:4 Syton (Monsanto Corporation, distributed by Remet Corporation, Chadwick, N.Y. 13319.) in deionized water polish for 60 minutes and finally a 0.1% Br in methanol chemo-mechanical polish for 5 minutes. Separate pads were used for the different polishing conditions. The concentrations of Syton in

water and Br in methanol were found to be quite critical. The undamaged surfaces had no observable scratches or pits under a microscope (magnification = 16).

The quality of the <100> surface also was examined by RS. Transverse optical (TO) phonon scattering is normally forbidden in backscattering from the <100> surface.[8] [10]. It can be shown that neither surface electric field or linear-q effects can activate the TO phonon from this face (see Table 9 Table 10). However, this symmetry forbidden-TO mode has been observed by many workers in <100> backscattering [8][10]. Several investigators have discussed the origins of this mode [10] [127] [128] including a very detailed analysis by Biellmann et al. [128]. The amplitude of the symmetry forbidden-TO in relation to the symmetry allowed-LO phonon can be used as a measure of crystal quality. The quality of the undamaged surface is important since it serves as a standard for the unstrained LO position and linewidth. We measured the ratio of TO/LO in a true-backscattering geometry and found it to be less than 0.2% for undamaged surface.

Damage was induced on an <u>undamaged</u> <u>surface</u> by slurries made from 0.5µm, 0.3µm, or 1µm alumina polishing powders for various time periods. Separate pads were used for the different particle sizes.

Shown in Figure 43a is the RS in the region of the LO phonon for undamaged <100> InP using the 5145 A line (spectrum A) and material polished with 0.05μm grit for 5 ~in. using the 5145, 4965, 4880 and 4579 A excitation lines (labeled B,C,D,E and F, respectively). The undamaged RS is a fairly sharp, symmetrical peak centered at 345.6 cm^{-1}. Spectrum B has a relatively sharp feature at about 848 cm^{-1} and a broad shoulder at about 355 cm^{-1}. As the penetration depth of the light decreases the amplitude of the high frequency shoulder grows relative to the low-frequency feature. The amplitude of the RS of the damaged material were considerably less than the undamaged sample although the integrated intensities remained approximately constant.

Plotted in Figure 43b are the results for <100> GaAs. Spectrum A is the undamaged material taken with 5145 A while spectra B-F are for the case of 0.3μm grit polish for 60 min. using 5145, 5017, 4880, 4765 and 4579 A, respectively. In this case the high-frequency shoulder in spectrum B has become the dominant feature at the shortest wavelength. As will be demonstrated below the two features in the spectra of damaged InP and GaAs do not arise from two separate peaks but are the consequences of the convolution of the skin depth of the damage-induced strain and the optical penetration depth for the various wavelengths.

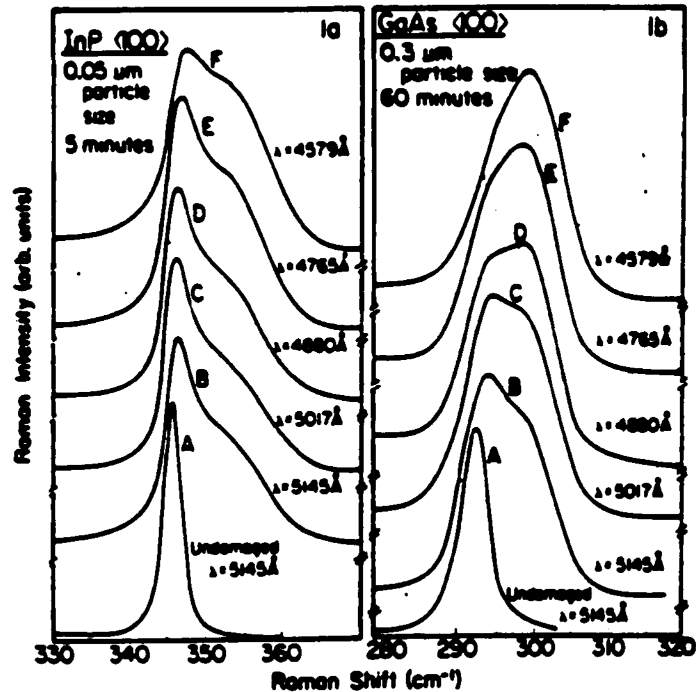

Figure 43: Raman scattering from polished <100> GaAs and InP. a)InP: undamaged surface at 5145A (spectrum A) and material damaged with 0.05μm particle size for 5 min. at 5145, 5017, 4880, 4765 and 4579 A (spectra B-F). b)GaAs: undamaged surface at 5145A (spectrum A) and material damaged with 0.3μm particle size for 60 min. at 5145, 5017, 4880, 4765 and 4579 A (spectra B-F).

Shown in Figure 44a is the RS in the region of the LO phonon for undamaged <111> InP using the 5145 A line (spectrum A) and material polished with 0.,05μm grit for 10 minutes using the 5145, 4880, 4579 A

excitation lines (labelled B,C,D, respectively). For the sake of clarity we have not plotted the spectra for all wavelengths since there are no major differences between them. The <111> and <100> [see Figure 44(a)] undamaged RS are identical in terms of peak position and linewidth. However, for the damage conditions, the RS from the <111> surface are quite different from the <100> case. The relatively sharp feature at about 348cm^{-1}, which appeared in the RS from the <100> face [see Figure 43a], is not seen. The broadening is fairly symmetrical, and peaked at about 346.5 - 347.5 cm^{-1}. As the penetration depth of the light decreases, the linewidth increases and the peak position shifts to the blue.

The RS spectra in the region of the LO phonon for undamaged and damaged <111> GaAs are displayed in Figure 44b. As for InP the undamaged spectra for <111> and <100> surfaces are identical. Also for GaAs the damaged spectra are symmetrically broadened; with decreasing wavelength the RS broaden and shift to the blue, although not as much as for InP [see Figure 44(a)].

The measured RS shift and linewidth for various polishing conditions from the <111> InP and GaAs surfaces versus different penetration depths, d_o, of the Ar^+ laser lines [105]. are plotted in Figure 45a and Figure 45b. We find for <111> InP and GaAs damaged with 0.3μm grit

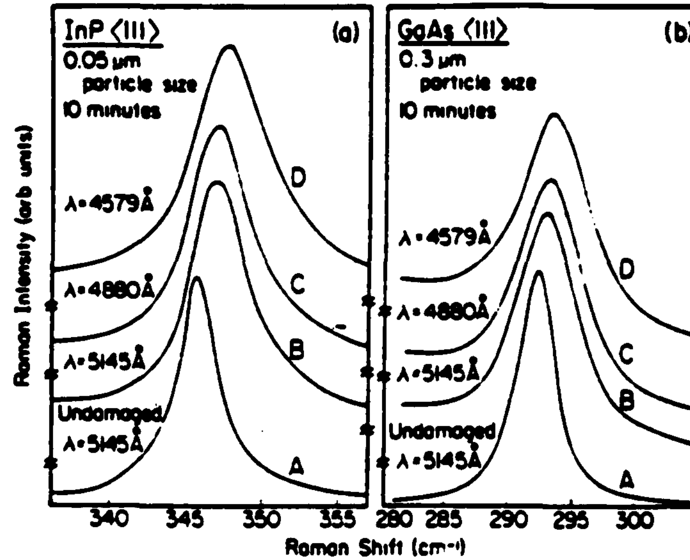

Figure 44: Raman scattering from polished <111> GaAs and InP. a)InP: undamaged surface at 5145A (spectrum A) and material damaged with 0.05μm particle size for 10 min. at 5145, 4880, and 4579 A (spectra B-D). b)GaAs: undamaged surface at 5145A (spectrum A) and material damaged with 0.3μm particle size for 10 min. at 5145, 4880, and 4579 A (spectra B-D).

for 60 minutes, the RS shift and phonon linewidth do not change with different d_o. However, for the 0.05μm grit size, the RS shift and linewidth do increase considerably with decreasing light penetration

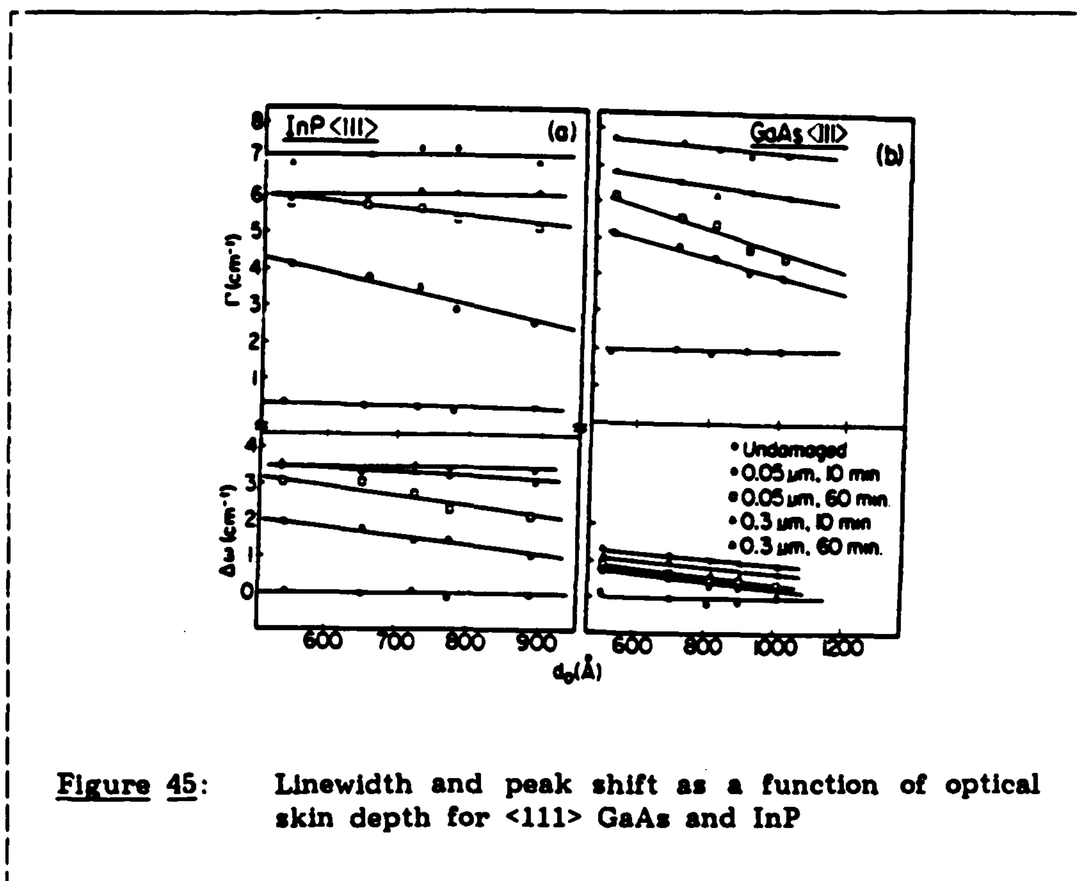

Figure 45: Linewidth and peak shift as a function of optical skin depth for <111> GaAs and InP

depth. We have also found that for the undamaged surfaces, the RS shift and linewidth are constant with d_o, demonstrating that by proper mechanical and chemical polishing, a strain-free surface can be achieved.

The above results can be accounted for on the basis of the following considerations. Polish induces strain at the surface of the material

thus producing a shift in the LO frequency from its unstrained value. [96]. [124] [125] This damaged-induced strain (and hence RS shift) diminishes as a function of depth into the sample. In addition the light intensity decays from the sample surface. The observed RS signal is then the convolution of the depth dependence of the LO frequency and the optical skin skin depth of the light. Assuming an exponential depth dependence for the Raman frequency, $\omega(x)$, (and hence strain) we can write:

$$\omega(x)=\omega_o+\Delta\omega \exp(-x/d_s) \tag{138}$$

where x is the distance from the surface, ω_o is the unperturbed frequency, $\Delta\omega$ is the shift due to surface strain, and d_s is the skin depth of the strain. Thus the Raman intensity $I(\omega)$ is given by

$$I(\omega) = \int_0^\infty dx\ L[\omega-\omega(x)]\ \exp(-2x/d_o) \tag{139}$$

where d_o is the optical skin depth and $L(\omega)$ is a line shape factor which is a convolution of the Lorentzian line shape of the RS and the instrumental transfer function. We have neglected the small differences in the optical skin depth for the incident and scattered radiation. For

simplicity we have assumed a triangular instrumental transfer function $T(\xi)$ with full width at half-maxima of Γ_I. Thus $L(\omega)$ can be written as

$$L(\omega) = \int_{-\infty}^{\infty} d\xi \; (\Gamma/2\pi) T(\xi) / [(\omega-\xi)^2 - (\Gamma/2)^2] \tag{140}$$

where Γ is the linewidth of the RS. Above equation can be solved to yield the analytical form:

$$L(\omega) = (\Gamma/2\pi\Gamma_I^{\,2})[R(\omega+\Gamma_I)+R(\omega-\Gamma_I)-2R(\omega)] \tag{141}$$

where

$$R(\omega)=(2\omega/\Gamma)\mathrm{arctg}(2\omega/\Gamma)-\tfrac{1}{2}\ln[(2\omega/\Gamma)^2+1] \tag{142}$$

It is also possible to take into account any inhomogeneous strain in the plane perpendicular to the polishing direction (for a given value of depth). This can be done by increasing the broadening parameter, Γ, from its intrinsic value (2.4 cm^{-1} for GaAs and 1.2 cm^{-1} for InP) and assuming a depth dependence similar to that of the frequency shift,

$$\Gamma(x)=\Gamma_o+\Delta\Gamma \; \exp(-x/d_s) \tag{143}$$

where Γ_o is the intrinsic value and $\Delta\Gamma$ takes into account the inhomogeneous broadening.

In order to correlate the RS peak shift $\Delta\omega$ with surface strain we assume that the polishing produces a two-dimensional strain in the plane perpendicular to the polishing direction. For the <100> case the quantity $\Delta\omega$ is related to the strain S by [96] [125]

$$\left(\frac{\Delta\omega}{\omega_0}\right)_{100} = \frac{(q - \lambda_{100}\, p)}{\omega_0^2} \cdot S = K_{100} S \tag{144}$$

where

$$\lambda_{100} = C_{12}/C_{11} \tag{145}$$

while for the <111> situation it can be shown that

$$\left(\frac{\Delta\omega}{\omega_0}\right)_{111} = \frac{(p+2q)(2-\lambda_{111})-4r(1+\lambda_{111})}{6\omega_0^2} \cdot S = K_{111} S \tag{146}$$

and

$$\lambda_{111}=2(C_{11}+2C_{12}-2C_{44})/(C_{11}+2C_{12}+2C_{44}) \quad (147)$$

where ω_o is the unperturbed Raman frequency, C_{11}, C_{12} and C_{44} are elastic stiffness constants and p,q and r are coefficients which describe the strain-induced shift of the optic phonon. For GaAs K_{100} = 1.5 and K_{III} = -0.7. For InP p, q and r have no been determined; however, since these parameters do not vary much for the III-V materials[125] [96] we take the GaAs values for InP and hence K_{100} = 1.3 and K_{111} = -0.80.

Shown in Figure 46a is a least-squares fit to the spectra at 5145 A and 4765 A of <100> InP damaged with 0.05µm grit for 60 minutes. The adjustable parameters were $\Delta\omega$ and d_s. We have taken ω_o = 345.6 cm^{-1} and Γ = 1.2 cm^{-1}; from the slit settings Γ_I = 2.4 cm^{-1}. Values of d_o were taken from Ref.[105]. There is excellent agreement between theory and experiment at both wavelengths. It is found that $\Delta\omega$ = 12.3 cm^{-1} and d_s = 204 A for 5145 A and $\Delta\omega$ = 12.3 cm^{-1} and d_s = 186 A for 4765 A, demonstrating the high degree of consistency of our approach. Comparable values were obtained for the other wavelengths. Listed in Table 15 are summaries of the results for InP (averaged over the different wavelengths) for the various polishing conditions.

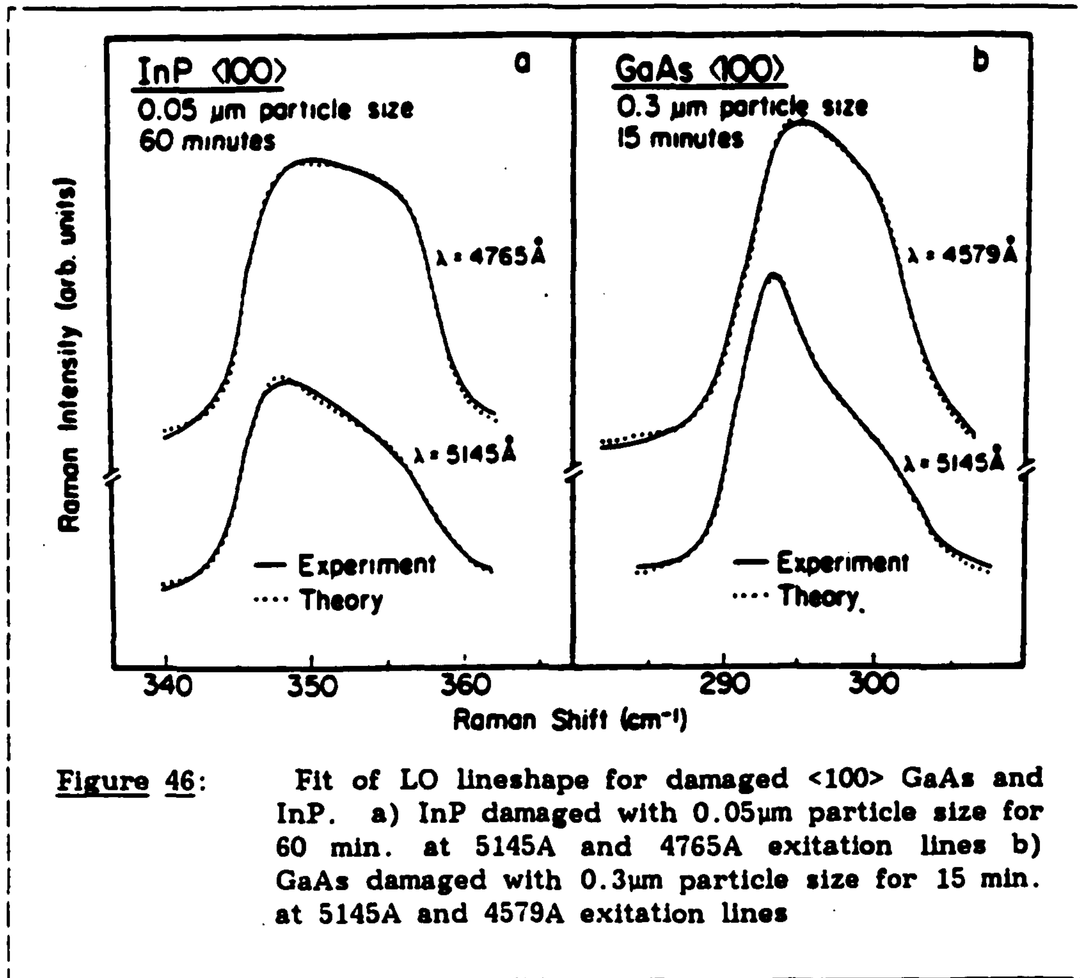

Figure 46: Fit of LO lineshape for damaged <100> GaAs and InP. a) InP damaged with 0.05μm particle size for 60 min. at 5145A and 4765A exitation lines b) GaAs damaged with 0.3μm particle size for 15 min. at 5145A and 4579A exitation lines

In Figure 46b are plotted experiment and theory for <100> GaAs at 5145 and 4579 A damaged with 0.3μm grit for 15 min. using ω_o =292.1 cm^{-1},Γ = 2.4 cm^{-1}, and Γ_I = 2.4 cm^{-1}. We find for 5145 A that$\Delta\omega$ = 10.9 cm^{-1} and d_s = 260 A while for 4579 A $\Delta\omega$ = 10.1 cm^{-1} and d_s = 230 A, again demonstrating consistency. Values of $\Delta\omega$ and d_s (averaged

over the wavelengths) for GaAs for different polishing conditions are listed in Table 15.

We have also introduced an inhomogeneous strain for the <100> case for both InP and GaAs. We find that increasing $\Delta\Gamma$ to 3 cm^{-1} had little effect on the quality of the fits in Figure 46a and Figure 46b; further increases, however, result in a significant deviation in the correlation between theory and experiment. Therefore, we conclude that the inhomogeneous strain component $\Delta\Gamma_I < 3$ cm^{-1} for the <100> case. This is significantly less than the homogeneous shift $\Delta\omega$ which is 9-12 cm^{-1} (see Table 15).

The interpretation of the experimental results for the <111> case are somewhat different from that for the <100> situation. By using only Eqs. (138)-(139), i.e. no homogeneous broadening, we were not able to get a good fit to the experimental data. We find that for the <111> surface it is necessary to introduce Eq. (143): for this case inhomogeneous broadening is an important effect, as found in the previous RS study[122]. In contrast to the <100> case it is difficult to get meaningful data from just the spectrum at a single wavelength since variations in d_s and $\Delta\Gamma$ produce similar effects on the theoretical fit. Therefore, we obtained values of $\Delta\omega$, $\Delta\Gamma$ and d_s for the different polishing conditions by performing a self-consistent least square fit of Eqs.

Table 15: experimental results for various polishing conditions on <100> suurface

Material	Particle size (μm)	Time (min)	Δω (cm^{-1})	ΔΓ (cm^{-1})	d_s (cm^{-1})
	0.05	5	+12.6±0.5	<3.0	190±25
InP	0.05	60	+12.1±0.5	<3.0	300±40
	0.3	30	+12.5±0.5	<3.0	440±50
	0.05	60	+9.1±0.5	<3.0	200±25
GaAs	0.3	15	+10.5±0.5	<3.0	250±40
	0.3	60	+11.4±0.5	<3.0	360±50
	1	2	+10.4±0.5	<3.0	530±50

(138)-(139) to all five spectra at different wavelengths, i.e., 5145, 4965, 4880, 4765 and 4579 A. The resultant numbers are listed in Table 16.

Comparing Table 15 and Table 16, we find that for the <111> surfaces, the compressive surface strain is less than that in the <100> case. The dominant strain is inhomogeneous. The depth of damage-induced strain is much deeper than that of the <100> for corresponding polishing conditions.

Table 16: Experimental results for various polishing conditions on <111> suurface

Material	Particle size (μm)	Time (min)	$\Delta\omega$ (cm^{-1})	$\Delta\Gamma$ (cm^{-1})	d_s (cm^{-1})
InP	0.05	10	+2.8±1.0	4.8±1.0	350±100
	0.05	60	+3.3±1.0	7.0±1.0	1100±200
	0.3	10	+3.6±1.0	6.0±1.0	3400±500
	0.3	60	+3.6±1.0	7.0±1.0	4500±500
GaAs	0.05	60	+1.3±0.5	6.5±1.0	240±100
	0.3	15	+1.5±0.5	7.3±1.0	440±100
	0.3	60	+1.0±0.5	5.5±1.0	1200±200
	1	2	+1.4±0.5	6.3±1.0	1800±200

From the sign and magnitude of $\Delta\omega$ in Table 15 and Table 16 we find a compressive surface strain of about 2.2% for <100> GaAs, 2.6% for <100> InP, 0.6% for <111> GaAs and 1.2% for <111> InP. With regard to the inhomogeneous strain (i.e., $\Delta\Gamma/2$) it is less than 0.3% for the <100> surface while it is about 1.4% for the <111> surface. For the <111> case the strain skin depth is of order the particle size while for the <100> situation it is generally less.

We have also considered the effects on the LO phonon line shape of other perturbations such as (a) disorder (b) temperature gradient effects and (c) free carrier interactions (coupled plasmon-LO modes) P. Disorder lowers the lattice symmetry and relaxes the q=0 selection rule of Raman scattering, i.e. some scattering processes which are normally forbidden in the undamaged crystal can be activated. [123] [10] It has been shown that the influence of this perturbation on the LO phonon is to red shift the peak position and asymmetrically (low-frequency side) broaden the line shape. [114] Introducing such an effect into our equations yields a poorer fit. In addition, we have measured the RS below the LO phonon region and find little disorder-activated effects. [123]. Thus the disorder-activated component of the damage corresponds to a correlation length (as defined in Ref. [114]) of greater than 300 A. We concluded, as Evans and Ushioda did, that the effects of disorder are relatively minor.

With regard to temperature gradients, it has also been shown that the influence of this perturbation is to red shift the LO phonon frequency and asymmetrically (low-frequency side) broaden the line shape. [129] Thus, it also contradicts our experimental results. Since we used the same power for both the damaged and undamaged surfaces there appears to be no physical reason why the temperature gradient is greater in the damaged case than it is in the undamaged situation.

Care must be taken in determining as to whether or not our observed blue shift (of about 5-10 cm^{-1}) is due to the introduction of free carriers by the polish damage. It is well known that the L_+ component of the coupled plasmon-LO phonon mode is at a higher frequency than that of the uncoupled LO peak[102]. If the scattering volume near the polished sample surface contains a free carrier concentration of n = 1.0×10^{17} cm^{-3}, then L_+ will lie about 10 cm^{-1} higher than LO. Thus, it might be responsible for the high frequency bump in the damaged spectra of Figure 43a and Figure 43b. It has been observed that one of the factors altering the surface carrier density is dopant redistribution induced by gettering to surface defects.[130] It is reasonable to assume that such gettering decreases with increasing distance from the damaged surface. However, RS does not determine the actual dopant density, but only measures the free carrier concentration. The depletion width for n = 1×10^{17} cm^{-3} is about 1000 A. Thus most of the pileup dopants are contained within the space-charge depletion zone. RS would not detect any of this effect within this region. It should be pointed out that anealing would not resolve this puzzle, since some previous studies have shown that anealing reduces both surface free carriers[102] as well as surface strain.[122]

This ambiguity can be resolved by examining the TO phonon since this mode does not couple to the free carriers [102] [8]. We have measured TO phonon RS from the <111> damaged surfaces and observed a blue shift from its unstrained value. However, because of the complexities of the strain-dependence of the TO phonon (it is a doublet) [124] [125], we were not able to do a detailed fit. The observed blue shift is consistent with the strain-induced shift of the LO mode and hence we deduce that free-carriers are not a factor in our analysis.

For the <111> case our results are consistent with those of other investigators, including Evans and Ushioda. As shown in Table 16 we find that the strain skin depth for both materials is approximately equal to the polishing particle size (for GaAs d_s is somewhat smaller than the particle size). Also, for both semiconductors d_s becomes larger with increasing polishing time. The phonon line broadening is caused primarily by the inhomogeneous strain distribution (both compressive and tensile) in the polishing plane, while the shift of the RS peak is due to the mean compressive surface strain.

For the <100> case our findings are somewhat different from previous studies [116] [117] [119] [122] [131]. Other investigations have concluded that the polishing induced damage goes as deep as the particle size, while we find that the strain penetration depth for the <100>

surface is considerably less than the particle size, particularly in the o.3μm and 1μm cases (see Table 15). However, it should be pointed out that other workers did not examine the <100> orientation but reported on other faces, i.e., <110> in Ref. [122], <111> in Ref. [131], etc. Thus, it is somewhat difficult to make detailed comparisons. Also, it should be noted that some of the earlier studies were not 'non-destructive' but obtained their findings by etching away controlled amounts of material from the surface. Compared with the <111> case, the strain in the <100> surface is relatively homogeneous. The phonon line broadening is primarily due to the exponential decay of homegeneous strain from surface.

At the present time we do not understand the difference in the results from the two orientations. We believe it may be related to the nature of the bonding at these two different surfaces. Since <100> is of considerable technological interest, our result should serve to stimulate more detail work on this surface.

In conclusion we have studied the effects of polishing on the LO phonon Raman spectra from <100> and <111> GaAs and InP; non-destructive depth profiling was performed by using various laser lines. The details of the line shape can be quantitatively accounted for by a theory based on the convolution of the optical and strain skin depths.

We find that the strains for both surfaces are compressive; the average compressive surface strain in 2-3% for the <100> surface and 0.6-1.2% for the <111> surface. The surface strain in <100> is fairly homogeneous (less than 0.3%), while that in <111> surface is significantly more inhomogeneous (about 1.4%). The strain skin depth is as deep as the particle size for <111> surface; while it is substantially smaller than the particle size for <100> surface.

Chapter IV

SUMMARY AND CONCLUSIONS

This thesis is an investigation of microstructural geometries in semiconductor using modulation spectroscopy and Raman scattering. Samples used in this study included AlAs/GaAs superlattices $GaAl_{1-x}As$/GaAs superlattices (X<0.3), GaAs nipi superlattices, InP/ITO system, heavily doped n-type GaAs (MBE grown $n=4x10^{17}-1.1x10^{19}$) and bulk intrinsic GaAs and InP.

We have demonstrated that electroreflectance especially photoreflectance is an extremely powerful tool for investigating microstructural geometries. We have developed a new servo mechanism for Photoreflectance by using a variable neutral density filter, which has considerable advantage over previously used one.

We demonstrated for the first time that Photoreflectance spectra can be fit by a third derivative function lineshape, thus making it possible to precisely determine energy positions and resolve hidden structures. This result greatly enhanced the usefulness of PR to characterize microstructural geometries and stimulated a lot of other scientific interesting.

Using Photoreflectance at room temperature we have evaluated the topographical variations in quantum level transitions of a GaAs/ $Ga_{0.76}Al_{0.24}As$ multiple quantum well(200A/150A) due to changes in barrier height and quantum well width. The spatial resolution of the measurement was about 100μm. We can detect the barrier height changes of several millielectron volts and variation in well as small as 2A.

The Photoreflectance spectra of several GaAs/AlAs superlattices have been measured at 300K and 77k using monochromator as a secondary beam, thus enabling us to study the wavelength dependence of the PR. The result showed that there were more than one mechanism in superlattices, in contrast to bulk material. Also nondestructive depth profiling has been demonstrated by this result.

We have investigated the PR spectra of GaAs/$Ga_{0.83}Al_{0.17}As$ superlattices. In addition of the allowed transitions, we have clearly observed, for the first time at room temperature, the forbidden features 12H, 13H,and 21H. the observed intensities appeared to be in good agree with a theory based on valence band mixing effect.

We have measure the room temperature PR spectra from GaAs doping superlattices with substantially different periodicities. The small period sample exhibited a number of features corresponding to transitions between quantized electron and hole states. The thick period sample

exhibited Franz-keldysh oscillations. The PR spectra for both samples exhibited strong dependence on the pump power and pump chopping frequency, which is due to the extremely long life time of free carriers in nipi structures. The dependence of PR on the pump chopping frequency is a measure of the recombination lifetime.

The Franz-keldysh theory for modulation spectroscopy has been generalized to include both dc and ac field. We demonstrated, both theoretically and experimentally, that if $E_{ac}/E_{dc}<0.2$ then the Franz-keldysh oscillation is determined by the dc field not by the ac field. Ac field only smears out the higher order oscillations. According to this result photoreflectance under small modulation pump intensity can be used as a contactless method to detect the surface electric field.

We have succeeded in gaining quantitative information about the widths of the space charge region from <100> n-GaAs with carrier concentrations in the range of 4×10^{17} cm^{-3} to 1×10^{19} cm^{-3} by RS from the LO phonons. We have presented a generalized theory of the depletion width for both degenerate and non-degenerate cases, at finite temperatures. The experimental results are in very good agreement with the theory. Thus RS can be used as a non-destructive, contactless probe of the SCR of <100> oriented zincblende-type semiconductors.

The effects of polishing on the LO phonon Raman spectra from <100> and <111> GaAs and InP have been studied in detail. Non-destructive depth profiling was performed by using various laser lines. The details of the line shape can be quantitatively accounted for by a theory based on the convolution of the optical and strain skin depths. We find that the strains for both surfaces are compressive; the average compressive surface strain is 2-3% for the <100> surface and 0.6-1.2% for the <111> surface. The surface strain in <100> is fairly homogeneous (less than 0.3%) , while that in <111> surface is significantly more inhomogeneous (about 1.4%). The strain skin depth is as deep as the particle size for <111> surface; while it is substantially smaller than the particle size for <100> surface.

<u>In conclusion this study can be summarized as follows</u>:

1. Modulation spectroscopy, especially photoreflectance is a powerful tool to investigate and characterize the microstructural geometries. Both topographic and depth studies can be carried out by this technique.

2. Normalized Photoreflectance spectra without introducing false signal can been obtained by using a variable density filter.

3. Fit to the third derivative lineshape enables us to determine the energy of the quantized levers within a few millelectron volts at room temperature.

4. Forbidden transitions clearly observed at room temperature is a strong support to the valence band mixing theory.

5. The periods of the Franz-Keldysh oscill^^tions in modulation spectrum are dependent on dc field not on ac field, thus providing a direct optical measurement of the built-in electric field by a contactless way.

6. Photoreflectance spectra from small period nipi samples exhibits transitions between quantized hole and electron states, while that from thick period samples exhibits Franz-Keldysh oscillations.

7. The dependence of PR on chopping frequency can be used to measure the recombination lifetime of carriers in nipi structures.

8. Raman scattering is demonstrated to be another powerful technique to characterize the microstructural geometries. It has been employed to determine the carrier concentration and depletion width for heavily doped III-V semiconductors.

9. Electric field induced Raman tensor (both amplitude and phase) and impurity induced Raman tensor have been determined for <100> GaAs at 2.7eV

10. The effect of polishing on LO Raman spectra lineshapes can be quantitatively accounted for by a model based on the convolution

of penetration depth of light and the skin depth of the polish induced strain.

Bibliography

1. Y. Uemura, J. Phys. Soc. Japan 49, Suppl. A., 1309 (1980)
2. M. Cardona, Modulational Spectroscopy, (Acadmic Press, N. Y., 1969) and references therein.
3. Semiconductors and Semimetals, Vol. 9 ed by R. K. Willardson and A. C. Beer (Academic Press, N. Y., 1972)
4. Proc. of the First Int. Conf. on Modulation Spectroscopy, published in Surface Science, Vol. 37, (1973)
5. Y. Hamakawa and T. Nishino in Optical Properties of Solids: NewDevelopments,ed, by B. O. Seraphin (North Holland, N. Y., 1976) p.225
6. D. E. Aspens in Handbook on semiconductors, vol 2, ed by M. Balkanski (North Holland, N. Y. 1980) p.109 and reference therein.
7. F. H. Pollak, in Proceeding of the Society of Photo OpticalInstrumentation Enginerrs (SPIE, Bellingham, 1981) 276, 142 (1981 and references therein

8. W.Hayes and R. London, Scattering of light by crystal, (Jonh Willey, N. Y., 1978) and reference therein

9. Light Scattering in solids, Vol. 1 ed by M, Cardona, Vols 2-4 ed by M.Cardona and G. Guntherodt (Springer Verlag, New York) and reference therein

10. R. Tsu, in Proceedings of the Society of Photo-optical Instrumentation Engineers. SPIE, Bellingham. 1981) 276, 78, 1981 and references therein.

11. F. H. Pollak and R. Tsu in Proceedings of the Society of Photo-optical Instrumentation Engineers (SPIE, Bellingham, 1984) 452, 26 (1984) and reference therein

12. E. E. Mendez, L.L. Chang, G. Landgren, R. Ludeke, L. Esaki and F.H. Pollak, Phys. Rev. Letts. 46, 1230 (1981).

13. M. Erman, J.B. Theeten, P. Frijlink, S. Gaillard, F.J. Hia and C. Alibert, J. Appl. Phys. 56, 3241 (1984).

14. O. J. Glembocki, B.V. Shanabrook. N. Bottka. W.T. Beard and J. Comas, Appl. Phys. Letts. 46, 970 (1985)

15. O. J. Glembocki, B.V. Shanabrook, N. Bottka, W.T. Beard and J. Comas, Proceedings of Society of Photo-Optical Instrumentation Engineers (SPIE, Bellingham, 1985) 524, 86 (1985).

16. J. N. Schulman and Y. C. chang, Phys. Rev. B24, 4445 (1981)

17. M. Gal, J. S. Yuan, J. M. Viner, P. C. Taylor and G. B. Stringfellow Phys. Rev. B33. 3310 (1986)

18. N. Bottka in Proce‑‑ings of the Society of Photo-opticalInstrumentation Engineers, (SPIE, Bellingham, 1981) 2?6, 157 (1981)

19. M. Tomkiewicz, W. Siripala, R. Tenne, J. Electrochem. Soc. 131, 736 (1984)

20. F. H. Pollak, in Proceedings of the Symposia on Photoelectre-chemical Processes and Measurement techniques for Photoelectro-chemical SolarCells, ed by W. L. Wallace, Electrochemical Society Proceedings 82-3, 608 (1982)

21. R. Sacks and H. shen Appl. Phys. Lett. 47, 15 (1985)

22. L. Esaki in Proceedings of the 17th International Conf. on the Physics ofSemiconductors, Berkeley, 1984 , ed by J. D. Chodi and W. A. Harrison (springer Verlag, N. Y., 1985) p. 473.

23. L. Esaki in Symposium on Recent Topics in Semiconductor Phys-ics, ed. by H. Kamimurs and Y. Toyozowe (World Scientific, Philadelphia, 1982) P. 1.

24. K. Ploog and G. H. Dohler, Advances in Physics32, 285 (1983)

25. R. Dingle, Advances in Solid State Physics Vol.XV, ed. by H. J. Quiesser (Braunschweig: Pergamon-Vierwag, 1975) P.21, ibid Festkorperprobleme 15, 21 (1975)

26. W. E. Spicer, I. Lindau, P. Skeath, and C. Y. Su, J. Vac. Sci. Technaol. 17, 1019 (1980)

27. J. L. Freec"f and J. M. Woodall Research Report of IBM, Solid State Physics, (1985)

28. E. Merzbacher, Quantum Mechanics, 2nd ed. (John Wiley and Sons, New York, 1970), pp. 100-105.

29. G.Bastard, Phys. Rev. B25, 7584 (1982)

30. J. N. Schulman and Y. C. chang, Phys. Rev. B31, 2056 (1985)

31. E. O. Kane, J. Phys. Chem. Solids 1 249 (1957)

32. H. Shen, P. Parayanthal, Fred H. Pollak, Arthur L. Smirl, J. N. Schulman, R. A. McFarlane and Irnee D'Haenens, Solid State Comm. 59 557 (1986).

33. H. Shen, P. Parayanthal, Fred H. Pollak, Arthur L. Smirl, J. N. Schulman, R. A. McFarlane and Irnee D'Haenens to be published in The Proceedings of the 18th International Conference on the Physics of Semiconductors Stockholm, 1986.

34. Y. C. Chang, J. N. Schulman, G. bastard, Y.Guldman and M. voos, Phys. Rev. B18, 2812 (1978).

35. G. H. Dohler, Superlattices and Microstructures, 1, 279 (1985)

36. G. H. Dohler, H. Kunzel and K. Ploog, Phys. Rev. B25, 2616 (1982)

37. G. H. Dohler and P. Ruden, Phys. Rev. B33, 5932 (1984)

38. Ruden and Dohler, Phys. Rev. B27, 3538, (1983)

39. B. O.Seraphin, Semiconductors and Semimetals edit by R. K. Willarson and Albert C. Beer (Acadmic press, N. Y. and london) vol 9, chapt. 1 (1971)

40. W. E. Engeler, H. Fritzsche, M. Garfinkel, and J.J.Tiemann, Phys. Rev. Lett. 14, 1069 (1965)

41. B. Batz ,Solid State Comm. 4, 241 (1965).

42. L. Van Hove, Phy. Rev. 89 1189 (1953).

43. B. O. Seraphin and N. Bottka, Phy. Rev. 145, 628 (1966).
Porsh, Phys. Stat. Solidi 27, 359 (1968).

44. D. E. Aspnes and J. E. Rowe, Phy. Rev. B, 5, 4022 (1972).

45. D. E. Aspnes and J. E. Rowe, Solid St. Commun. 8, 1145 (1970).

46. Enderlein, Phys. Stat. Solidi, 26 509 (1968).

47. Porsh, Phys. Stat. Solidi 27, 359 (1968).

48. H. Shen and F. H. Pollak, private communication

49. J. Callaway, Phys. Rev. 130, 549 (1963)

50. K. Tharmalingham, Phys, Rev. 130, 2204 (1963)

51. D. E. Aspnes, Phys. Rev. 147, 554 (1966)

52. J. Callaway, Phys. Rev. 134, A998 (1964)

53. K. S. Viswanathan and J. Callaway, Phys. Rev. 143, 564 (1963)

54. F. Aymerich and F.Handler, and D. F. Bloossey, Phys. Rev. 166,921 (1968)

55. D. E., Aspnes, Phys. Rev. 153, 972 (1967)

56. Milton Abramowitz and Irene A. Stegrum , Handbook of Mathematical Function

57. D. E. Aspnes and A. Frova, Solid State Comm. 7, 155 (1969)

58. P. Handle , S. Jasperson and S. Koeppen, Phys. Rev. lett. 23, 1387 (1967)

59. W. A. Albers, Jr. Phys.Rev. Lett. 23, 410 (1969)

60. Photon Technology International Inc., Princeton, N. J. 08542

61. M.Cardona, K. L. Shaklee and F. H. Pollak, Phys. Rev. 154, 696 (1967)

62. W. E. Engeler, M. Garfinkel, and J.J.Tiemann, Phys. Rev. 155, 693 (1967)

63. D. A. B. Miller, D.S. chemla, T.C.Damen, A, C.Gossard, W. Wieggmann, T. H. Wood and C. A. Burrus, Phys. Rev. 32, 1043 (1985)

64. B. V. Shanabrook, O. J. Glembocki and W. T. Beard, submitted to Phys. Rev.

65. P. Parayanthal, H. Shen, Fred H. Pollak, O. J. Glembocki, B. V. Shamabrook and W. T. Breard, Appl. Phys Lett. 48 1261 (1986)

66. O. Berolo and J.C. Woolley, Canad. J. Phys. 49, 1335 (1971).

67. R. C. Miller and D. A. Kleinman, J. Luminescence 30, 520 (1985).

68. P. Dawson, G. Duggan, H.I. Ralph, K. Woodbridge and G.W. Hooft, Superlattices and Microstructures 1, 231 (1985).

69. D. E. Aspnes, Solid State Comm. 8, 267 (1970).

70. F. H. Pollak, C. E. Okeke, P. E. Vanier and P. M. Raccah, J. Appl. Phys. 49, 4216 (1978).

71. O. J. Glembocki, B. V. Shanabrook and W. T. Beard, to be published in the Proceedings of the 2nd Int. Conf. (Yamada) on Modulated Semiconductor Structures, Kyoto, 1985.

72. P. Dawson, G. Duggan, H.I. Ralph, K. Woodbridge and G.W. 't Hooft, Superlattices and Microstructures 1 , 321 (1985).

74. H. Shen, P. Parayanthal, F. H. Pollak, M. Tomkiewicz, T. Drummond and J.N. Schulman, Appl. Phys. Lett. 48 653 (1986)

75. J. L. Aubel, U. K. Reddy, S. Sundaram, W. T. Beard and J. Comas, J. Appl. Phys. 58, 495 (1985).

76. R. C. Miller, A. C. Gossard, G. D. Sanders, Y. C. Chang and J. N. Schulman, Phys. Rev. B32, 8452 (1985).

77. R. P. Silberstein and F. H. Pollak, J. Vac.Sci.Technol. 17 (1980) 1052; also, Solid State Comm. 33 (1980) 1131; also T.E.

Furtak, K.L. Kliever and D.W. Lynch (eds.) Proceedings of an International Conference on Non-Traditional Approaches to Study of the Solid-Electrolyte Interface, North Holland, Amsterdam, 1980, p.269.

78. V. A. Kiselev, Phys. Stat.Sol. (B) 111 (1982) 461.

79. M. Cardona , F. Seitz, D. Turnbull and H. Ehrenreich (eds.) Solid State Physics, Suppl. 11, Academic Press, New York, 1969; also, Feskorperprobleme (Advances in Solid State Physics), Vol. X, Pergammon, Vieweg, 1970, p. 125 and references therein.

80. The dominance of the heavy-hole transitions in FKO was demonstrated by M. Chandresekhar and F.H. Pollak, Phys. Rev.B15 (1977) 2127.

81. Values for the conduction and heavy-hole masses in InP were taken from Concise Encyclopedia of Solid State Physics, ed by R. Lerner and G.L. Trigg, Addison-Wesley, New York, 1983, p. 250.

82. M. Gal, J. S. Yuan, J. M. Viner, P. C. Taylor and G. B. Stringfellow, Phys. Rev. B33, 4410 (1986)

83. G. Fasol, P. Ruden, and K. Ploog, J. of Phys. C17, 1395 (1984) and references therein

84. J. N. Schulman in Proceedings of the Symposium on Layered Structuresand Epitaxy, 1985 Fall Meeting of the Materials Research Society, Vol. 56 of Materials research Society Symposium Proceedings

85. R. Bhattacharya, H. Shen , P. Parayanthal, F. H. Pollak, T. Coutts and H. Aharoni, to be published in Solar Cells.

86. K. Ploog, Annu. Rev. Mater. Sci. 12, 123 (1982)

87. H. Jung, H. Kunzel, G. H. Dohler, and K. Ploog, J. Appl. Phys. 54, 6965 (1983)

88. Y. Horikoshi, A. Fischer, and K. Ploog. Appl. Phys. Lett. 45, 919 (1984)

89. P. Voisin, G. Bastard, and M. Voos, Phys. Rev. B29, 935 (1984)

90. D. A. B. Miller, D. S. Chemla, S. Schmitt-Rink, Phys. Rev. B33 6976, (1985)

91. M. Cardona, Light scattering in Solids Topics in applied physics, Vol. 8 ed. by M. Cardona (Springer-Verlag, Berlin, Heidelberg, New York 1975).

92. W. Richter, Springer Tracts in Modern Physics, Solid State Physics, Vol 78, (Springer, Verlag, Berlin, 1976).

93. R. Louden, Adv. in Physics 13, 423 (1964).

94. G. Abstreiter, M. Cardona, and A. Pinczuk, Light Sacttering by free carrier excitations in Semiconductors in Light scattering in Solids Vol IV, (Springer-Verlag, Berlin, Heidelberg, New york 1975).

95. A. Pinczuk and E. Burstein In /1/ Chap. 2.

96. E. Anastasakis, Dynamical properties of Solids edited by G.K. Hoton and A.A. Maradudin (north Holland Publishing Co., 1980), chap. 3.

97. H. J. Stolz and G. Abstreiter, J. Vac. Sci. Technol., 19, 380, 1981, ibid, J. Phys. Sci. Japan, 49, Suppl. A, 1101, 1980; H. Brugger, F. Schaffer and G. Abstreiter, Phys. Rev. LEtts., 52, 141, 1984.

98. A. Pinczuk, A. A. Ballman, R. E. Nahory,, M. A. Pollack and J. M. Worlock, J. Vac. Sci. Technol., 16, 1168

99. D. J. Olego, R. Schachter, and J. A. Baumann, Appl. Phys. Letts., 45, 1127, 1984.

100. R. Tsu, H. Kawamura, and L. Esaki, Solid State Comm., 15, 321, 1974.

101. G. Abstreiter, Verhandl DPG VI, 12, 81, 1977.

102. G. P. Schwartz, G. J. Gualtier, L. H. Dubois and W. A. Bonner J. Electrochem. Soc., 131, 1716, 1984.

103. U. Rossler, Solid State Comm., 49, No. 10, 943, 1984.

104. T. Nakamura and T. Katoda, J. Apl. Phys., 55, 3064, 1984.

105. D. E. Aspnes and A. A. Studna, Phys. Rev. B27, 985 (1983).

106. E. S. Yang in Fundamentals of Semiconductor Devices (McGraw-Hill, New York, 1978) 9-20.

107. W. E. Spicer, P. W. Chye, C. M. Garner, I. Lindau and P. Pianetta, Surf. Sci., 86, 763, 1979.

108. J. W. Conley and G. D. Mahan, Phys. Rev., 161, 681, 1967.

109. R. Trommer, G. Abstreiter and M. Cardona. Proceeding of the International Conference in Lattice Dynamics Pairs, 1977, ed by M Bolbonski (Flammarion, Pairs, 1978) p189.

110. A. Pinczuk and E. Burstein, Phys. Rev. Letts. 21, 1073 (1968).

111. G.W. Rubloff, E. Anastassakis and F.H. Pollak, Solid State Comm. 13, 1755 (1973).

112. J. Menendez and M. Cardona, Phys. Rev. Lett. 51, 1297 (1983).

113. J. Menendez and M. Cardona, Phys. Rev. B31, 3696 (1985).

114. K. K. Tiong, P. M. Amitharaj, F. H. Pollak, and D. E. Aspnes, D.E., Appl. Phys. Lett., 44, 122, 1984.

115. M.H. Grimsditch, D. Olego and M. Cardona, Phys. Rev. B20, 1758 (1979).

116. D. J. Stirland, and B. W. Straughan, Thin Solid Films, 13, 139, 1976 and references therein. These authors point out that no precise definition of work damage can be given.

117. A. Karpol and B. Pratt, Solid State Commun. 12, 325, 1973.

118. T. M. Donovan, E. J. Ashley and H. C. Bennet, J. Opt. Soc. Am., 53, 1403, 1963.

119. C. E. Jones and A. R. Hilton, J. Electrochem. Soc., 112, 908, 1965.

120. P. J. Zanzucchi and M. T. Duffy, Appl. Opt., 17, 3477, 1978.

121. M. P. Lisitsa, V. N. Malinko, E. V. Pidisnyi and G. E. Tsebulya, Surf. Sci., 11, 411, 1968.

122. D. J. Evans and S. Ushioda, Phys. Rev., 89, 1638, 1974.

123. R. Carles, N. Saint-Cricq, A. Zwick, M. A. Renucci, and J. B. Renucci, J. Phys. Soc. Jpn., 49, Suppl. A, 665, 1980.

124. H. Shen and F. H. Pollak, Appl. Phys. Letts., 45, 692, 1984.

125. F. Cerdeira, C. J. Buchenauer, , F. H. Pollak and M. Cardona, Phys. Rev., B5, 580, 1971.

126. F. H. Pollak, Surf. Sci., 37, 863, 1973.

127. G. Abstreiter, E. Bauser, A. Fisher and K. Ploog, Appl. Phys., 16, 345, 1978.

128. J. Beillmann, B. Prevot, and C. J. Schwab, Phys. C, 16, 1135, 1983.

129. J. Rapis, E. Liarokapis and E. Anastassakis, Appl. Phys. Lett., 44, 125, 1984.

130. C. K. Chin, I. Camlibel, B. V. Dutt, V. Dswaminathan, W. A. Bonner and A. A. Ballman, Appl. Phys. Lett., 42, 901, 1983.

131. P. Warekois, M. C. Levine and H. C. Gatos, J. Appl. Phys., 31, 1302, 1960.